

TAILOR-MADE ADDITIVES IN MOLECULAR BULK-HETEROJUNCTION ORGANIC
PHOTOVOLTAICS AND CHROMOPHORE SPACER CONTROL IN POLYMER LIGHT-
EMITTING DIODES

By

PATRICK M. WIERUSZEWSKI

A THESIS PRESENTED TO THE DEPARTMENT OF CHEMISTRY
OF THE UNIVERSITY OF FLORIDA IN PARTIAL FULFILLMENT
OF THE REQUIREMENTS FOR THE DEGREE OF
BACHELOR OF SCIENCE

UNIVERSITY OF FLORIDA

2012

© 2012 Patrick M. Wieruszewski

To my family and Megan.

ACKNOWLEDGMENTS

I would like to start off by thanking my family for their emotional and financial support throughout my undergraduate studies. Without my parents' hard work and dedication, I would not be where I am today. I am also very grateful for having a scholarly older sister. Graduating college with a dual undergraduate degree, she has always been there for me, providing tips to help me through the tough times. I am very thankful for the continued support and encouragement from my girlfriend, Megan. I am appreciative for her patience and helpfulness on nights I spent late in the lab. Her support has helped me stay on track mentally during this experience, and I couldn't ask for anything more.

I am very thankful of my advisor, Professor John Reynolds, for taking me on as an undergraduate, as I had just barely over a year of college experience under my belt. It is his support and encouragement that gave me an appreciation for research in the sciences, and has led to my success as a researcher. I also thank my mentor, Ken Graham, for teaching me theory and techniques regarding organic electronics and glovebox use. It was a pleasure having Ken as a colleague and a friend throughout this experience. I am also grateful for his continuous support while thousands of miles away at KAUST in Saudi Arabia.

I would like to thank the entire Reynolds' group for their support and help throughout my research experience. They were very encouraging and overall a great group of people to be around. I thank Frank Arroyave for teaching me the freeze-pump-thaw process. I thank Ünsal Koldemir for the occasional delightful conversations we shared. I thank Emily Thompson for her assistance with obtaining high quality pictures

and videos of illuminated pixels presented in the PLED section of this thesis. I also thank Caroline Grand for joining the Reynolds' group and working in the MCCL.

I thank Dr. Kenneth Wagener for allowing me to collaborate with Brian Aitken to produce the PLED portion of this work. I also thank Brian for his support and suggestions throughout our collaboration.

I am very grateful for Dr. Kirk Schanze allowing me to keep my office space and bringing me into his research group upon the departure of the Reynolds' group from UF. I also thank Romain Stalder and Dr. Aubrey Dyer for their continued support as mentors in my research and thesis writing after Dr. Graham's departure from UF.

I am very thankful for Dr. Ben Killian, Dr. Anna Brajter-Toth, Dr. John Mitchell, and Dr. Jeff Gower for giving me the opportunity to serve as a teaching assistant for their courses. Teaching both lower-division and upper-division chemistry courses has helped me grow as a professional. The experience I gained by instructing and managing courses is invaluable, and I am grateful for that.

Finally, I would like to thank Dr. Michael Kessler of the Major Analytical Instrumentation Center, Department of Materials Science and Engineering for his patience and persistence in obtaining many of the TEM images presented in this work. I thank Cheryl Googins, Annyetta Douglas, and Sara Klossner of the chemistry department for their help throughout my studies at UF.

TABLE OF CONTENTS

	<u>page</u>
ACKNOWLEDGMENTS.....	4
LIST OF TABLES.....	9
LIST OF FIGURES.....	10
LIST OF OBJECTS.....	15
LIST OF ABBREVIATIONS.....	16
ABSTRACT.....	17
CHAPTER	
1 INTRODUCTION.....	19
1.1 Organic Solid State Electronics.....	19
1.1.1 Band-structure Theory.....	19
1.1.2 Electrical Conduction and Transport.....	23
1.1.3 Semiconductor Physics.....	25
1.1.4 Space Charge Limited Current.....	28
1.2 Organic Photovoltaics.....	30
1.2.1 Background and Motivation.....	30
1.2.2 Organic Photovoltaic Devices.....	32
1.2.2.1 The Bulk-Heterojunction.....	32
1.2.2.2 Device Operation.....	34
1.2.2.3 Quantification of OPV Parameters.....	36
1.3 Organic Light-Emitting Diodes.....	39
1.3.1 Background and Motivation.....	39
1.3.2 Organic Light-Emitting Devices.....	40
1.3.2.1 Materials.....	40
1.3.2.2 Device Operation.....	42
2 EXPERIMENTAL TECHNIQUES AND INSTRUMENTATION.....	44
2.1 Introduction.....	44
2.2 Materials & Purification.....	44
2.2.1 Materials for Glovebox Use.....	44
2.2.1.1 Synthetic Materials for OPVs and PLEDs.....	44
2.2.1.2 Freeze Pump Thawed Solvents.....	45
2.2.1.3 Materials for Thermal Deposition.....	46
2.2.2 Solvent Distillation.....	47
2.2.3 Stir Bar Cleaning.....	48
2.2.4 Glass Syringe Cleaning.....	49

2.3	Device Fabrication.....	50
2.3.1	Indium Tin Oxide Cleaning	50
2.3.2	Photovoltaic Devices	52
2.3.3	Light-Emitting Diode Devices.....	55
2.3.4	Space Charge Limited Current Devices	55
2.3.4.1	Hole-only Devices.....	55
2.3.4.2	Electron-only Devices	56
2.4	Device Measurement	58
2.4.1	Organic Photovoltaics.....	58
2.4.1.1	Solar Simulation.....	58
2.4.1.2	Power Conversion Efficiency	60
2.4.2	Polymer Light-Emitting Diodes	61
2.4.2.1	Electroluminescence.....	63
2.4.2.2	Luminance	64
2.4.2.3	PLED Performance.....	66
2.4.3	Charge-carrier Mobility Devices.....	68
2.5	Morphology Characterization	68
2.5.1	Atomic Force Microscopy	69
2.5.1.1	Tapping Mode.....	69
2.5.1.2	Position-dependent Morphology	70
2.5.1.3	Thickness Measurements.....	74
2.5.2	Transmission Electron Microscopy	75
2.5.2.1	Sample Preparation	76
2.5.2.2	Top-down Imaging.....	77
3	ASYMMETRIC AND SYMMETRIC OLIGOMERS AS TAILOR-MADE ADDITIVES IN ORGANIC PHOTOVOLTAICS	78
3.1	Introduction	78
3.2	Isoindigo as an Electron Donor	79
3.3	il(TT) ₂ -tBu ₃ Si	80
3.3.1	Photovoltaic Performance	80
3.3.2	Charge Mobility.....	82
3.3.3	Morphology.....	84
3.3.4	Crystal Growth.....	89
3.4	il(TT-tBu ₃ Si) ₂	90
3.4.1	Photovoltaic Performance	91
3.4.2	Charge Mobility.....	92
3.4.3	Morphology.....	94
3.5	il(TT) ₂ -H	99
3.5.1	Photovoltaic Performance	100
3.5.2	Charge Mobility.....	101
3.5.3	Morphology.....	103
3.6	Chapter Summary	105

4	ELECTROACTIVE POLYOLEFINS WITH PRECISELY CONTROLLED CHROMOPHORE SPACING.....	108
4.1	Electroactive Polyolefins	108
4.2	Perfectly Regioregular Terfluorenylidene Polymers	110
4.2.1	Electroluminescence	111
4.2.2	Luminance.....	112
4.2.3	PLED Performance.....	114
4.2.4	Pixel Anomaly.....	115
4.3	Sequenced Triarylamine Functionalized Polyolefins	119
4.4	Chapter Summary	123
5	PERSPECTIVES AND OUTLOOK	125
5.1	Bulk-Heterojunction Organic Photovoltaics	125
5.2	Polymer Light-Emitting Diodes	126
	APPENDIX: DERIVATION OF THE FIELD INDEPENDENT AND DEPENDENT MOTT-GURNEY LAW	128
	LIST OF REFERENCES	131
	BIOGRAPHICAL SKETCH.....	141

LIST OF TABLES

<u>Table</u>		<u>page</u>
3-1	Summary of OPV parameters for increasing mole % asymmetric oligomer in [il(TT) ₂ :il(TT) ₂ -iBu ₃ Si]:PC ₆₁ BM solar cells under AM1.5G 100 mW cm ⁻² simulated radiation.	81
3-2	Summary of OPV parameters for increasing mole % symmetric oligomer in [il(TT) ₂ :il(TT-iBu ₃ Si) ₂]:PC ₆₁ BM solar cells under AM1.5G 100 mW cm ⁻² simulated radiation.	92
3-3	Summary of OPV parameters for increasing mole % asymmetric oligomer in [il(TT) ₂ :il(TT) ₂ -H]:PC ₆₁ BM solar cells under AM1.5G 100 mW cm ⁻² simulated radiation.....	101

LIST OF FIGURES

<u>Figure</u>	<u>page</u>
1-1 Exaggerated diagram of energy states with increasing degrees of conjugation in an organic material, depicting the formation of an “energy band.”	20
1-2 Band diagrams of a metal (a), insulator (b), and semiconductor (c).	21
1-3 Band diagrams of a monovalent (a) and bivalent (b) metal.	22
1-4 Band diagrams of p-type (a) and n-type (b) semiconductors.	26
1-5 Energy band diagrams of a metal and n-type semiconductor before (a) and after contact (b).	27
1-6 Work functions of materials used in this work.....	27
1-7 Band diagrams of electron-only (a) and hole-only (b) devices to employ the SCLC method.....	30
1-8 An exaggerated view of a BHJ (a) and a schematic of a simple BHJ OPV device (b).....	32
1-9 Selected donor (a) and acceptor (b) units commonly used in organic and polymeric materials for OPVs.	33
1-10 Various fullerene derivatives that have been used as acceptors in BHJ OPVs recently.....	34
1-11 Mechanism of the conversion of photoenergy to a usable current in a photovoltaic device—light absorption and formation of an exciton (a), exciton diffusion to the donor-acceptor interface (b), charge transfer (c), charge separation and transport (d), charge collection at the electrodes (e), and the resulting usable current (f).....	36
1-12 Sample J-V curve of illuminated and dark current, with all parameters of interest labeled for the calculation of the PCE.	37
1-13 Schematic of a simple OLED device.	40
1-14 A variety of hole transport (a) and electron transport (b) layers found in the literature.	41
1-15 Mechanism of the emission of light from an applied bias in an OLED—charge injection (a), charge transport (b), charge recombination and formation of an exciton (c), and the resulting emission of light (d).....	43

2-1	Solvent distillation column and cooling system setup.	47
2-2	ITO pattern (a) and shadow mask pattern (b).	51
2-3	SolidWorks model of the device holder used for thermal deposition.	54
2-4	Schematic of patterned mask (a) and SolidWorks model of the evaporation device holder (b) used for anode deposition of electron-only devices.	57
2-5	Schematic of an electron-only device.	58
2-6	Schematic of the air mass conditions used for photovoltaic measurements (a) and their standard spectra (b).	60
2-7	SolidWorks schematic of the top (a,b) and bottom (c,d) of the PLED device holder.	62
2-8	An illuminated PLED pixel under constant bias, viewed from the outside of the device holder.	63
2-9	Luminous flux leaving the source, labeled with the parameters used to calculate luminance.	64
2-10	Block diagram of the Konica Minolta CS 100 luminance meter—objective lens (O), aperture stop (S_1), chopper (C), field stop (S_2), spectral-response correction filter (F), silicon photocell (P), current-to-voltage converter (I/V), and analog-to-digital converter (A/D).	65
2-11	Example of a PLED's x and y coordinates, plotted using the standard CIE 1931 color space chromaticity diagram, showing a deep red color.	66
2-12	Schematic of an AFM.	70
2-13	Structure of APFO-DOT.	71
2-14	AFM images of APFO-DOT:PC ₇₁ BM (1:4) in chlorobenzene at the center (a), between the center and the edge (b) and towards the edge (c) of the device. The device ITO and cathode layout with the labeled A, B, and C positions (d). .	72
2-15	Mechanical process of spin coating—clean device secured to the spin chuck by vacuum (a), solution deposited on device (b), and spin speed ramped up (c).	73
2-16	Use of SpmLabAnalysis software to calculate the stepheight for an AFM image containing a scratch (left) and the film (right) (a), height distribution (b), and stepheight calculation (c).	75
2-17	Schematic of a TEM.	76

2-18	Area of a device from which a TEM sample was prepared.....	77
3-1	Cartoon example of a parent molecule (a) and the resulting “tailor-made additive” (b).....	78
3-2	Chemical structures of <i>trans</i> -isoidindigo (a) and il(TT) ₂ , the parent oligomer used in the experiments presented in this work (b).	79
3-3	Chemical structure of the asymmetric tailor made additive, il(TT) ₂ -iBu ₃ Si.....	80
3-4	Representative J-V curves of 0 to 100 % asymmetric oligomer in [il(TT) ₂ :il(TT) ₂ -iBu ₃ Si]:PC ₆₁ BM solar cells under AM1.5G 100 mW cm ⁻² simulated radiation.	82
3-5	Summary of hole mobilities for increasing mole % asymmetric oligomer in [il(TT) ₂ :il(TT) ₂ -iBu ₃ Si]:PC ₆₁ BM SCLC devices.	83
3-6	Representative J-V plots of 0, 10, 20 (a), 30, 40 (b), 50 and 100 (c) mole % asymmetric oligomer in [il(TT) ₂ :il(TT) ₂ -iBu ₃ Si]:PC ₆₁ BM SCLC devices.....	84
3-7	AFM images of increasing mole % asymmetric oligomer in [il(TT) ₂ :il(TT) ₂ -iBu ₃ Si]:PC ₆₁ BM devices. All images shown are 5 × 5 μm.....	86
3-8	AFM images of increasing mole % asymmetric oligomer in [il(TT) ₂ :il(TT) ₂ -iBu ₃ Si]:PC ₆₁ BM devices. All images shown are 1 × 1 μm.....	86
3-9	TEM images of increasing mole % asymmetric oligomer in [il(TT) ₂ :il(TT) ₂ -iBu ₃ Si]:PC ₆₁ BM devices.....	87
3-10	Cross-sectional TEM images of 20 (a) and 100 (b) mole % asymmetric oligomer in [il(TT) ₂ :il(TT) ₂ -iBu ₃ Si]:PC ₆₁ BM devices as well as a 3 nm Gaussian blur (c) applied to image b.	88
3-11	Crystal length dependence on mole % il(TT) ₂ -iBu ₃ Si as a function of il(TT) ₂ (a) and representative polarized microscope images of increasing mole % il(TT) ₂ -iBu ₃ Si in il(TT) ₂ :il(TT) ₂ -iBu ₃ Si.	90
3-12	Chemical structure of the symmetric tailor made additive, il(TT-iBu ₃ Si) ₂	91
3-13	Representative J-V curves of 0 to 100 % symmetric oligomer in [il(TT) ₂ :il(TT-iBu ₃ Si) ₂]:PC ₆₁ BM solar cells under AM1.5G 100 mW cm ⁻² simulated radiation.....	92
3-14	Summary of hole mobilities for increasing mole % symmetric oligomer in [il(TT) ₂ :il(TT-iBu ₃ Si) ₂]:PC ₆₁ BM SCLC devices.	93
3-15	Representative J-V plots of 0, 10, 20 (a), 30, 40 (b), 50 and 100 (c) mole % symmetric oligomer in [il(TT) ₂ :il(TT-iBu ₃ Si) ₂]:PC ₆₁ BM SCLC devices.....	94

3-16	AFM images of increasing mole % symmetric oligomer in [il(TT) ₂ :il(TT- tBu ₃ Si) ₂]:PC ₆₁ BM devices, with the typical color scale (a) and in gray scale (b). All images shown are 5 × 5 μm.	96
3-17	AFM images of increasing mole % symmetric oligomer in [il(TT) ₂ :il(TT- tBu ₃ Si) ₂]:PC ₆₁ BM devices. All images shown are 1 × 1 μm.	97
3-18	TEM images of increasing mole % symmetric oligomer in [il(TT) ₂ :il(TT- tBu ₃ Si) ₂]:PC ₆₁ BM devices.	98
3-19	Chemical structure of an asymmetric tailor made additive, il(TT) ₂ -H.	100
3-20	Representative J-V curves of 0 to 100 % asymmetric oligomer in [il(TT) ₂ :il(TT) ₂ -H]:PC ₆₁ BM solar cells under AM1.5G 100 mW cm ⁻² simulated radiation.	101
3-21	Summary of hole mobilities for increasing mole % asymmetric oligomer in [il(TT) ₂ :il(TT) ₂ -H]:PC ₆₁ BM SCLC devices.	102
3-22	AFM images of increasing mole % asymmetric oligomer in [il(TT) ₂ :il(TT) ₂ - H]:PC ₆₁ BM devices. All images shown are 5 × 5 μm.	104
3-23	AFM images of increasing mole % asymmetric oligomer in [il(TT) ₂ :il(TT) ₂ - H]:PC ₆₁ BM devices. All images shown are 1 × 1 μm.	104
3-24	TEM images of increasing mole % asymmetric oligomer in [il(TT) ₂ :il(TT) ₂ - H]:PC ₆₁ BM devices.	105
4-1	Typical electroactive polymer system structures—conjugated polymers (a), main chain π-functional polymers (b) and side chain π-functional polymers (c).	109
4-2	Family of electroactive terfluorenylidene polymers—regioregular unsaturated (a), regioregular saturated (b), regiorandom unsaturated (c), and regiorandom saturated (d).	111
4-3	Electroluminescence spectra of saturated polymers at a constant driving bias.	112
4-4	Luminance and current density as a function of driving voltage for unsaturated (a) and saturated (b) polymers.	113
4-5	Calculated EQEs for the entire family of terfluorenylidene polymers.	115
4-6	AFM images of P-3,3-TF-S (a), P-6,6-TF-S (b), and P-9,9-TF-S (c).	116
4-7	Optical microscope images of the aluminum electrode on devices with P-3,3- TF-S (a), and P-9,9-TF-S (b).	116

4-8	Time-lapsed images taken every 2.5 s of a P-9,9-TF-S pixel at a constant driving bias of 13 V.	117
4-9	Family of regioregular sequenced triarylamine functionalized polyolefins—unsaturated (a) and saturated (b) hole transporters.	120
4-10	Summary of average hole mobility data (a) and current-voltage characteristics (b) for SCLC devices.	121
4-11	Representative J-V plots of unsaturated (a) and saturated (b) TPF polymer containing SCLC devices.	122
A-1	Schematic of an organic semiconducting material sandwiched by two electrodes, with an applied voltage (V) and diffusion length (L) of the current flow in the positive x-direction.	128

LIST OF OBJECTS

<u>Object</u>	<u>page</u>
4-1 Video of a P-9,9-TF-S pixel at a constant bias of 13 V	117

LIST OF ABBREVIATIONS

ADMET	Acyclic diene metathesis
AFM	Atomic force microscopy
BHJ	Bulk-heterojunction
CB	Conduction band
EL	Electroluminescence
EQE	External quantum efficiency
FF	Fill factor
HOMO	Highest occupied molecular orbital
$t\text{Bu}_3\text{Si}$	Triisobutylsilyl
ITO	Indium tin oxide
J-V	Current density-voltage
J_{sc}	Short circuit current density
LUMO	Lowest unoccupied molecular orbital
OLED	Organic light-emitting diode
OPV	Organic photovoltaic
PC ₆₁ BM	[6,6]-phenyl-C61-butyric acid methyl ester
PCE	Power conversion efficiency
PEDOT:PSS	Poly(3,4-ethylenedioxythiophene):poly(styrene sulfonic acid)
PLED	Polymer light-emitting diode
SCLC	Space charge limited current
TEM	Transmission electron microscopy
TPF	4,4'-bis(phenyl- <i>m</i> -toluylamino)biphenyl
VB	Valence band
V_{oc}	Open circuit voltage

Abstract of Thesis Presented to the Department of Chemistry
of the University of Florida in Partial Fulfillment of the
Requirements for the Degree of Bachelor of Science

TAILOR-MADE ADDITIVES IN MOLECULAR BULK-HETEROJUNCTION ORGANIC
PHOTOVOLTAICS AND CHROMOPHORE SPACER CONTROL IN POLYMER LIGHT-
EMITTING DIODES

By

Patrick M. Wieruszewski

May 2012

Chair: John R. Reynolds
Major: Chemistry

Organic electronics are quickly growing in popularity with promising applications in transistors, light-emitting devices, and renewable solar energy (photovoltaics). Organic electronics are highly researched due to their solution-processability, use of non-toxic materials, and ability to produce thin, lightweight, and flexible devices. To compete with their inorganic counterparts in the consumer and industrial markets, however, power conversion efficiencies (PCEs) must be increased.

In the first portion of this work, the effects of tailor-made additives in molecular bulk-heterojunction (BHJ) organic photovoltaics (OPVs) are explored. A tailor-made additive is structurally similar to its parent molecule, with the exception of a minor defect; and when incorporated into BHJ OPVs, affords fine tuned morphologies and increased PCEs. In the second portion of this work, a new class of electroactive polyolefins for use in polymer light-emitting diodes (PLEDs) is explored. Through acyclic diene metathesis (ADMET) polymerization, polyolefins with precisely spaced chromophores were afforded. When incorporated into PLEDs, systematic control of external quantum efficiency (EQE) and hole mobility is achieved through varying the

number of carbon atoms between chromophores on the electrically insulating backbone. Through the use of novel synthetic materials and innovative device design, performance in OPVs and PLEDs may be increased to meet industrialization requirements.

CHAPTER 1 INTRODUCTION

Modern electronic devices govern the way in which today's society operates. Today, electronics span a variety of applications ranging from industrial settings to the consumer household. In 1821, Thomas Johann Seebeck discovered the thermoelectric effect when studying the temperature-dependent thermopower of PbS and ZnSb.¹ This initial work is what gave rise to what we know and love as “semiconductors” today. It wasn't until nearly a century later in 1911 when the term “halbleiter” (German for “semiconductor”) was introduced by Königsberger and Weiss.² In 1947, the first working transistor was fabricated at AT&T Bell Telephone Laboratories;³ thereafter giving rise to a booming interest in semiconducting devices.

1.1 Organic Solid State Electronics

The focus of this work is the study of organic electronics, which is relatively new to the field of electronics. In 1977, Alan Heeger, Alan MacDiarmid, and Hideki Shirakawa discovered and synthesized the first conducting polymer; for which they received The Nobel Prize in Chemistry 2000.⁴ These initial findings are what jump started peoples' interests in studying the electronic properties of organic materials. Since then, organic materials have been featured in a wide variety of electronic device applications—electrochromic windows and displays,^{5,6} field-effect transistors,⁷⁻¹⁰ thin film transistors,^{11,12} light emitting diodes,¹³⁻²⁰ semiconductor memory devices,²¹ photodetectors,²² and photovoltaics.²³⁻²⁸

1.1.1 Band-structure Theory

The electrical conduction in organic materials arises from the delocalization of π electrons along the conjugated double bonds of the system. In simple molecular orbital

theory, the highest occupied molecular orbital (HOMO) and lowest unoccupied molecular orbital (LUMO) have distinct energy states. As the degree of conjugation in the system increases, the number of energy states increases, and the energy gap between these states decreases. With a conjugated polymeric system, or any organic system with a higher order of conjugation, these energy states begin to approach each other with an increasing degree of conjugation, giving rise to “energy bands” (Figure 1-1).

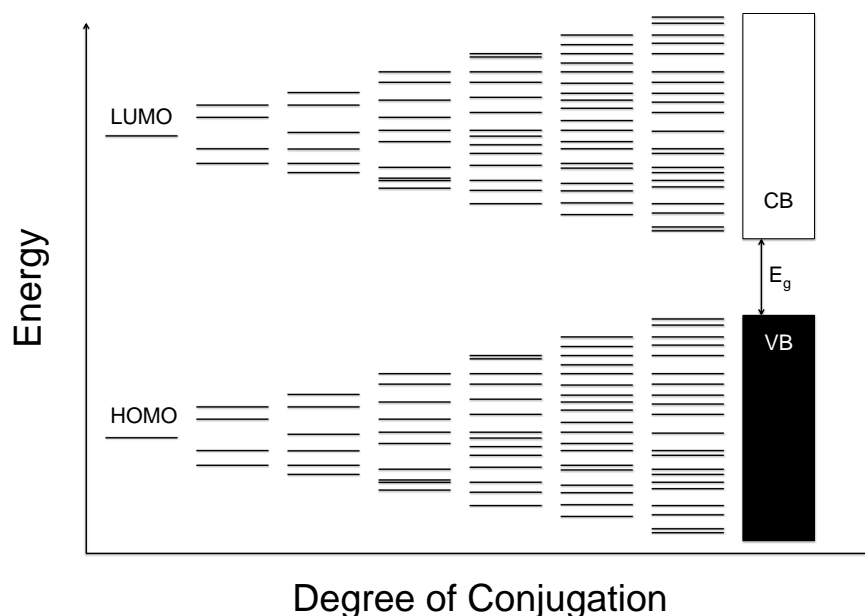


Figure 1-1. Exaggerated diagram of energy states with increasing degrees of conjugation in an organic material, depicting the formation of an “energy band.”

In Figure 1-1, there is an energy difference between the HOMO and LUMO levels of the bands, which is termed the “band gap,” and its energy will be referred to as the gap energy (E_g) in this work. In solid-state physics, this gap energy can be used to define various classes of materials. If the gap energy is negligible (~ 0 eV), the material is referred to as a conductor (Figure 1-2a); these are typically metals. If the gap energy is rather large (> 3 eV), the material is referred to as an insulator (Figure 1-2b); these

are typically ceramics. Finally, if the gap energy is somewhere between the above-mentioned materials (< 3 eV), the material is referred to as a semiconductor (Figure 1-2c). These gap energy values are estimates and should not be interpreted as the limits for conductors, insulators, and semiconductors.

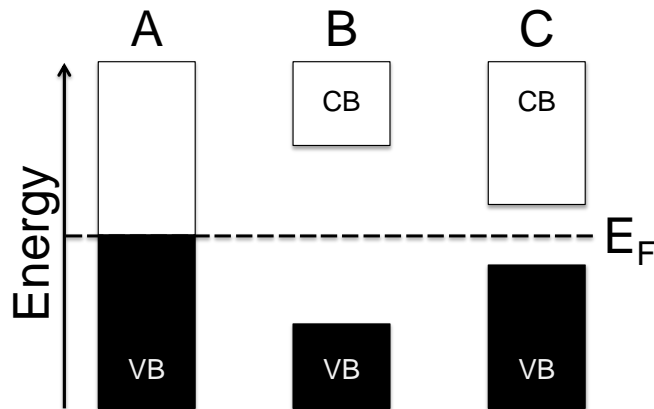


Figure 1-2. Band diagrams of a metal (a), insulator (b), and semiconductor (c). Here, CB is the conduction band, VB is the valence band, and E_F is the Fermi energy. The black shaded regions show occupied energy states.

The gap energy is also slightly dependent on temperature. The gap energy at a certain temperature can be calculated using Varshni's empirical equation,²⁹

$$E_{g(T)} = E_{g(T=0)} - \frac{\alpha T^2}{T + \beta} \quad (1-1)$$

Where α and β are empirically determined material constants. However, there were some complications with this calculation as β is related to the Debye temperature, Θ_D , which can sometimes be negative.²⁹ There have been computational analyses of this problem to overcome it;³⁰ however, thorough examination of these calculations is beyond the scope of this work. It can be seen from Equation 1-1 that as temperature decreases, the gap energy increases, due to decreased atomic vibrations.

Having introduced the valence band (VB) and conduction band (CB) in Figures 1-1, and 1-2, it is appropriate to discuss them now. The valence band is essentially a

“housing” for the valence electrons. According to the Pauli principle, a spin-up and spin-down electron may occupy each available energy state. In a metal—monovalent (Figure 1-3a), bivalent (Figure 1-3b), etc.—the valence band is partially filled with electrons, giving rise to electrical conduction. One may ask at this point: doesn’t a bivalent metal have two valence electrons, thus a completely filled valence band and is consequently an insulator? In principle, this should be correct; however, bivalent metals have slightly overlapping bands of higher energy. Due to weak binding interactions between the valence electrons and the nucleus, some electrons at the top of the lower energy band spill into the bottom of the higher energy band, as electrons tend to assume the lowest energy state possible (Figure 1-3b).

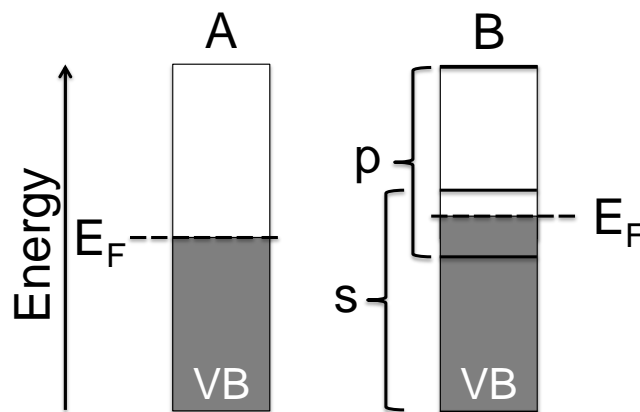


Figure 1-3. Band diagrams of a monovalent (a) and bivalent (b) metal. Here, s and p are atomic orbitals. The grey shaded regions show occupied energy states.

In an insulator, the valence band is completely filled with electrons, and thus does not electrically conduct. In an intrinsic semiconductor, the valence band is completely filled with electrons; however, the gap energy is small in these materials ($E_g < 3$ eV). Thus, in the presence of an energetic excitation—thermal for example—sufficient energy may be supplied to excite a negatively charged electron (e^- in schematics) into the conduction band, leaving behind a positive charge in the valence band. This

positive charge is often referred to as an “electron-hole,” or “hole” (‘ h⁺ ’ in schematics) for short.

In the band diagrams of Figures 1-2 and 1-3, E_F is the Fermi energy (also referred to as the chemical potential, μ), which is extremely important in the discussion of semiconductors. The Fermi energy is the highest energy electrons assume at absolute zero ($T = 0$ K). Furthermore, the probability at which an electron assumes a specific energy (E) can be calculated using Fermi-Dirac statistics. This probability is called the “Fermi function” ($\mathcal{F}(E)$), and is defined by,

$$\mathcal{F}(E) = \frac{1}{\exp\left(\frac{E-E_F}{k_B T}\right)+1} \quad (1-2)$$

Where k_B is the Boltzmann constant, 8.6173×10^{-5} eV K⁻¹, and T is the absolute temperature. Thus, if the band is completely filled with electrons, the probability of finding an electron at any given energy state, $\mathcal{F}(E)$, is equal to 1; and it follows that an empty band has $\mathcal{F}(E) = 0$. This can be visualized using the band diagram presented for the intrinsic semiconductor in Figure 1-2. At absolute zero, the valence band is completely filled with electrons, thus $\mathcal{F}(E) = 1$; similarly, the conduction band is empty, thus $\mathcal{F}(E) = 0$. From Equation 1-2 it can be realized that when $T \neq 0$ K, and $E = E_F$, then $\mathcal{F}(E) = \frac{1}{2}$, which is a more useful definition of the Fermi energy than stated before.

1.1.2 Electrical Conduction and Transport

Our discussion leading up to the semiconductor devices discussed in this work begins with a foundation in electrical conduction and transport. In semiconducting devices, we are interested in studying the movement of charge carriers, both electrons and holes. We begin with a few fundamental principles of electrical conduction.

The potential difference in a material (V), is defined by Ohm's law,

$$V = IR \quad (1-3)$$

Where I is the current flow measured in amperes (A), and R is the resistance of the material measured in ohms (Ω). Ohm's law takes on another form defining the current density (J),

$$\vec{J} = \sigma \vec{E} \quad (1-4)$$

Where σ is the conductivity, measured in $\Omega^{-1} \text{ cm}^{-1}$, and is commonly expressed as its reciprocal, the resistivity, ρ , and current density is the current flow per unit surface area,

$$I = \int_S \vec{J} \cdot d\vec{A} \quad (1-5)$$

The external electric field, E, is defined by,

$$\vec{E} = \frac{V}{L} \quad (1-6)$$

The current density can also be related to the velocity of carriers through the material,

$$\vec{J} = N\vec{v}e \quad (1-7)$$

Where N is the number of carriers per unit volume, v is the velocity of the carriers, and e is the elementary charge, $1.6022 \times 10^{-19} \text{ C}$. This leads us to the carrier mobility, a highly desired term to characterize the performance of an electronic device. The carrier mobility, μ , is defined by

$$\mu = \frac{\vec{v}_d}{E} \quad (1-8)$$

Where v_d is the drift velocity of the carriers under the influence of an applied external electric field, E. Combining Equations 1-4, 1-7, and 1-8, we can relate the mobility of carriers to the conductivity,

$$\sigma = N\mu e \quad (1-9)$$

Equation 1-9 allows us to calculate the mobility of carriers using intrinsic values. However, as mentioned in section 1.1.1, when sufficient energy is added to a semiconductor, an electron is excited into the conduction band leaving a hole in the valence band. Since both electrons and holes contribute to electrical conduction, both have a drift velocity, and thus have different mobilities. We are interested in the mobility of both the electrons and holes, and thus Equation 1-9 is rewritten considering both charge carriers,

$$\sigma = N_e \mu_e e + N_h \mu_h e \quad (1-10)$$

Where the subscripts e and h refer to electrons and holes, respectively.

1.1.3 Semiconductor Physics

At this point, we should bring our attention back to the band diagrams, and describe typical semiconductors. In sections 1.1.1 and 1.1.2, we discussed intrinsic semiconductors, that is, materials with no impurities. However, extrinsic semiconductors are of more interest for devices. Let us consider silicon, which has a valence of IV, for the purposes of this discussion. If we add a nominal amount of a dopant—boron for example, which has a valence of III—we introduce an electron deficient impurity, as boron has one electron less than silicon. This results in an increased number of positive charges (holes). These types of dopants are referred to as acceptors, and the resulting semiconductor is referred to as “p-type” semiconductor (Figure 1-4a).

Contrarily, if we dope the silicon with a dopant of an extra electron—phosphorous for example, which has a valence of V—we introduce an electron rich impurity. These extra electrons are referred to as donors, and the resulting semiconductor is referred to as “n-type” semiconductor (Figure 1-4b).

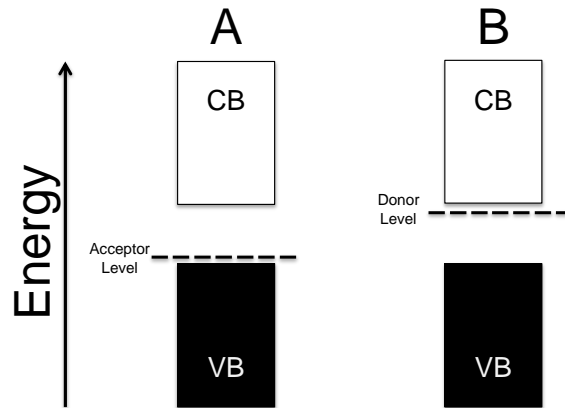


Figure 1-4. Band diagrams of p-type (a) and n-type (b) semiconductors.

With semiconducting devices, we want to make metal-semiconductor contacts. The following discussion about contacts is important for the selection of metals and materials when fabricating semiconducting devices. Let us consider a metal-semiconductor contact with an n-type material. Prior to contact, the Fermi energy of the n-type semiconductor is larger than the Fermi energy of the metal (Figure 1-5a). Here, we have introduced a new term, Φ , the work function. The work function is defined as the amount of energy required to remove an electron from the Fermi surface into vacuum. Once the metal and semiconductor are brought into contact and an external electric field is applied, electrons are driven from the semiconductor into the metal until the Fermi energy is at equilibrium. This gives rise to the 'curved' region—also referred to as the depletion region, which has a low charge carrier density—that is observed, resulting in an energy barrier (Figure 1-5b).

As mentioned, work functions of materials are important for proper selection of materials to fabricate a quality electronic device. Figure 1-6 summarizes work functions of materials that were used in this work.

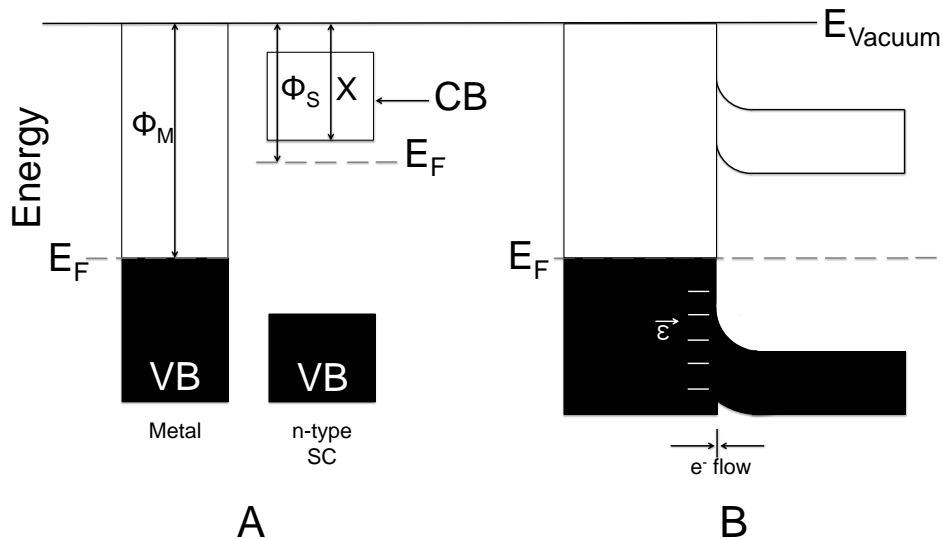


Figure 1-5. Energy band diagrams of a metal and n-type semiconductor before (a) and after contact (b). Here, Φ is the work function of a metal (m) and semiconductor (s), χ is the electron affinity, and ϵ is the applied electric field. Black shaded regions shown occupied states.

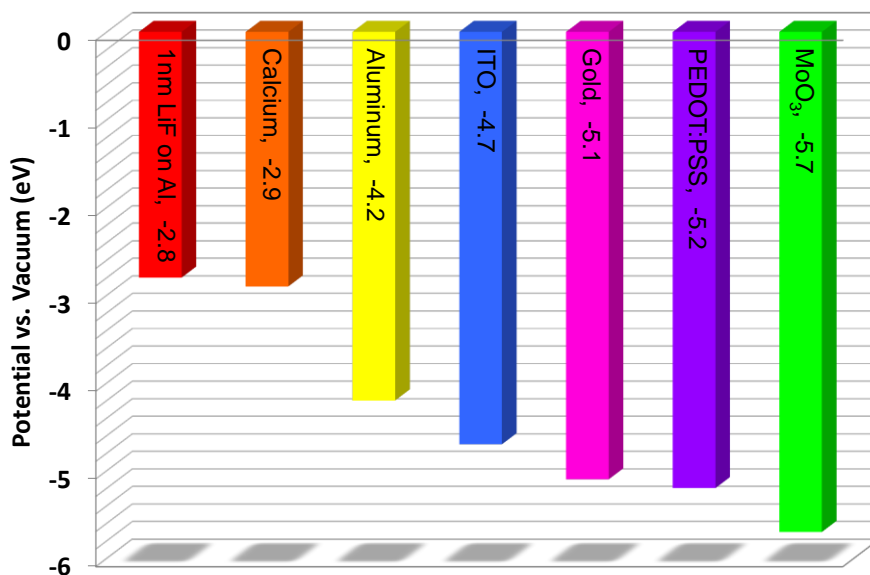


Figure 1-6. Work functions of materials used in this work—1 nm lithium fluoride on aluminum,³¹ calcium,³² aluminum,³¹ indium tin oxide (ITO),³³ gold,³⁴ poly(3,4-ethylenedioxythiophene):poly(styrene sulfonic acid) (PEDOT:PSS),³⁵ and molybdenum (VI) oxide.³⁶

1.1.4 Space Charge Limited Current

In section 1.1.2 we defined an expression for the conductivity allowing us to quantify electron and hole mobilities in a semiconducting device (Equation 1-10). Many methods exist to quantify mobilities in organic devices—use of field-effect transistors, time-of-flight measurements, and the space charge limited current (SCLC) method. It is generally accepted that the SCLC method serves as an accurate technique to measure mobilities of charge carriers in organic semiconducting devices. This is because organic systems, unlike metals, are disordered systems in the sense that they are composed of many intertwined/packed molecules. Thus charge carriers in an organic system transport within a molecule along delocalized π -conjugation, but must also reach the next closest molecule and thus transport by a “hopping” mechanism. Consequently, organic systems suffer from lower conductivities and thus mobilities compared to classic metal conductors. Luckily, organic materials satisfy crucial requirements to employ the SCLC method—low charge carrier mobilities, and trap-free charge transport.

In the absence of trap states, the space charge limited current (J_{SCL}) is defined by the Mott-Gurney law,³⁷

$$J_{SCL} = \frac{9}{8} \epsilon_0 \epsilon_r \mu \frac{V_i^2}{L^3} \quad (1-11)$$

Where ϵ_0 is the vacuum permittivity, $8.8542 \times 10^{-12} \text{ F m}^{-1}$, ϵ_r is the relative permittivity, μ is the field-independent mobility, L is the length, or in the case of organic devices, the thickness of the film, and V_i is the dropped bias across the device:

$$V_i = V - V_{rs} - V_{bi} \quad (1-12)$$

Where V is the applied bias, V_{rs} is the dropped bias resulting from series resistance of the ohmic contacts, and V_{bi} is the “built-in” voltage, which is the voltage across the depletion region (see section 1.1.3 and Figure 1-5b).

In organic materials, however, shallow traps are often present, thus the mobility is expected to be field dependent,

$$\mu = \mu_0 \exp(\gamma\sqrt{E}) \quad (1-13)$$

Where μ_0 is the zero-field mobility and γ is the field dependent term. Thus, the field-dependent mobility described by the Poole-Frenkel effect can be calculated using the modified Mott-Gurney law,³⁸

$$J_{SCL} = \frac{9}{8} \varepsilon_0 \varepsilon_r \mu_0 \exp(0.891\gamma\sqrt{E}) \frac{V_i^2}{L^3} \quad (1-14)$$

Derivations of the field independent and dependent SCLC models can be viewed in detail in the appendix.

Now, a very important complication arises when considering the SCLC method. The field dependent Mott-Gurney law described by Equation 1-14 is useful for measuring the zero-field mobility of a single charge carrier and is widely accepted as the method of choice for organic semiconducting devices.^{39–43} However, as discussed in section 1.1.1, there are two charge carriers in organic materials which exhibit a mobility—electrons and holes. Thus, in order to accurately quantify the charge carrier mobility of electrons or holes, the device must be fabricated to isolate one of the charge carriers.

To achieve a device of only electron or hole carriers, metals must be selected with specific work functions to make ohmic contacts in order to inject only one charge carrier to satisfy the SCLC model. To measure only the mobility of electrons, two low work

function metals must be chosen for the electrodes (Figure 1-7a). This ensures that no holes are injected or collected by either electrode. Similarly, to measure only the mobility of holes, two high work function metals must be used as the electrodes (Figure 1-7b). Accordingly, no electrons are injected or collected by the high work function metals.

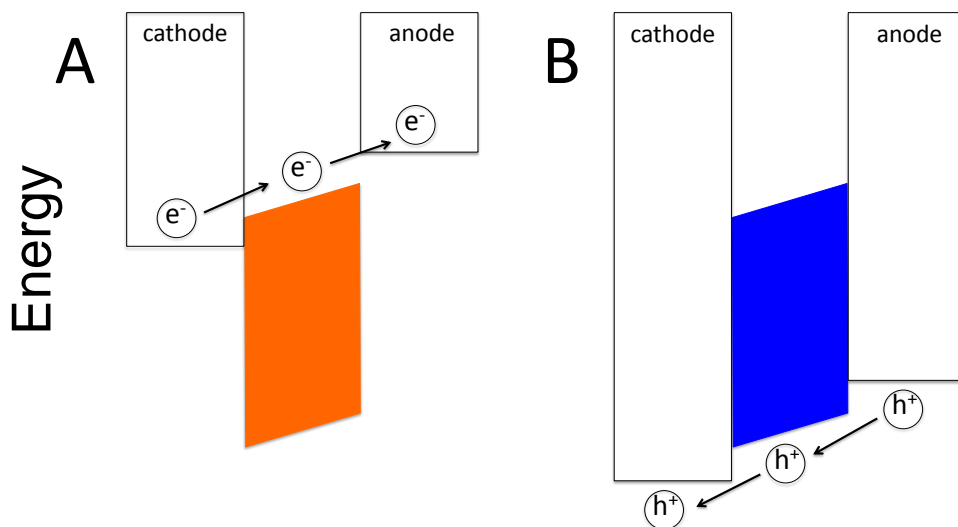


Figure 1-7. Band diagrams of electron-only (a) and hole-only (b) devices to employ the SCLC method.

1.2 Organic Photovoltaics

Now that we have established the basic principles of electrical properties of materials, conduction, and transport, we can begin our discussion of semiconducting devices, starting with organic photovoltaics (OPVs).

1.2.1 Background and Motivation

As discussed in the section 1.1, electronics are the driving forces for the day-to-day operation of today's modern world. New technological advances are coming to light every day, bringing new gadgets to the consumer and industrial markets. However, with these increasing amounts of technological advances and increased usage of these

gadgets, energy demands to power these devices are higher than ever, and are continuing to rise.

Currently, fossil fuels dominate the energy production market in the world. These mainly petroleum-based materials produce harmful emissions into the Earth's atmosphere. It is estimated that by 2050, the world demand of energy will be approximately 30 terawatts, making the energy market a 30 trillion dollar industry.⁴⁴ It is estimated that the United States crude oil production will rise over 20% in the next decade.⁴⁵ Furthermore, the Energy Information Administration (EIA) estimates energy-related carbon dioxide emissions to increase 3% by 2035.⁴⁵ Given such a high demand in energy, renewable sources are being investigated to limit the amount of harmful atmospheric emissions produced by petroleum-based materials. To minimize these numbers, research efforts towards renewable solar energy are increasing, giving rise to the motivation for this work.

Currently, the highest performing photovoltaic cells consist of inorganic-based materials. Solar Junction currently holds the world record for PV efficiency of a silicon-based cell at 43.5% under concentrated 1,000 suns radiation.⁴⁶ Inorganic cells are however brittle, expensive to manufacture, and use toxic materials during fabrication.

Organic solar cells, on the other hand, are of interest in this work. These cells are relatively inexpensive to produce and use non-toxic materials in fabrication. Additionally, organic solar cells are solution-processable, and with recent technologies, organic layers can be deposited on flexible substrates through slot-die coating,⁴⁷⁻⁴⁹ ink-jet printing,⁵⁰⁻⁵³ and flexographic printing.⁵⁴⁻⁵⁷ These processes allow for lightweight, flexible cells that are not restricted to a solar field or roof top as are inorganic cells. To

compete with their inorganic counterparts in the consumer market, however, power conversion efficiencies (PCEs) must be increased. Currently, organic solar cells are shy of the 10% mark thought to be required for industrialization; however, solar cells based on polymeric⁵⁸⁻⁶⁰ and small molecular^{61,62} systems have reached PCEs of 8 and 6%, respectively.

1.2.2 Organic Photovoltaic Devices

A simple OPV has a vertical architecture consisting of a conductive organic layer sandwiched between two electrodes on top of a transparent substrate (Figure 1-8b). The organic layer is a mixture of an electron donor (will be referred to as donor), and an electron acceptor (will be referred to as acceptor), which is termed as a bulk-heterojunction (BHJ, Figure 1-8a).

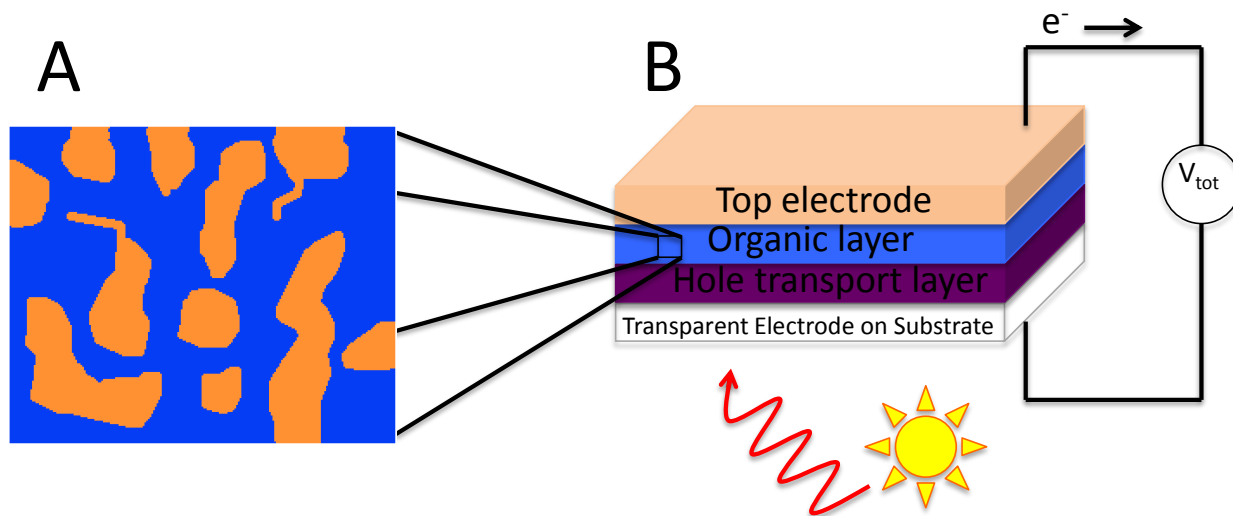


Figure 1-8. An exaggerated view of a BHJ (a) and a schematic of a simple BHJ OPV device (b).

1.2.2.1 The Bulk-Heterojunction

The number of approaches to designing molecules for use in OPVs is endless. Over the past several years, a plethora of donors and acceptors have been used in both

small molecular and polymeric solar cells. Some popular donor and acceptor entities are summarized in Figures 1-9a and 1-9b, respectively. This summary of electron-rich and electron-deficient entities should not be interpreted as complete, but rather a sample of those one can find in the literature.

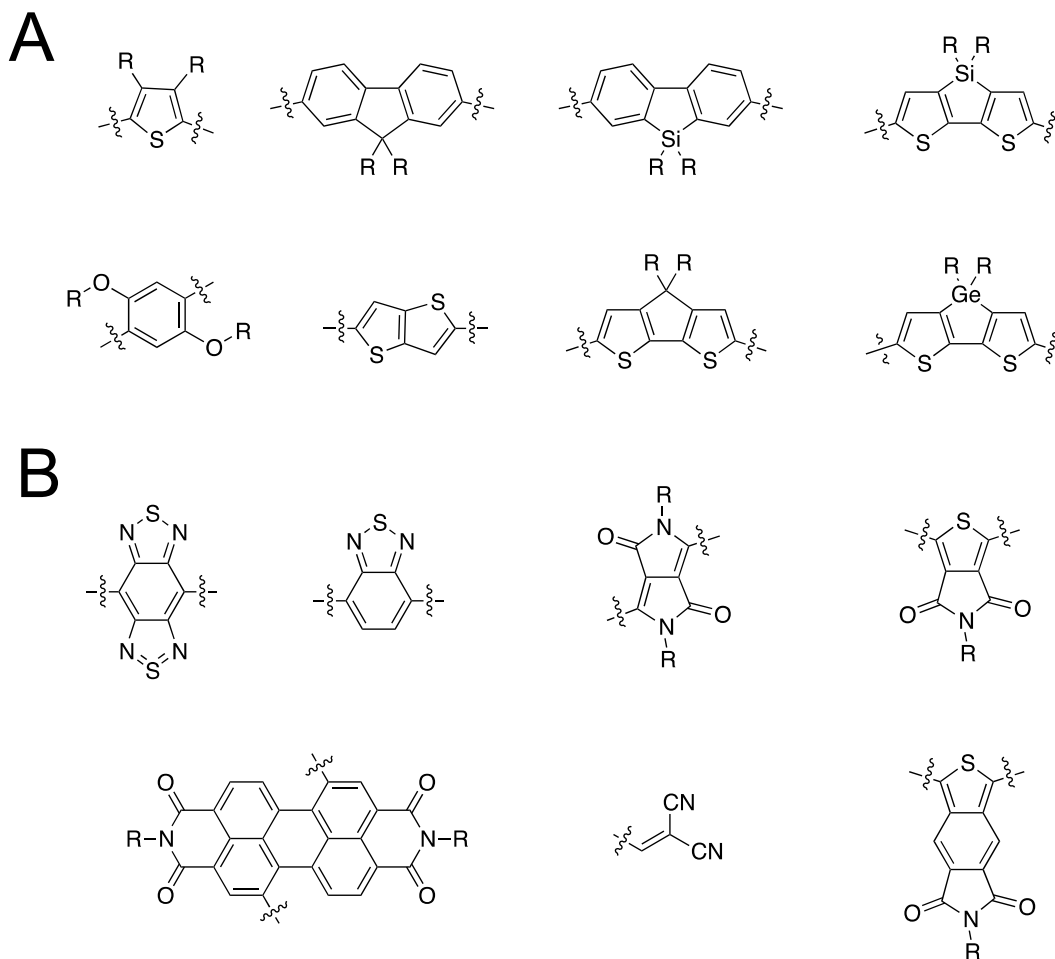


Figure 1-9. Selected donor (a) and acceptor (b) units commonly used in organic and polymeric materials for OPVs.

The donor and acceptor units presented in Figure 1-9 are used to design molecules for high performing OPVs. As mentioned above, the organic layer is a mixture of donor and acceptor (BHJ). The materials presented in Figure 1-9 are typically used to synthesize a donor molecule for a BHJ.

The acceptor in a BHJ is typically a fullerene derivative, most notably PC₆₁BM⁶³ or PC₇₁BM²³ (Figure 1-10). These fullerene derivatives have been used in high performance BHJ OPVs and can be purchased with high purity. However, recently many groups have been investigating other fullerene derivatives as acceptors in OPVs—dihydronaphthyl,^{24,64} bis-adduct,^{65,66} cyclopropano,⁶⁷ and 1,4 fullerene derivatives⁶⁸ (Figure 1-10).

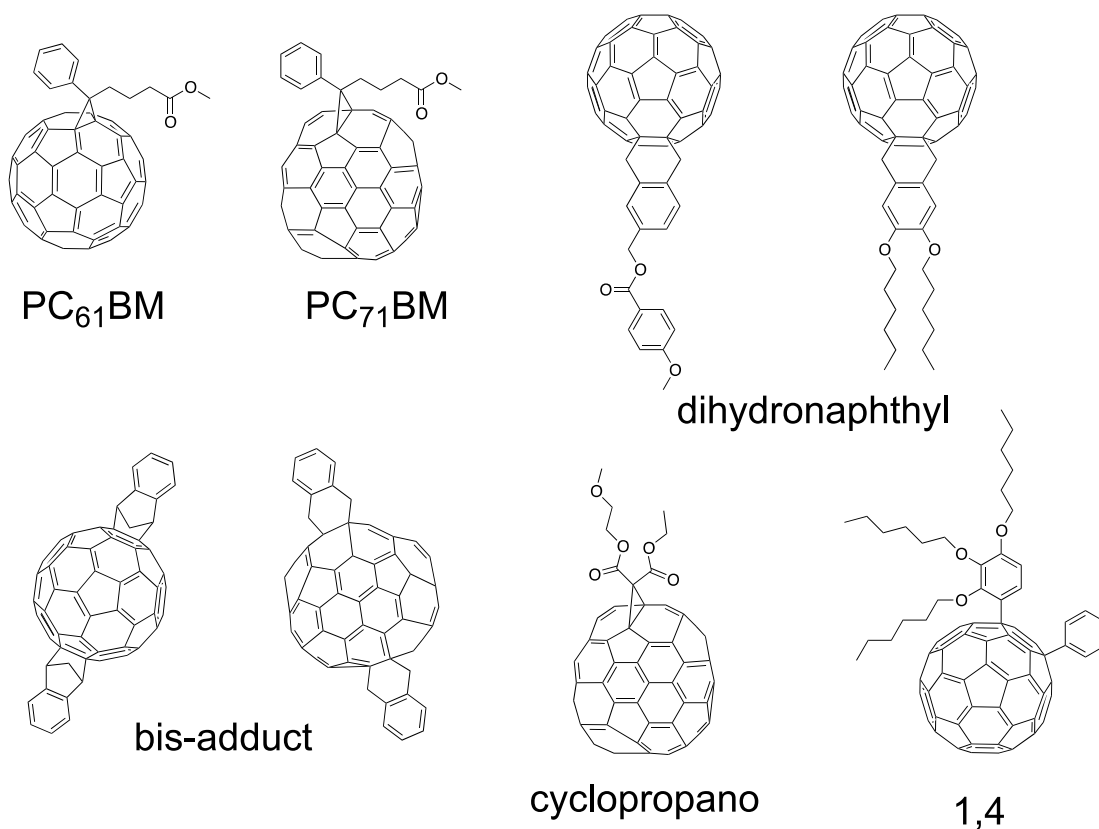


Figure 1-10. Various fullerene derivatives that have been used as acceptors in BHJ OPVs recently— PC₆₁BM;⁶³ PC₇₁BM;²³ and dihydronaphthyl,^{24,64} bis-adduct,^{65,66} cyclopropano,⁶⁷ and 1,4 fullerene derivatives.⁶⁸

1.2.2.2 Device Operation

The discussion of electrical properties, transport, and choice of materials for use in optoelectronics brings us to the operation of an OPV device. As shown in Figure 1-8b, a simple OPV device consists of an organic layer sandwiched between two electrodes.

The bottom electrode (cathode) must be transparent and lie on a transparent substrate for adequate photon absorption from the sun's light. The choice of materials to compose the organic layer is crucial for device performance. The metal electrodes can be precisely chosen to obtain specific energy levels. The organic layer is a bit trickier, as the energy levels depend on the HOMO and LUMO levels of the donor and acceptor in the BHJ, respectively. These HOMO and LUMO levels play a crucial role in charge transport in the operation of a photovoltaic device.

The mechanism for the operation of an OPV device and the generation of a current from photoenergy is summarized in Figure 1-11. First, light absorption of a photon causes excitation of an electron in the donor, promoting it from the HOMO to the LUMO (Figure 1-11a). The excitation of an electron leaves a hole in the HOMO, and this bound electron-hole pair is termed an "exciton." Next, exciton diffusion to the donor-acceptor interface occurs (Figure 1-11b). Exciton lifetime is about 5 – 10 nm, thus crucial choice of donor and acceptor is necessary for fabricating devices with ideal mixing thermodynamics and thus morphologies in the solid state.^{69,70} Once the exciton is at the donor-acceptor interface, charge transfer occurs, with an electron transferred from the LUMO of the donor to the LUMO of the acceptor (Figure 1-11c). Next, the charges separate and transport to opposite ends of the device (Figure 1-11d). Finally, the charge collection of the holes and electrons occurs at the cathode and anode, respectively (Figure 1-11e), resulting in a current (Figure 1-11f).

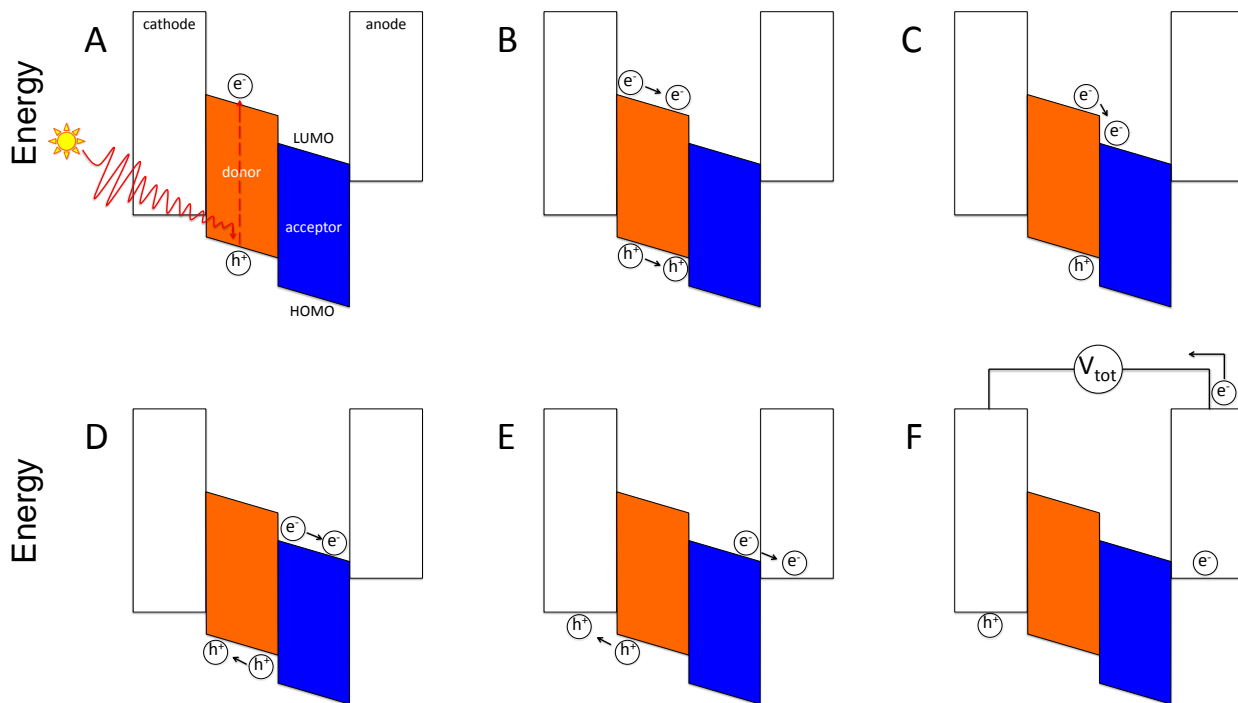


Figure 1-11. Mechanism of the conversion of photoenergy to a usable current in a photovoltaic device—light absorption and formation of an exciton (a), exciton diffusion to the donor-acceptor interface (b), charge transfer (c), charge separation and transport (d), charge collection at the electrodes (e), and the resulting usable current (f).

1.2.2.3 Quantification of OPV Parameters

In order for OPVs to compete with their inorganic counterparts in the industrial and consumer markets, PCEs must be increased. As mentioned in section 1.2.2.2, the conversion of photoenergy into a usable current is a mechanism of the electrons and holes in the BHJ. Essentially, an OPV is exposed to a simulated light source mimicking the photon flux of the sun's radiation. Next, a bias is applied and the current passing through the device is measured. This process is discussed in greater depth in chapter 2. Once a pixel is measured, we can plot a current density-voltage curve to quantify the PCE. A sample current density-voltage curve is shown in Figure 1-12, with the parameters of interest labeled on the curve for the purposes of this discussion.

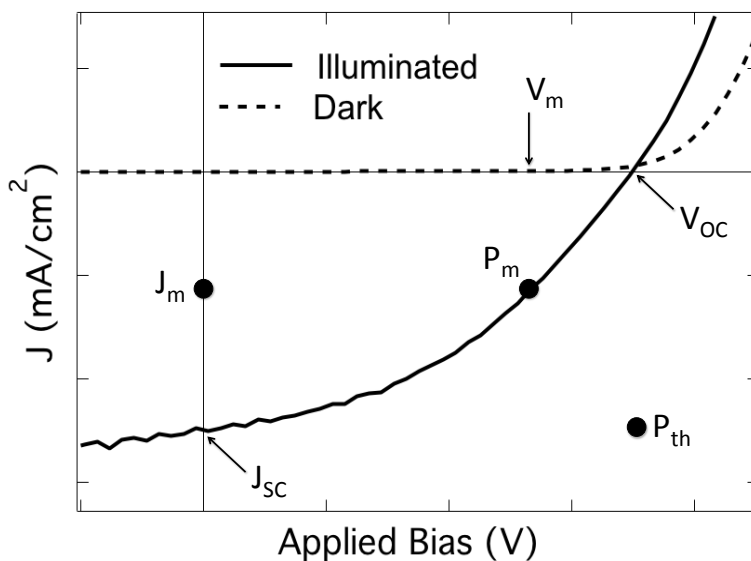


Figure 1-12. Sample J-V curve of illuminated and dark current, with all parameters of interest labeled for the calculation of the PCE in Equation 1-19.

We begin the quantification of the PCE by referring back to the mechanism by which an OPV device operates (Figure 1-11). In Figure 1-11d, the charges separate and the holes travel to the cathode and the electrons travel to the anode. The energy difference between the two is estimated as the energy difference between the HOMO of the donor and the LUMO of the acceptor, and is what contributes to the photovoltage or open circuit voltage (V_{oc}). Next, in Figure 1-11e, charge collection occurs at the electrodes. The density of holes and electrons collected contributes to the photocurrent, which accordingly is the product of the current density and voltage at any given point on the curve. Thus, the maximum power generated (P_m) must be the product of the maximum voltage and maximum current density,

$$P_m = J_m V_m \quad (1-15)$$

This brings us to the fill factor (FF), which is the ratio of the actual maximum power to the theoretical maximum power. The theoretical maximum power (P_{th}) is the product

of the short circuit current density (J_{SC}) and the open circuit voltage (V_{OC}), where the short circuit current density is defined as

$$J_{SC} = \frac{hc}{q} \int \frac{P_{1.5G} \cdot EQE}{\lambda} d\lambda \quad (1-16)$$

Where h is Planck's constant, 6.6261×10^{-34} J s, c is the speed of light, 2.9979×10^8 m s^{-1} , q is the electronic charge, $P_{1.5G}$ is the power of the AM1.5G filtered simulated light source, which is typically used in a laboratory setting to test PV devices (see section 2.4.1.1), the external quantum efficiency (EQE) is the ratio of the collected electrons contributing to the generated current to the incident photons of the power source, and the integration of $d\lambda$ is over the active spectrum of wavelengths, λ . Thus, the fill factor can be calculated by

$$FF = \frac{P_m}{P_{th}} = \frac{J_m V_m}{J_{SC} V_{OC}} \quad (1-17)$$

This brings us to the PCE (η), which is the ratio of the power produced (P_{out}) by the cell to the incident power (P_{in}):

$$\eta = \frac{P_{out}}{P_{in}} \quad (1-18)$$

Combining Equations 1-15, 1-17 and 1-18, we arrive at a useful expression for the calculation of the PCE of an OPV device using easily obtainable parameters from the characteristic J-V curve (Figure 1-12):

$$\eta = FF \frac{J_{SC} V_{OC}}{P_{1.5G}} \quad (1-19)$$

To increase PCE, many optimization efforts have been made to maximize FF, J_{SC} , and V_{OC} in devices. However, as with the majority of science, there is a trade-off when increasing a parameter, resulting in increased PCEs being more difficult to obtain.

1.3 Organic Light-Emitting Diodes

To continue the discussion of organic electronic devices, we will shift gears towards the other portion of this work, organic light-emitting diodes (OLEDs).

1.3.1 Background and Motivation

Lighting displays have been playing crucial roles in communication and entertainment in today's world of multimedia. Currently, there are a variety of displays widely used today—liquid crystal displays (LCD),⁷¹ plasma display panels (PDP),⁷² cathode ray tubes (CRT),⁷³ digital light processing projectors (DLP),⁷⁴ and light-emitting diode displays (LED).⁷⁵ Many of these technologies, however, have disadvantages—to name a few—PDPs produce copious amounts of heat, DLPs are difficult to view in well-lit areas, CRTs are bulky and heavy, and LCDs have limited viewing angles.

Recently, LEDs have been making more and more appearances in the consumer market in the form of TVs, computer monitors, and large area displays. LEDs are advantageous as they may be used to fabricate thin—and consequently lightweight—displays. The focus of this work is the study of OLEDs, a class of light-emitting diodes based upon organic materials.

The realization of electroluminescence—the phenomenon of light emission under an induced electric field—in organic materials was by Bernanose 1953 when studying gonacrin, acridine orange, and carbazole.⁷⁶ This work is what initially gave rise to the fabrication of multilayer OLEDs studied today.^{77,78} Displays based on OLEDs are exciting—compared to their counterparts discussed above—as they may have lower power consumption, materials can span the entire visible spectrum, thinner and lightweight displays are possible, and they have a larger viewing angle.

1.3.2 Organic Light-Emitting Devices

A basic OLED has a simple vertical architecture consisting of an electron transport emissive layer and a hole transport layer sandwiched between two metal electrodes on a transparent substrate (Figure 1-13). To obtain full light emission, the bottom electrode must be a transparent metal oxide, typically ITO. Multilayer structures are highly researched, however are not the focus of this work.

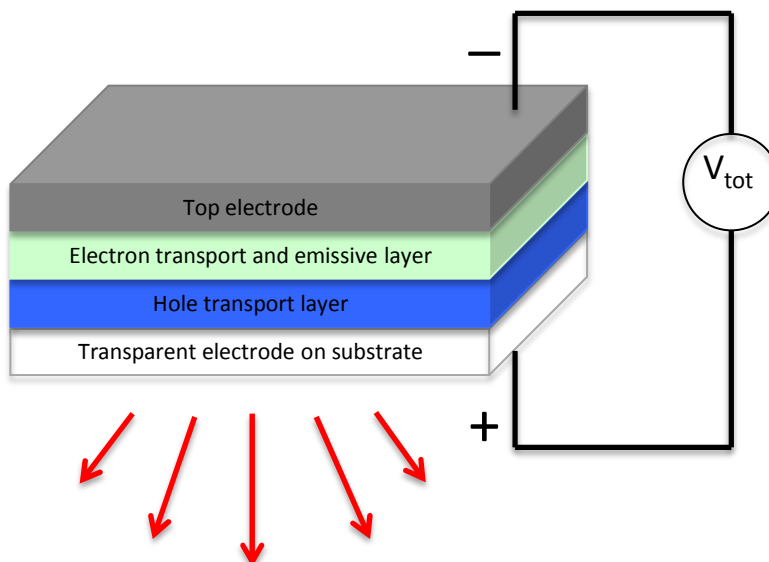


Figure 1-13. Schematic of a simple OLED device.

1.3.2.1 Materials

Choice of electroluminescent organic materials for use in LEDs is crucial for fabricating bright, high performing devices. Most organic materials used for LEDs are π -conjugated systems. As will be discussed in the proceeding section, balanced electron and hole mobilities must be achieved for proper charge recombination and light emission. Some selected hole transport and electron transport layers that can be found in the literature are summarized in Figures 1-14a and 1-14b, respectively.

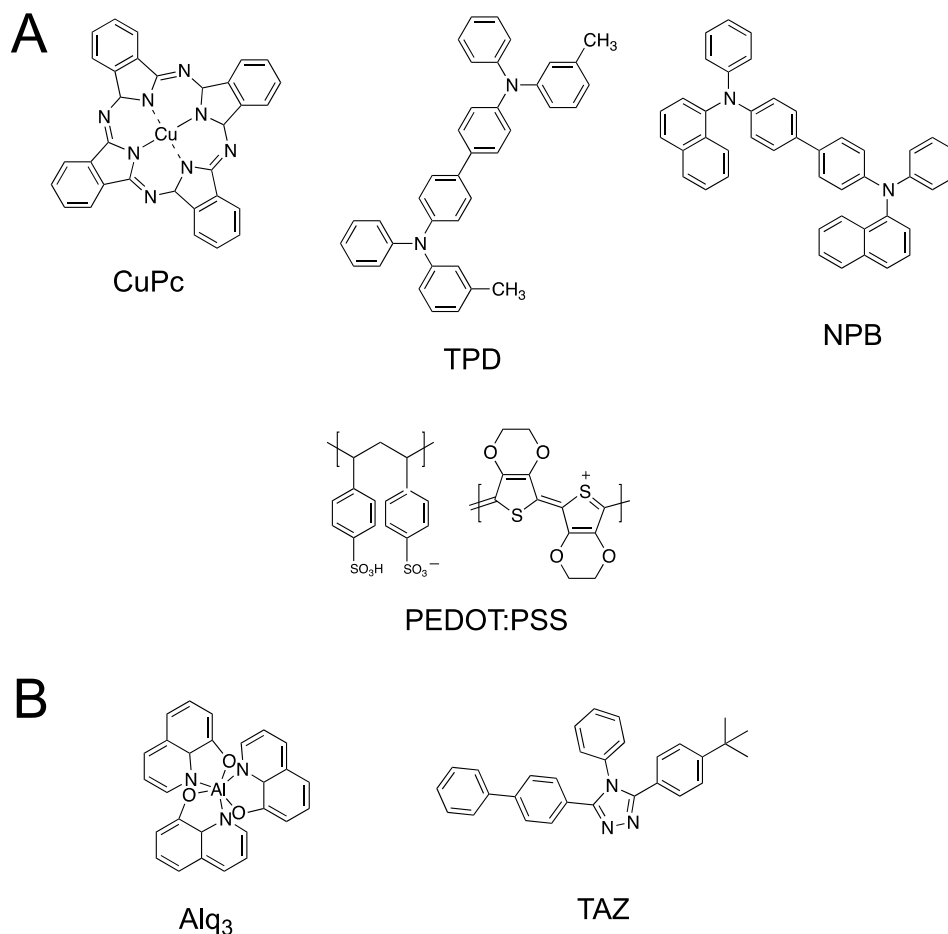


Figure 1-14. A variety of hole transport (a)—CuPc,⁷⁹ TPD,⁸⁰ NPB,⁸¹ PEDOT:PSS,¹⁵— and electron transport (b)—Alq₃,⁸² TAZ,⁸³—layers found in the literature.

It can be seen from Figure 1-14a that aromatic amines are excellent choices for hole-transporting materials. In chapter 4 we will explore a new class of aromatic amines as hole-transporting layers for controllable charge mobility. The list of hole and electron transporters presented in Figure 1-14 should not be interpreted as complete, as new molecules and derivatives of existing transporters are investigated daily. The possibilities for hole and electron transport materials are endless, perhaps the reason why the field of OLEDs is so exciting.

1.3.2.2 Device Operation

The operation of a basic OLED is summarized in Figure 1-15. First, a bias is applied, injecting electrons and holes at the cathode and anode, respectively (Figure 1-15a). Choice of electrodes is crucial for efficient charge injection. A low work function metal—1 nm lithium fluoride on 100 nm aluminum was used in this work—is needed for the cathode to inject electrons. For the anode, a high work function electrode—typically ITO—is needed to inject holes. ITO was used in this work as it is widely used and known as a good hole injector and it can be purchased pre-patterned on substrates relatively cheap.^{33,84,85} However, any other transparent metal oxide will do just fine as long as the work function is properly lined up with the HOMO of the emissive layer for proper hole injection. Once in the emissive layer, charge transport occurs (Figure 1-15b), followed by charge recombination to form an exciton (Figure 1-15c), resulting in light emission (Figure 1-15d).

When testing OLEDs in a laboratory setting, many parameters are of interest—electroluminescence, luminance, and EQE. These parameters and their calculations are discussed in great detail in section 2.4.2.

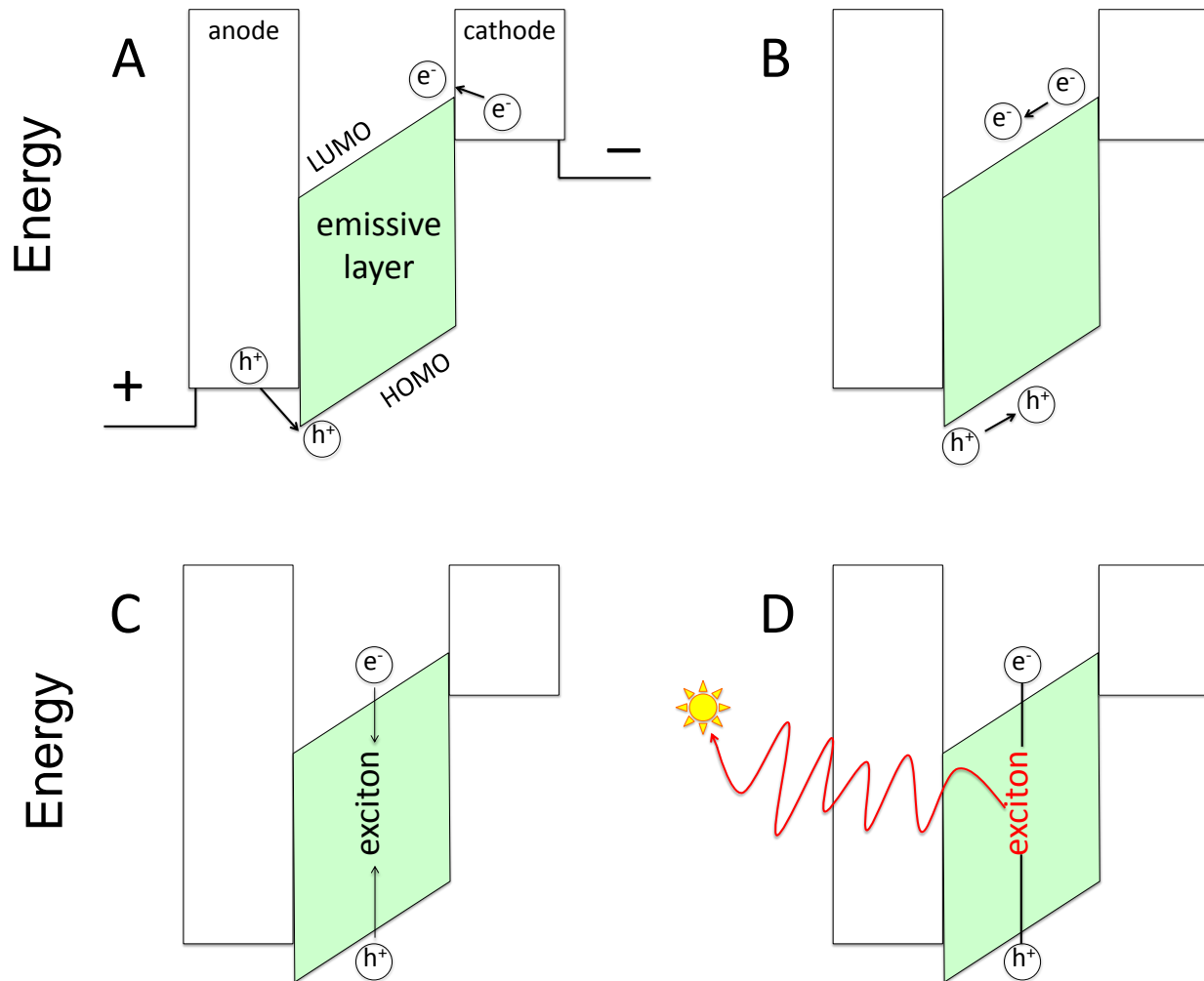


Figure 1-15. Mechanism of the emission of light from an applied bias in an OLED— charge injection (a), charge transport (b), charge recombination and formation of an exciton (c), and the resulting emission of light (d).

CHAPTER 2 EXPERIMENTAL TECHNIQUES AND INSTRUMENTATION

2.1 Introduction

Voids and impurities can be detrimental to electronic device performance and stability. Careful and sterile processing techniques and materials are crucial to fabricating quality devices. This chapter will discuss in detail the materials and methods used in device fabrication and characterization. All procedures discussed in this chapter were carried out in the Materials Chemistry Characterization Laboratory at the University of Florida, unless specifically noted otherwise.

2.2 Materials & Purification

2.2.1 Materials for Glovebox Use

Much of the device fabrication and characterization process took place in a custom built MBraun glovebox (project # 05-245) containing an Argon (Airgas South, cat. # ARHP-300) atmosphere. Oxygen and water levels in the glovebox were maintained at <0.1 ppm throughout experimentation. The glovebox catalyst used for removal of residual oxygen and water was regenerated approximately every three months using nitrogen gas balanced with 4% hydrogen (Airgas South, cat. # NI-HY4200).

2.2.1.1 Synthetic Materials for OPVs and PLEDs

For photovoltaics, the modified fullerene derivative used as an electron acceptor, [6,6]-phenyl-C₆₁-butyric acid methyl ester (PC₆₁BM), was purchased from nano-C (>99.5% purity, cat. # Nano-PCBM-BF). Isoindigo based oligomers used as electron donors in OPVs—il(TT)₂ and asymmetric derivatives—were synthesized by Romain Stalder and Dan Patel in the Reynolds' Group.⁸⁶ Brian Aitken of the Wagener Group synthesized all polymers used to prepare PLEDs in this work.^{87,88} Both small molecules

and polymers were synthesized in the George and Josephine Butler Polymer Research Laboratories at the University of Florida. Once purified and characterized, small molecule organics and polymers were immediately introduced into the Ar glovebox, where they were stored until further use in device fabrication. Polyfluorene-based polymer containing vials were wrapped in aluminum foil to prevent photo-oxidation and the formation of fluorenone defects.^{18,17}

2.2.1.2 Freeze Pump Thawed Solvents

All devices—OPVs and PLEDs—presented in this work, were solution-processed from chlorobenzene. To ensure there was no dissolved water or oxygen in prepared solutions, chlorobenzene was purchased anhydrous and freeze-pump-thawed to remove residual oxygen content. Freeze-pump-thaw procedures were performed in a synthetic lab part of the UF Butler Polymer Research Laboratories, with the assistance of Frank Arroyave. Anhydrous chlorobenzene was purchased from Sigma Aldrich in 1L sure-sealed bottles (99.8%, cat. # 284513). To freeze-pump-thaw, a Schlenk flask was rinsed sequentially with toluene, acetone, and isopropanol; and baked in an oven overnight. A cannula (stainless steel tube and needle) was used to transfer chlorobenzene from the sure-sealed bottle to the Schlenk flask to ensure the solvent was not exposed to ambient air. Such removal of chlorobenzene was only performed twice per purchased bottle to ensure the sure-seal remained effective in preventing exposure to atmosphere. The Schlenk flask was never filled over half of its volume, as this may cause the flask to shatter during the freeze-pump-thaw process. Once the flask was filled with solvent, any residual oxygen in the flask was removed to prevent condensing liquid oxygen during the freeze-pump-thaw process. The flask was pulled under vacuum and a liquid nitrogen bath was used to freeze the solvent. Once frozen,

the solid thawed under vacuum using a lukewarm water bath. Thawing of the solvent resulted in deoxygenation, which was visually noticed by bubbling. This freeze-thaw cycle was performed approximately five times, or until the aforementioned bubbling ceased. After performing the freeze-thaw cycles and allowing the solvent to return to a manageable temperature, the Schlenk was backfilled with Ar and transferred into the Ar glovebox. The solvent was then transferred into smaller amber storage bottles, which were cleaned using the same procedure as the Schlenk flask described above. Caps of the amber bottles were sealed with Teflon tape and stored until further use.

2.2.1.3 Materials for Thermal Deposition

Tungsten evaporator boats coated in Alumina were purchased from R.D. Mathis (cat. # S35B-AO-W). These evaporator boats allow for thermal evaporation up to ca. 1200 °C, which is sufficient for all of the materials used in this work. Gold was purchased from a local supplier (National Coins, 2007 NW 43rd St., Gainesville, FL 32605, ph: 352-378-3983) in the form of coins (Canadian Maple Leaf, 99.99% purity). The University of Florida's Department of Chemistry machine shop cut the coins into ca. 2 mm pieces. Gold pieces were sequentially sonicated in hexanes, toluene, acetone, and 2-propanol; and were allowed to thoroughly dry prior to introduction to the Ar glovebox. Aluminum slugs, ca. 8.0 mm in length (99.99%, cat. # 40417) and redistilled calcium shots, <1 cm size (99.5%, cat. # 10127) were purchased from Alfa Aesar. Lithium fluoride powder (97%, cat. # 21827) was purchased from Acros Organics. Molybdenum (VI) oxide powder (99.99%, cat. # 203815) was purchased from Sigma Aldrich. All thermal evaporation materials were used as received without any further modifications, with the exception of gold.

2.2.2 Solvent Distillation

With an increasing stress being put on environmentally friendly chemistry, solvents were distilled to recycle their use. Since electronic device fabrication must be rid of all impurities, such solvent distillation was only performed for acetone and 2-propanol used in the cleaning of ITO coated substrates. This section will discuss the distillation process of selected solvents, which will be explicitly recognized in the Indium Tin Oxide Cleaning section of this chapter.

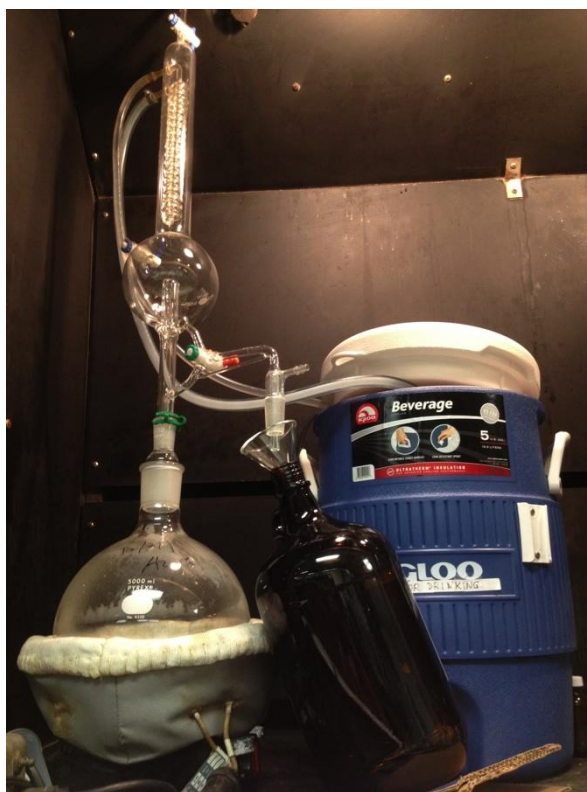


Figure 2-1. Solvent distillation column and cooling system setup.

To distill solvents, a 5-liter round bottom flask with a handful of boiling chips was filled with “dirty” solvent, presumably close to 100% purity (discussed in the ITO Cleaning section). A heating mantle (Glas-Col LLC.) coupled with a POWERSTAT Variable Transformer (The Superior Electric Co.) was set to a setting of 60 for acetone (ca. 56 °C) or to 90 for 2-propanol (ca. 83 °C). To cool the system, an external water

source is needed. To limit the amount of wastewater, which can be quite significant as typical distillations run upwards of four hours, water was recycled. A 5-gallon cooler was filled with tap water, which was treated with Chloramine-T Algicide (Ted Pella Inc, cat. # 18625) to prevent algal growth. A small fish pump used for commercial aquariums was connected to the intake tubing on the column and was submerged in the external cooler. The outtake tubing on the column was redirected into the cooler to allow for the water to infinitely cycle through the system. The distillation setup is shown in Figure 2-1. Once a reflux was obtained, the first approximate 20 mL of solvent was discarded to remove lower boiling point impurities. Distilled solvent was collected in 4-liter amber storage bottles, which were explicitly labeled. Distillation was ceased when approximately 50 mL solvent remained in the round bottom flask to leave behind any solid or higher boiling point impurities. It should be stressed that solvents used for distillation came only from ITO cleaning procedures, and no other sources. It is not recommended to recycle solvents from other laboratory usages for use in electronic devices.

2.2.3 Stir Bar Cleaning

Due to high cost and to limit waste, stir bars used for solution preparation were recycled, but nonetheless thoroughly cleaned. After being used in solution preparation, stir bars were immediately rinsed with toluene until visibly clean of residual organics. After rinsing, the stir bars were stored in an amber storage bottle filled with chloroform. Once an adequate number of stir bars was collected in the bottle, the chloroform was discarded and stir bars were rinsed again with chloroform, which was then discarded. The bottle was filled with chlorobenzene, heated to 140 °C, and stirred rigorously for two hours. The solvent was allowed to cool prior to being discarded. Once cool, the stir

bars were rinsed twice, sequentially in chloroform, toluene and 2-propanol. The stir bars were laid out on KimWipes and allowed to thoroughly dry for several hours to ensure evaporation of residual 2-propanol prior to introduction back into the Ar glovebox. Through conducting this work and reusing stir bars it was observed that they do not have an infinite lifetime. After extended use, it was realized that the magnetic material inside the stir bar was more visually evident, but had no apparent effect on device performance. Though the effects or cause of this was not investigated, such stir bars were discarded.

2.2.4 Glass Syringe Cleaning

With all electronic devices presented in this work being solution processed, with the majority of solutions needing filtration, a syringe is necessary to deposit the solution onto substrates. Prior to the work presented here, plastic syringes (Becton Dickenson Tuberculin) were used to deposit solutions onto substrates. Our group recognized an increase in OPV performance from using plastic syringes compared to glass syringes. Polydimethylsiloxane (PDMS) was acknowledged as a lubricant used in plastic syringes and was postulated as the reason for an increased PCE. This suspicion was confirmed by Matrix-assisted Laser Desorption/Ionization-Mass Spectrometry (MALDI-MS) and Infrared (IR) spectroscopy and PDMS was further investigated as a method to increase device performance in our group's previous publication.⁸⁹ Thus the work presented here utilized only glass syringes to ensure no impurities or enhancements during device fabrication.

After being used to deposit solutions in the glovebox, glass syringes were removed and immediately rinsed with toluene until visibly clean of residual organics. Rinsed glass syringes were stored in a beaker of clean toluene. Once the beaker was

full of syringes, the toluene was discarded and the syringes were rinsed with fresh toluene. The syringes were stacked upright in a new beaker, covered with methanol and sonicated for 15 minutes. The solvent was discarded and the sonication process was repeated sequentially with chloroform, toluene and 2-propanol. Syringes were blown dry of residual 2-propanol with compressed air and stored in a container lined with aluminum foil to be introduced back into the Ar glovebox.

2.3 Device Fabrication

The device fabrication techniques presented in this section were collectively optimized by Reynolds' group members and carried out with crucial detail to ensure sterile and reproducible procedures. It should be stressed that the times presented here are quite exact and slight deviations in device performance/quality were observed when straying from procedure.

2.3.1 Indium Tin Oxide Cleaning

Pre-patterned Indium Tin Oxide (ITO) coated glass slides (25 mm × 25 mm) were purchased from Kintec (www.kintech.hk) or Tinwell Technology Ltd. (www.tinwell.b2s.com) with a sheet resistance of 12 or 20 $\Omega \square^{-1}$ (Figure 2-2a).

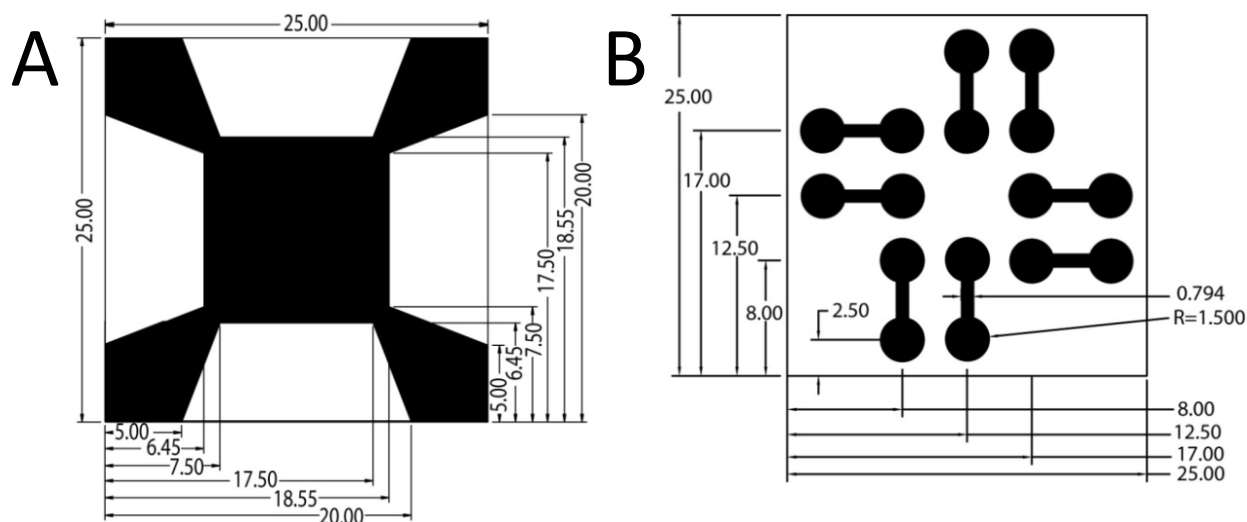


Figure 2-2. ITO pattern (a) and shadow mask pattern (b). For (a), black shows ITO and white shows glass. For (b), the black area shows the openings (where metals are deposited through) and white is the mask composed of brass. All measurements are in millimeters. Reprinted with permission from Ref 95.

A glass scribe was used to etch a device label on the non-ITO side of the substrate for easier identification. ITO-coated substrates were scrubbed using a KimWipe dipped in sodium dodecyl sulfate (SDS) (Sigma Aldrich >99%, cat. # L6026) solution. Substrates were stacked in a custom device holder assembled by the UF Department of Chemistry machine shop, which can hold up to sixteen 25 mm x 25 mm substrates. Once in the holder, the devices were submerged in SDS solution and sonicated for 15 minutes. After sonication, SDS solution was discarded and the substrates were rinsed seven times with deionized water, and five times with 18.2 M Ω MilliQ water. The substrates were submerged in 18.2 M Ω water and sonicated for 15 minutes. Substrates were then rinsed and covered with acetone and sonicated again for 15 minutes. After sonication, the acetone was stored in a 4-liter amber bottle labeled “dirty acetone” for distillation (see Solvent Distillation section). The process for acetone was repeated exactly with 2-propanol. During this work, it was noticed that discarding

the 2-propanol immediately following sonication caused residual solvent to dry on the surface of the substrates. The effect of this was not investigated, but rather substrates were blown dry with filtered nitrogen gas immediately after removal from 2-propanol. The substrates were placed in a vacuum chamber (Harrick model # PDC-32G) under a particle-free hood assembled by Dr. Nate Heston, and evacuated using a vacuum pump coupled with a dry ice/2-propanol cold trap. Detailed experimental procedures and specifications of the particle-free hood can be viewed in Dr. Nate Heston's Ph.D. dissertation.⁹⁰ Once under vacuum, the chamber was backfilled with pure oxygen and evacuated. This was repeated three times to ensure only pure oxygen in the chamber. The RF coil was turned to high, exposing substrates to oxygen plasma for two 10-minute intervals, with a 10-second pure oxygen purge between the two. Treating the ITO surface with oxygen is known to enhance surface wetting, improve stoichiometry, and modify ITO's work function; however, degradation of these effects is observed overtime.^{91,92} To ensure proper energy levels and oxygen rich ITO, substrates were further processed immediately. Procedures following oxygen exposure are specific to the device being fabricated. The procedure will continue in the following three subsections for photovoltaic devices, light-emitting diodes, and space charge limited current devices.

2.3.2 Photovoltaic Devices

Following oxygen exposure, substrates were immediately transferred to the stage of a spin coater (Laurell Technologies Co. model # WS-400BZ-6NPP/LITE), which was under the particle-free hood described before. The device was secured by vacuum and a nitrogen purge gas valve was turned on. Poly(3,4-ethylenedioxythiophene) poly(styrene sulfonic acid) (PEDOT:PSS, Baytron P VP Al 4083) was filtered through

0.45 μm nylon filters (Whatman) and deposited onto oxygen treated substrates. The substrates were spun cast for 40 seconds with a 3 second ramp at 5000 rpm. A cotton swab dipped in 18.2 M Ω water was used to wipe the corners of the substrate. Since PEDOT:PSS is in an aqueous solution, the water dissolves the film, exposing the conducting ITO surface on the corners which was later used as an electrode contact for the negative bias during characterization. PEDOT:PSS-coated substrates were immediately introduced into the Ar glovebox and baked on a hotplate at 130 $^{\circ}\text{C}$ for 20 minutes. Substrates were allowed to cool on aluminum blocks prior to storage in individual plastic containers until further processing. PEDOT:PSS treated substrates were used within one week of fabrication.

All active layer solutions for photovoltaic devices were prepared in the Ar glovebox. For all photovoltaic cells presented in this work, acceptor (PC_{61}BM) and donor (isoindigo based oligomers) solutions were prepared separately at 20 mg mL^{-1} in chlorobenzene solution and allowed to stir overnight. Three hours prior to spin casting, acceptor and donor solutions were heated to 60 $^{\circ}\text{C}$ and stirred for an hour and a half. Solutions were combined for the desired fullerene:isoindigo ratio and heated to 60 $^{\circ}\text{C}$ and stirred for an hour and a half to ensure complete dissolution.

Active layer solutions were deposited onto PEDOT:PSS coated substrates using a glass syringe with a 0.45 μm PTFE filter (Whatman) and spun cast for 60 seconds with a 3 second ramp at 1000 rpm. Active layer coated substrates were thermally annealed on a hotplate at 100 $^{\circ}\text{C}$ for 20 minutes. After cooling on aluminum blocks, substrates were transferred to a thermal deposition chamber using a custom-built device holder (Figure 2-3). The chamber was evacuated using a roughing pump and a

turbomolecular pump. The chamber was allowed to pump down for at least four hours, but no longer than twelve hours prior to top electrode deposition to ensure evaporation of any residual solvent in the film. Once the deposition chamber reached a pressure of 1×10^{-6} mbar, metal electrodes were deposited. All photovoltaic cells presented in this work received 10 nm of calcium followed by 100 nm of aluminum as the cathode. Calcium was deposited at a rate of 1.0 \AA s^{-1} and aluminum was deposited at a rate of 2.0 \AA s^{-1} . Once evaporation begun, shutters were not opened immediately, but rather a few nanometers of metal were allowed to evaporate to remove any impurities that might have been present. Controlled deposition was achieved through shadow masks defining 8 pixels per device with active areas of 0.0707 cm^2 each (Figure 2-2b). After deposition, the chamber was refilled with Ar and devices were removed and stored in individual plastic containers, wrapped in aluminum foil until characterization.

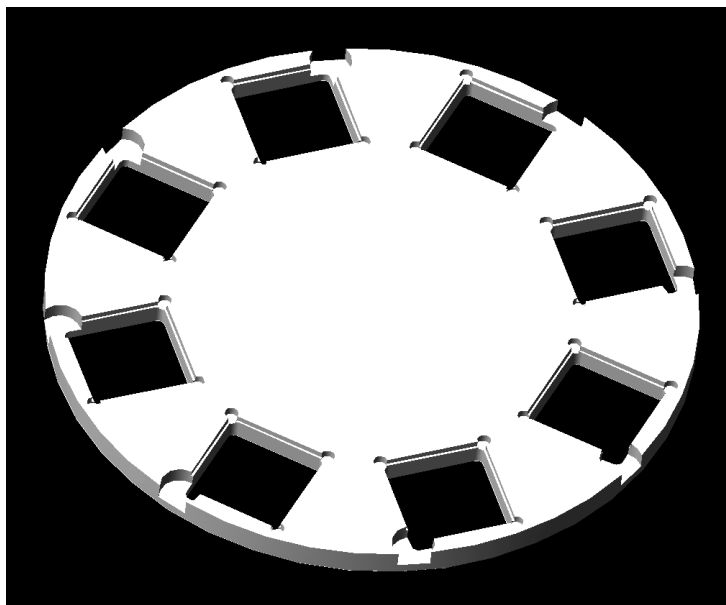


Figure 2-3. SolidWorks model of the device holder used for thermal deposition. Inset grooves measure 25.2 mm to house shadow masks (Figure 2-2b). Reprinted with permission from Ref 90.

2.3.3 Light-Emitting Diode Devices

The procedure of PEDOT:PSS deposition and annealing for photovoltaic cells was identical for light-emitting diode devices. Active layer solutions of polymers were prepared at 15 mg mL⁻¹ chlorobenzene and allowed to stir overnight. Solutions were deposited on PEDOT:PSS coated substrates using a glass syringe and a 0.45 μm PTFE filter (Whatman). Substrates spun cast for 60 seconds with a 3 second ramp at 1000 rpm. Substrates were then transferred to the thermal deposition chamber discussed before and received a layer of 1 nm lithium fluoride followed by 100 nm aluminum. Lithium fluoride was deposited at a rate of 0.1 Å s⁻¹, and aluminum was deposited at a rate of 2.0 Å s⁻¹. The same shadow masks were used for LEDs that were used for OPVs (Figure 2-2b). Devices were removed from the deposition chamber and stored in individual plastic containers wrapped in aluminum foil until characterization. Since all instruments used for light-emitting diode characterization were located outside of the glovebox, devices were removed one at a time and tested immediately to ensure minimal exposure to ambient air.

2.3.4 Space Charge Limited Current Devices

As discussed in chapter 1, the SCLC method is very useful in measuring charge-carrier mobilities in organic electronic devices. However, the model cannot measure charge carriers in tandem, thus the fabrication of hole-only and electron-only devices is necessary.

2.3.4.1 Hole-only Devices

For hole-only devices, either PEDOT:PSS or MoO₃ was used as the hole injection layer, and gold as the hole collecting layer. For PEDOT:PSS containing devices, the same procedure was followed as that for OPVs and LEDs for PEDOT:PSS deposition

and annealing. For MoO₃ containing devices, substrates were brought into the glovebox immediately after oxygen plasma exposure (see ITO Cleaning section). Substrates were loaded into the evaporation chamber without any shadow masks to deposit the MoO₃ layer on the entire surface of the device. Since the substrates hadn't received any organic layers yet, the evaporator was only evacuated for approximately 45 minutes to a pressure of 1×10^{-5} mbar. A layer of 7 nm MoO₃ was deposited at a rate of 0.3 \AA s^{-1} . Upon removal of MoO₃ coated substrates from the evaporation chamber, the active layer was immediately spun cast to ensure proper energy levels, with no shifting.³⁶ Solutions for SCLC devices were prepared in the same fashion as for OPVs and LEDs, however at a concentration of 25 mg mL^{-1} . Active layer solutions were spun cast on PEDOT:PSS or MoO₃ coated substrates for 60 seconds with a 3 second ramp at 1000 rpm. Devices containing isoindigo-based oligomers were thermally annealed at 100 °C for 20 minutes after spin casting. Substrates were transferred into the evaporation chamber, which was evacuated for a minimum of four hours. Once a pressure of 1×10^{-6} mbar was achieved, 70 nm of gold was deposited through the same shadow masks that were used for OPVs and LEDs (Figure 2-2b). Gold was deposited at a rate of 1.0 \AA s^{-1} . Devices were stored in individual plastic containers and wrapped in aluminum foil until characterization.

2.3.4.2 Electron-only Devices

For electron-only devices, Al was used as the anode and LiF/Al was used as the cathode. Substrates were brought into the Ar glovebox immediately after oxygen plasma exposure. Substrates were loaded into the evaporator using a different holder to deposit a patterned anode (Figure 2-4).

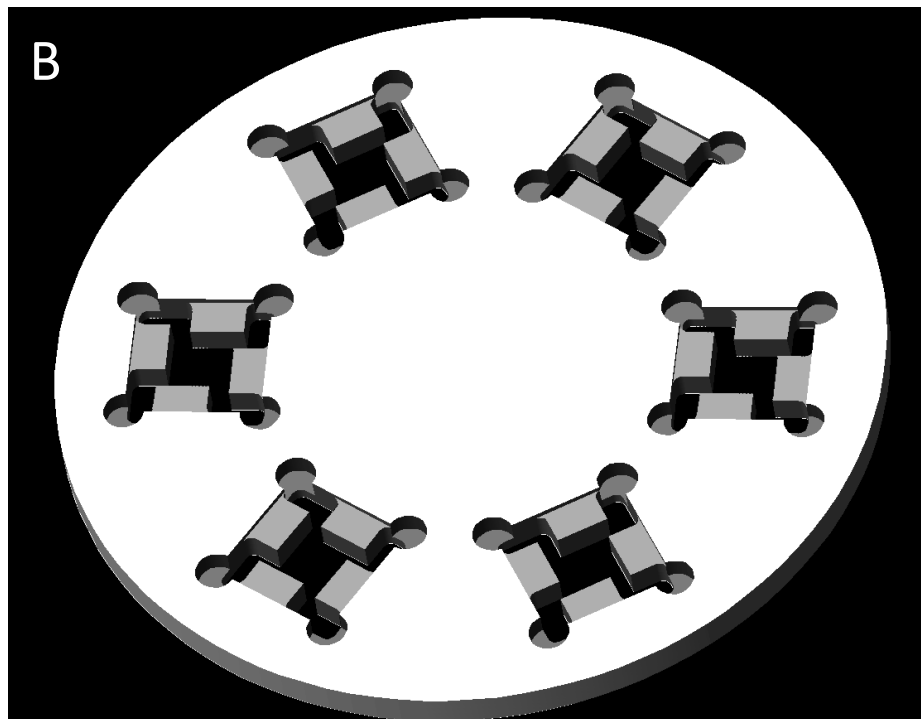
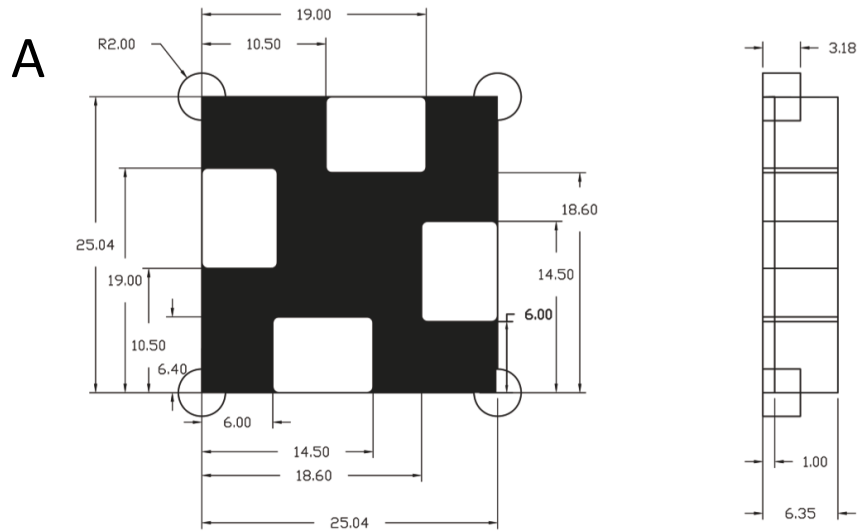


Figure 2-4. Schematic of patterned mask (a) and SolidWorks model of the evaporation device holder (b) used for anode deposition of electron-only devices. Reprinted with permission from Ref 90.

Opposed to hole-only devices, where the anode (MoO_3) was deposited on the entire surface, a patterned device holder was used to controllably deposit the aluminum anode for electron-only devices. Depositing a patterned aluminum anode ensures no vertical overlap of aluminum anode and aluminum cathode in the resulting electron-only

device (Figure 2-5). Electron-only devices with such an overlap were observed to have the majority of the pixels short when testing. Once the evaporation chamber reached a pressure of 1×10^{-6} mbar, substrates received 100 nm of Al at a rate of 2.0 \AA s^{-1} as the anode. Active area solutions were prepared and deposited using the same procedure as hole-only devices. Electron-only devices received 1 nm LiF and 100 nm Al as the cathode. LiF and Al were deposited at the same rates as for LEDs. The same shadow masks were used as before for cathode deposition (Figure 2-2b). Devices were stored in individual plastic containers, wrapped in aluminum foil until characterization.

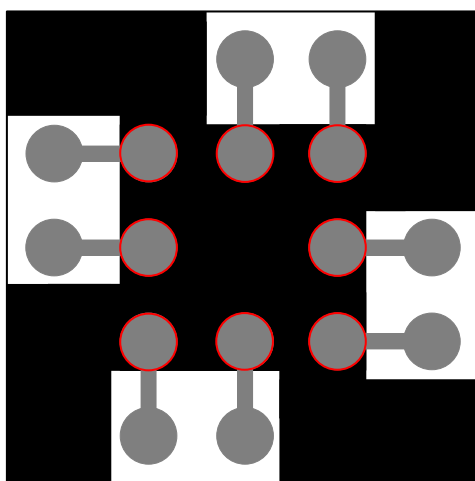


Figure 2-5. Schematic of an electron-only device. Black shows the aluminum anode, gray shows the LiF/Al cathode, and red shows the active area (pixels).

2.4 Device Measurement

2.4.1 Organic Photovoltaics

2.4.1.1 Solar Simulation

In order for organic photovoltaics to compete with their inorganic counterparts, power conversion efficiencies must be improved. Quantifying the efficiency of a solar cell may not be as easy as going outside on a sunny day and simply applying a bias and measuring a photocurrent. Though this is possible and how devices would be

applied in the real world, simulated light may provide more accurate and reproducible characterization for laboratory purposes. This is because the profile of the sun's light can drastically change based on location and a variety of environmental factors including cloud content and seasonal variations. Additionally, the sun's radiation can be modified from the instance it leaves the sun to the point it reaches the cell. Such modifications may include scattering, and absorption or reflection, which alter the profile of the radiation. This results in light at an angle further away from zenith, a point directly above the opposition of gravitational force, appearing less bright.

Solar simulators have been manufactured to more accurately represent the qualities of sunlight for laboratory measurements, which follow air mass coefficient (AM) classifications. Numerous tables of air masses can be found in the literature, from which the AM factor is calculated.⁹³ Many different AM classifications can be calculated, though for the purpose of photovoltaic characterization, only the three most popular will be discussed: AM0, AM1.0 and AM1.5 (Figure 2-6).

The AM0 classification is an extraterrestrial spectrum, mimicking the sunlight prior to passing through the Earth's atmosphere. Then there are the terrestrial spectra, AM1.0 and AM1.5. The AM1.0 spectrum is that of light passing through the Earth directly orthogonal to the atmosphere, or 0° to the zenith angle. However, this would only accurately represent sunlight around the equator. The AM1.5 filter provides the profile of the sun passing through one and a half atmospheres, which is the equivalent of penetrating the atmosphere at an angle of 48.2° to the zenith. The AM1.5 spectra can be further characterized as direct or global, AM1.5D and AM1.5G, respectively. For AM1.5D, the radiation neglects any diffused radiation as described above, while

AM1.5G represents total ground radiation considering diffused and reflected factors. It is presumed that the AM1.5 filters most accurately represent sunlight in the continental United States and is thus used in this work to characterize all photovoltaic cells. For all experiments conducted for this work, a 150-watt xenon arc lamp (Newport 66902 lamp coupled with Newport 66907 power supply), filtered through AM1.5G was used to illuminate cells.

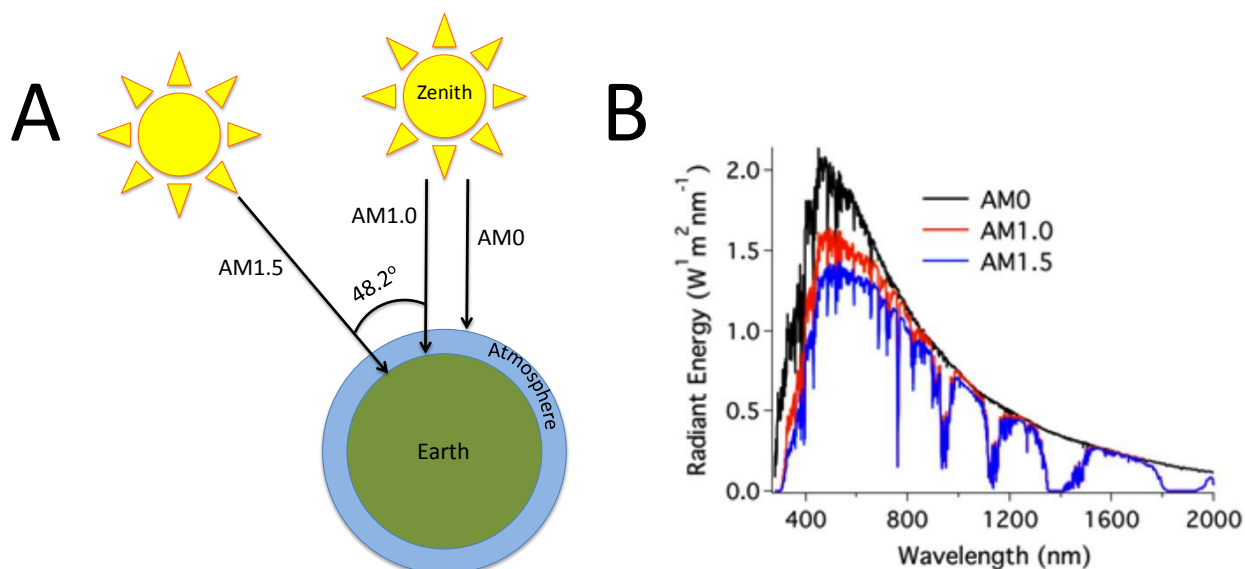


Figure 2-6. Schematic of the air mass conditions used for photovoltaic measurements (a) and their standard spectra (b). Image (b) reprinted with permission from Ref 95.

2.4.1.2 Power Conversion Efficiency

To measure photocurrent, individual pixels were irradiated with $100 \pm 1 \text{ mW cm}^{-2}$ solar simulated AM1.5G light (specifications described in the previous section) and a bias was applied from -1.0 V to +1.5 V (1 point per 0.02 V) using a Keithley 2400 Sourcemeter. Applying the same bias and covering the pixels from any light exposure measured the dark current. Current-voltage characteristics were collected using a custom written LabVIEW program. A custom excel template was used to plot current

density-voltage curves and photovoltaic parameters were extracted using the equations discussed in chapter 1.

2.4.2 Polymer Light-Emitting Diodes

To quantify polymer light-emitting diode performance, many characterization techniques were utilized. All instruments used for light-emitting diode characterization were outside of the Ar glovebox. Thus, devices remained inside individual plastic containers wrapped in aluminum foil inside the Ar glovebox until testing. Inside the Ar glovebox, a device was put inside a custom device holder fabricated by the UF machine shop (Figure 2-7). The device holder was used for all device testing, so there was no need to remove the device once inside the holder. The device holder containing the device was removed from the Ar glovebox and immediately tested, to limit the exposure to ambient air.

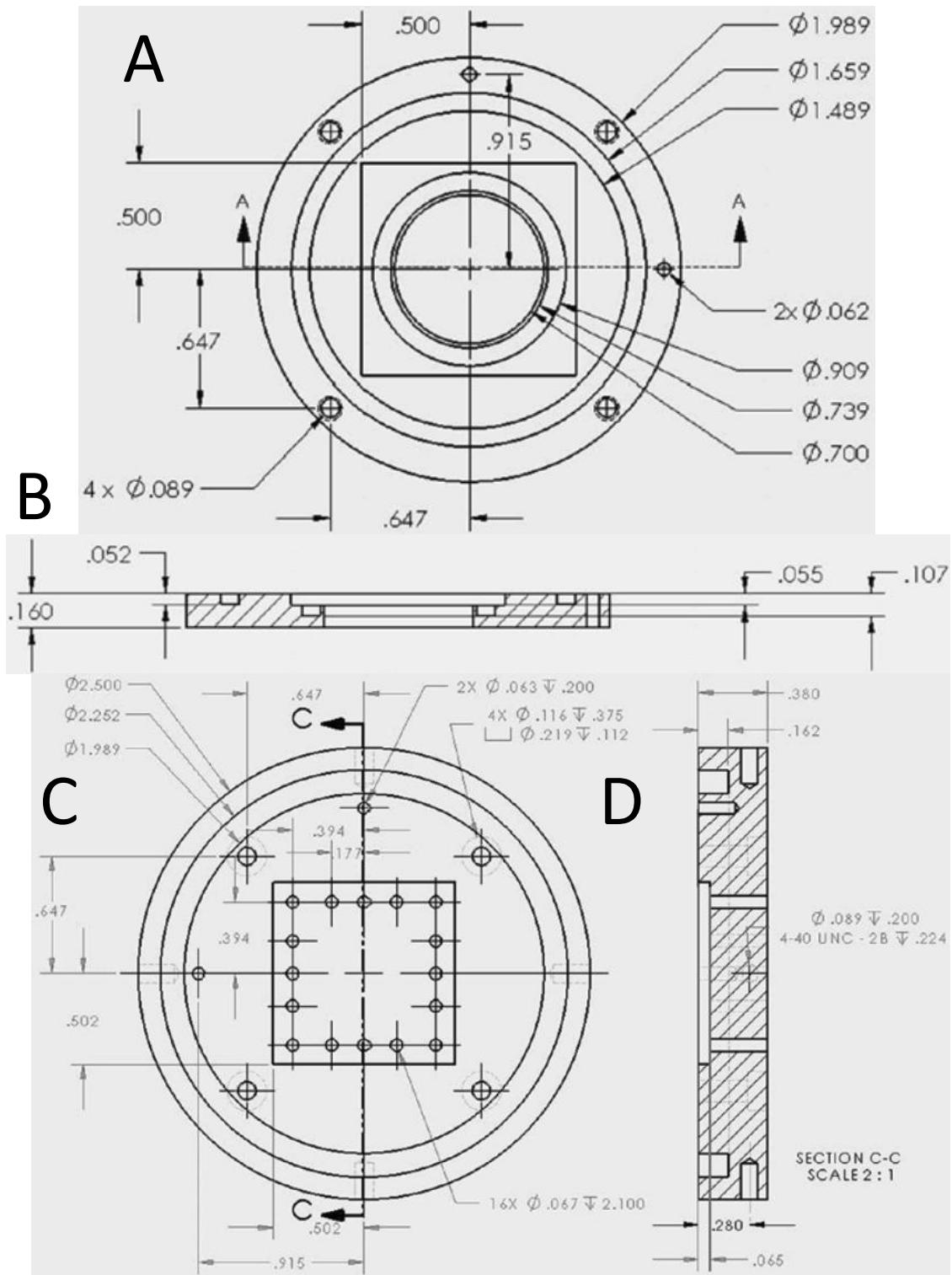


Figure 2-7. SolidWorks schematic of the top (a,b) and bottom (c,d) of the PLED device holder. All measurements are in inches. Reprinted with permission from Ref 95.

2.4.2.1 Electroluminescence

Light-emitting diodes exhibit an optical/electrical phenomenon called electroluminescence (EL), where light is generated upon induction of an electrical current. To record electroluminescence spectra, the PLED was placed inside the device holder (Figure 2-7), which was screwed into a stand on a workbench. The device holder was positioned so that the pixel of interest was directly orthogonal to the aperture opening on the spectrograph. A constant current was applied using a Keithley 2400 Sourcemeter, and spectra were obtained using an ISA-SPEX Triax 180 spectrograph equipped with a silicon charge-coupled device (CCD) detector, cooled to ~140 K with liquid nitrogen. The device was turned on for just enough time for spectra to be obtained, ca. 3 seconds (Figure 2-8). The maximum wavelength of emission was recorded, which was later used for performance testing (see PLED Performance section). For all reported EL spectra in this work, a correction file was applied after obtaining spectra.

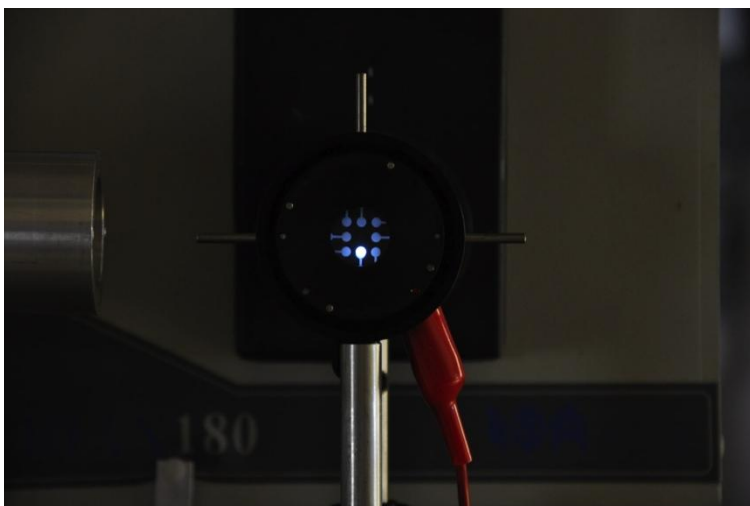


Figure 2-8. An illuminated PLED pixel under constant bias, viewed from the outside of the device holder.

2.4.2.2 Luminance

A PLED's brightness may be quantified by measuring its luminance (L_v), the total photometric flux on an element of surface per unit area. Luminance is a desired characterization quantity of optoelectronics as it effectively quantifies the way a human eye perceives the brightness of a light. To arrive at the luminance, we begin with the luminous flux (Φ_v), light's time rate of flow measured in lumens (lm):

$$\Phi_v = \int K_m \Phi_{e,\lambda} V(\lambda) d\lambda \quad (2-1)$$

Where K_m is a constant determined empirically (683 lm W^{-1}), $\Phi_{e,\lambda}$ is the radiant flux with respect to wavelength, and $V(\lambda)$ is the *spectral luminous efficiency for photopic vision*, a factor correcting for the human eye's visual perception applied at wavelengths from 360 to 830 nm.⁹⁴ The luminous intensity (I_v), the total photometric flux on an element of surface measured in candelas (cd), is defined by

$$I_v = \frac{\partial \Phi_v}{\partial \Omega} \quad (2-2)$$

Where $d\Omega$ is the propagating angle after the flux leaves the source (Figure 2-9).

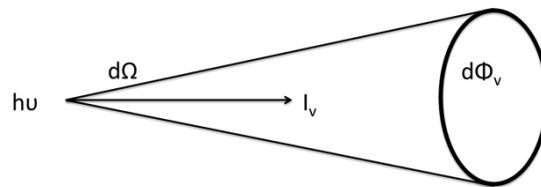


Figure 2-9. Luminous flux leaving the source, labeled with the parameters used to calculate luminance in Equation 2-3.

Finally, we arrive at the desired calculation of luminance, the luminous intensity (Equation 2-2) per unit area (cd m^{-2}).

$$L_v = \frac{\partial^2 \Phi_v}{\partial \Omega \partial A \cos \phi} \quad (2-3)$$

Where $dA \cos \phi$ accounts for the projected area of the surface orthogonal to the measurement direction (Figure 2-9).

To probe PLED brightness and true color, a calibrated Konica Minolta CS 100 luminance meter equipped with a No. 110 lens was used (Figure 2-10). The device holder containing a fresh PLED (Figure 2-7) was screwed into a stand mounted onto a workbench. Mounted on a tripod, the Minolta luminance meter was aligned directly orthogonal to the face of the device using a level. Using the eyepiece on the Minolta, the circular crosshair was aligned directly in the center of a pixel.

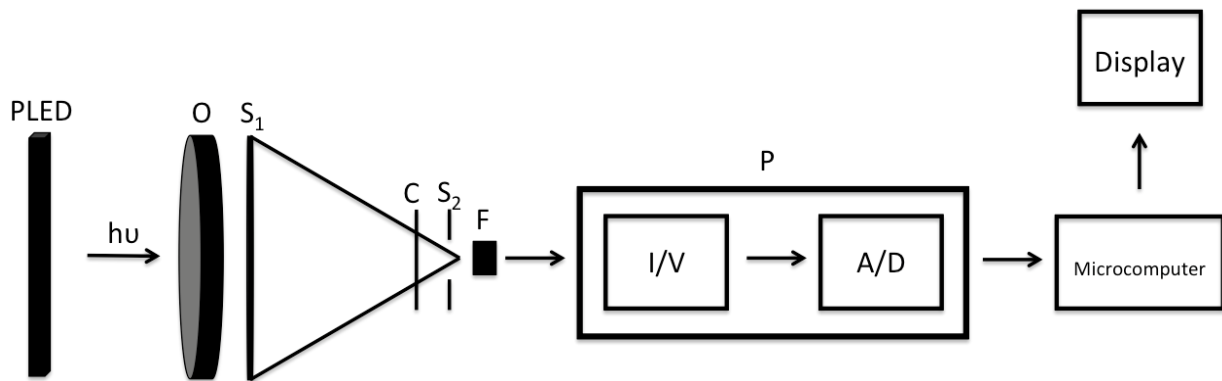


Figure 2-10. Block diagram of the Konica Minolta CS 100 luminance meter—objective lens (O), aperture stop (S_1), chopper (C), field stop (S_2), spectral-response correction filter (F), silicon photocell (P), current-to-voltage converter (I/V), and analog-to-digital converter (A/D).

To measure luminance, a constant bias was applied using a Keithley 2400 Sourcemeter, while simultaneously opening the aperture of the Minolta. The device was only powered on long enough for the Minolta to obtain a reading, ca. 4 seconds to prevent pixels from burning out or shorting. This process was done at 0.5 V steps and luminance values were recorded manually.

As light emits from the PLED, it travels through the objective lens and the aperture stop. The light then passes through the chopper, field stop and spectral-response

correction filter. Corrected light strikes the silicon photocell, where current is converted to voltage, transforming the analog signal to a digital output. The signal is processed by the integrated microcomputer, which carries out the necessary calculations to display on the screen.

In addition to luminance, the Minolta also provides color coordinates x and y , which follow CIE 1931 color space standards. Color coordinates for each 0.5 V step were manually recorded and plotted using the standard CIE 1931 color space chromaticity diagram (Figure 2-11). Such color coordinates allow for a way to determine the true color of an emitted light.

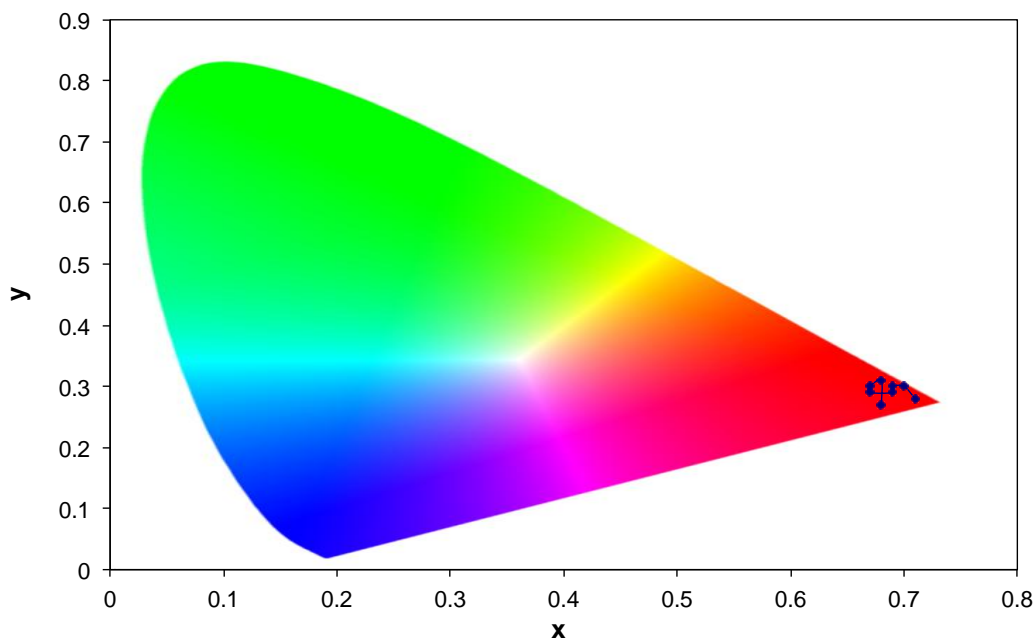


Figure 2-11. Example of a PLED's x and y coordinates, plotted using the standard CIE 1931 color space chromaticity diagram, showing a deep red color.

2.4.2.3 PLED Performance

Thus far we have looked at the optoelectronic phenomenon of the PLED as well as how to measure its brightness and true color. To conclude our discussion on PLED characterization, we now examine the external quantum efficiency (EQE), the ratio of

the number of photons the LED emits onto the surface to the total number of electrons injected in the device. However, to arrive at the EQE, we must first discuss the components. First we calculate the radiant emittance (R_v), the total flux incident on the surface per unit area ($W m^{-2}$) by

$$R_v = \frac{R_D}{A\phi} \quad (2-4)$$

Where R_D is the radiant flux detected, A is the active area, which was 0.0707 cm^2 (Figure 2-2b), and ϕ is the fraction of light collected, which was empirically determined to be 24.5 %.⁹⁵ Also, Planck's relation states that the energy of a photon (E) is inversely proportional to its wavelength emitted:

$$E = \frac{hc}{\lambda} \quad (2-5)$$

Where h is Planck's constant, $6.6261 \times 10^{-34} \text{ J s}$, c is the speed of light, $2.9979 \times 10^8 \text{ m s}^{-1}$, and λ is the wavelength emitted by the photon in meters. We can divide Equation 2-5 by Equation 2-4 to obtain

$$\frac{E}{R_v} = \frac{hc}{R_v\lambda} \quad (2-6)$$

Here, we have the energy of the photon per total power. Additionally, we have

$$\frac{\#electrons}{second} = \frac{I}{e} \quad (2-7)$$

Where I is the current injected and e is the elementary charge, $1.6022 \times 10^{-19} \text{ C}$. Since we defined the EQE as the ratio of the number of photons produced per number of injected electrons, we can combine Equation 2-6 and Equation 2-7 to arrive at the EQE:

$$EQE = \frac{\text{power out}}{\text{power in}} = \frac{R_v\lambda/hc}{I/e} = \frac{R_v\lambda e}{Ihc} \quad (2-8)$$

The EQE is typically reported as a percentage, where Equation 2-8 is simply multiplied by 100.

To probe PLED EQE experimentally, a fresh PLED was loaded into the device holder (Figure 2-7). The device holder was placed face down on a custom stage designed by Ken Graham and assembled by the UF machine shop, which housed a silicon photodiode. The silicon photodiode was attached to a UDT optometer (S471), which was connected to a computer and a sourcemeter. A bias was applied using a Kiethley 2400 Sourcemeter, and data was collected using a custom LabVIEW program written by Ken Graham. To calibrate the UDT, the emission peak obtained from the EL spectra was used. After testing, the LabVIEW program outputs a .txt file with the following parameters: applied voltage (V), radiant power emitted (μW), radiant emittance ($\mu\text{W cm}^{-2}$), current density (mA cm^{-2}), and EQE (%).

2.4.3 Charge-carrier Mobility Devices

As discussed, the SCLC model does an excellent job at probing electron and hole mobilities in organic thin films, though not simultaneously. To measure either electron or hole mobilities, a fresh device was loaded into the same holder used for OPV testing. A bias was applied using a Kiethley 2400 Sourcemeter and current-voltage characteristics were collected using a custom written LabVIEW program. For hole-only devices, a bias from 0 to +10 V (1 point per 0.025 V) was typically found to provide better current-voltage curves, and for electron-only devices, a bias from -10 to 0 V was used (same point per voltage as the positive bias). Current density-voltage data was plotted using IGOR Pro WaveMetrics programming software, which was used to extract charge-carrier mobilities using the field-dependent SCLC model (Equation 1-14).

2.5 Morphology Characterization

Morphology is extremely important in organic thin films, especially in photovoltaics when trying to gain a fundamental understanding of the correlation between

performance and nanostructure. Different processing techniques can contribute to an altered morphology, including solvent choice, spin rate, and annealing.^{96,97} Additionally, it was found that morphology varied based on the location on the device from which an image was taken, which will be discussed later. Many techniques are available to probe morphology of a thin film. The most common method in the field of organic electronics is Atomic Force Microscopy (AFM), which is a scanning probe microscope. Additionally, there are various electron microscopes and X-ray Photoelectron Spectroscopy (XPS) available for surface imaging. Those seeking a true fundamental understanding of nanostructure should be cautious when simply accepting the results from one morphology characterization technique. It will be shown in chapter 3 that Transmission Electron Microscopy (TEM) revealed features that were not visible from AFM imaging in certain devices.

2.5.1 Atomic Force Microscopy

2.5.1.1 Tapping Mode

Atomic Force Microscopy (AFM) is an excellent tool for probing surface profiles of thin films. AFM relies on the attractive or repulsive forces of a nanometer scale tip scanning just above the surface of a solid. The tip oscillates up and down without touching the surface and adjusts accordingly with the surface features with its flexible cantilever (Figure 2-12). As a result, AFM produces a surface topology image.

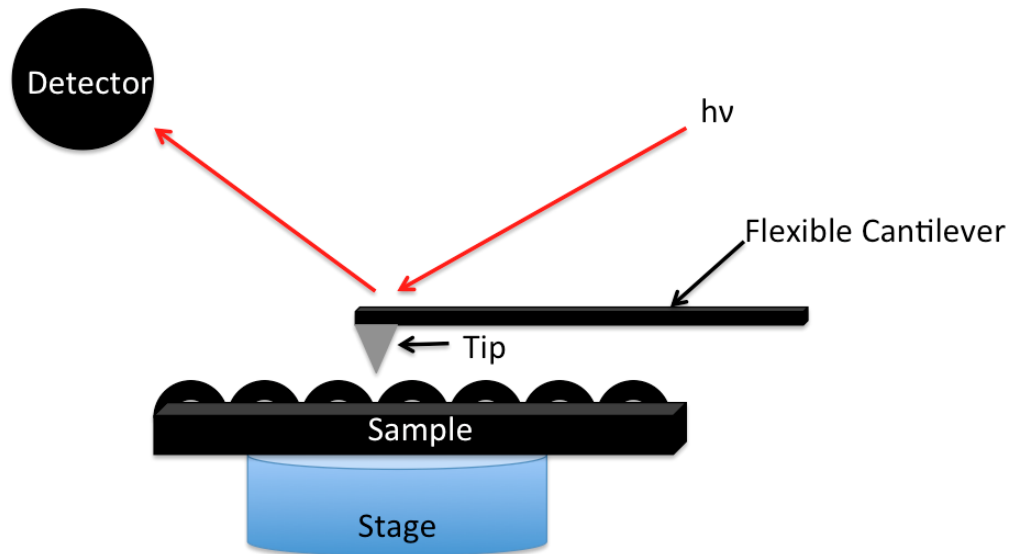


Figure 2-12. Schematic of an AFM.

To obtain AFM images for this work, a Veeco Innova scanning probe microscope in tapping mode was used. Cantilevers with a tip frequency of ~ 325 kHz and a force constant of ~ 40 N m⁻¹ (MikroMasch NSC15) were used. Representative images were taken within 2 mm of a pixel, where the active layer overlapped the ITO (Figure 2-2).

2.5.1.2 Position-dependent Morphology

In my earlier work with solar cells, a different ITO pattern and shadow mask was used, resulting in a different pixel layout (Figure 2-14d). AFM studies on these devices revealed a change in morphology based on the position of the device where the image was taken. This was recognized and further investigated when studying polymeric solar cells made with APFO-DOT, synthesized by Ünsal Koldemir of the Reynolds' group (Figure 2-13).⁹⁸

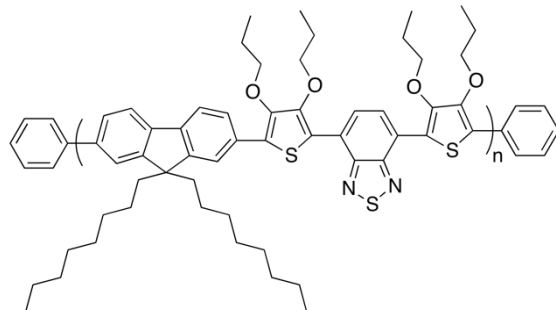


Figure 2-13. Structure of APFO-DOT synthesized by Ünsal Koldemir.

Positions A, B and C were assigned to areas on the device, with A being closest to the center of the device, and C being further towards the edge of the device (Figure 2-14). AFM images were taken at positions A, B and C on the same device, and a change in morphology was observed. It can be seen that the domains in the center of the device (A) are quite circular and very well defined. However, once we move towards the outside of the device (B then C), we see that the domains are spreading and distorting.

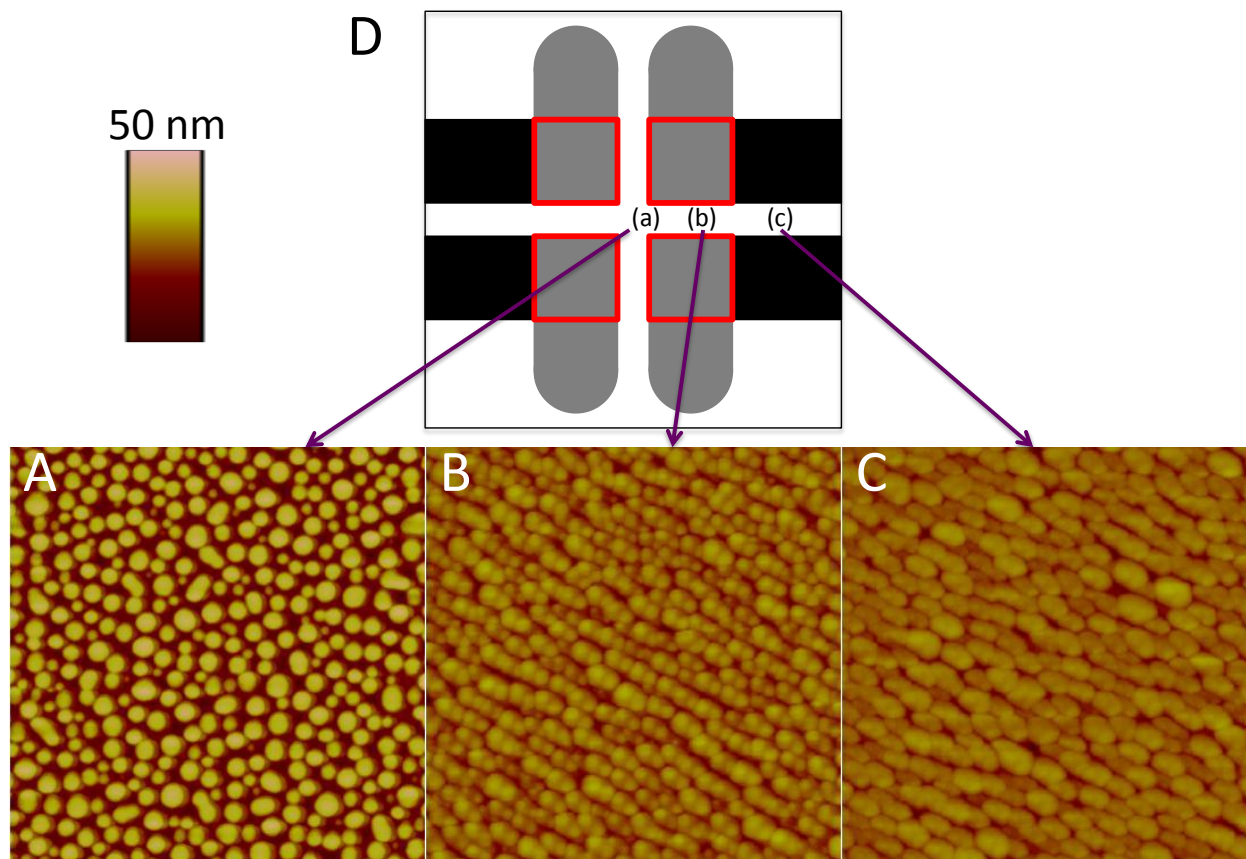


Figure 2-14. AFM images of APFO-DOT:PC₇₁BM (1:4) in chlorobenzene at the center (a), between the center and the edge (b) and towards the edge (c) of the device. The device ITO and cathode layout with the labeled A, B, and C positions (d). All AFM images are 5 μm \times 5 μm . For (d), black shows the ITO, gray shows the cathode, and the red box shows the active area (pixel).

Such a distortion in domain shape can be attributed to the classical mechanics of spin coating. As described in the Device Fabrication section, active layer solutions are deposited on devices using glass syringes. Once the solution covers the face of the substrate, spin coating commences. As the spin coater ramps up, centrifugal force pulls the solution away from the center of the device, and towards the edges of the device (Figure 2-15).

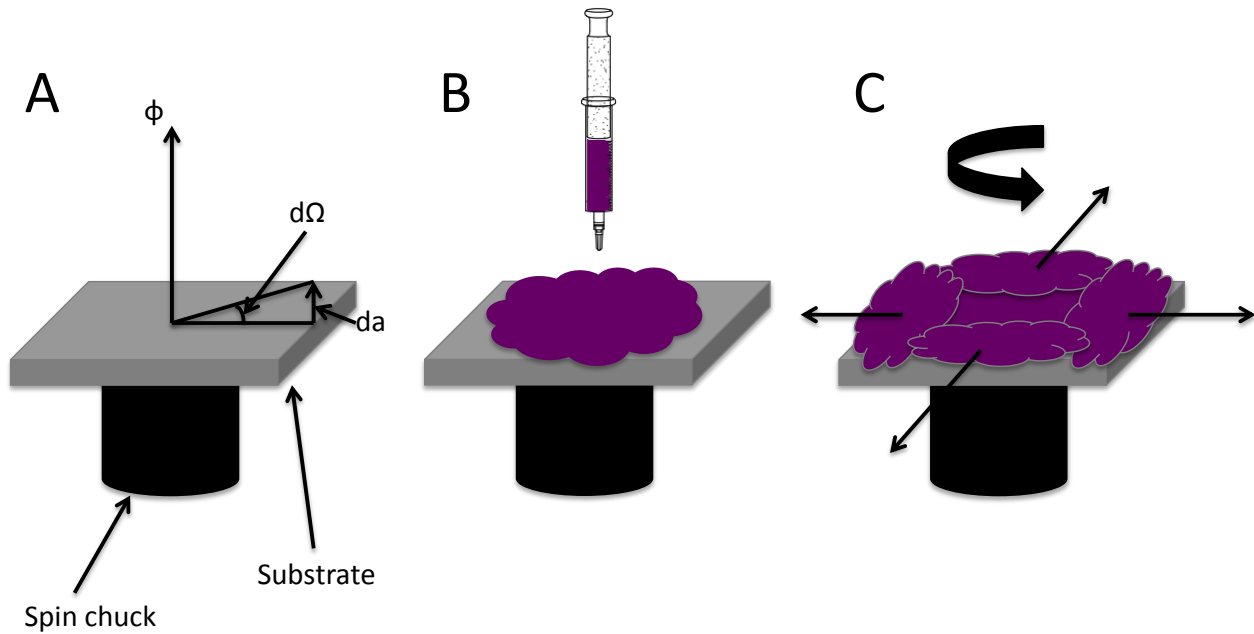


Figure 2-15. Mechanical process of spin coating—clean device secured to the spin chuck by vacuum (a), solution deposited on device (b), and spin speed ramped up (c). Image (a) shows the parameters for solving Equation 2-13, where ϕ is the reference axis of rotation.

To quantify the centrifugal force (F_c), we begin with Newton's second law of an inertial frame described by

$$\vec{F} = m \frac{\partial^2 \vec{r}}{\partial t^2} \quad (2-9)$$

Where F is the force, m is the mass and the differential, d^2r/dt^2 , is the acceleration.

However, we want the force of the rotating frame, where the time derivative of the acceleration is defined by

$$\frac{d\vec{a}}{dt} = \vec{\omega} \times \vec{a} + \frac{\partial \vec{a}}{\partial t} \quad (2-10)$$

Where ω is the angular velocity:

$$\vec{\omega} = \frac{d\vec{\Omega}}{dt} \quad (2-11)$$

Now, transforming d^2r/dt^2 in Equation 2-9 using Equation 2-10, we arrive at a new equation of motion:

$$\vec{F} = -2m\vec{\omega} \times \frac{\partial \vec{r}}{\partial t} - m\vec{\omega} \times (\vec{\omega} \times \vec{r}) \quad (2-12)$$

Here, the first term is known as the Coriolis force, which contains the term dr/dt and is thus dependent on the velocity of the rotating frame. Extracting the second term, we arrive at the centrifugal force:

$$\vec{F}_c = -m\vec{\omega} \times (\vec{\omega} \times \vec{r}) \quad (2-13)$$

Equation 2-13 is a rough approximation of what is actually occurring during the spin coating process. To proceed further we would require tedious calculations involving fluid mechanics, which was not investigated in this work. Should the reader be interested in such studies, he or she may consult the literature.^{99,100} Since morphology is position-dependent, all AFM images were obtained from similar areas on the device—within 2 mm of a pixel where the active area overlaps the underlying ITO. Typically 3-5 AFM images were taken per device to ensure uniform morphology and accurate representation.

2.5.1.3 Thickness Measurements

To gauge thickness of active layer films, AFM tapping mode was used to measure “stepheights.” A razor blade was used to lightly scratch the device surface, lifting a portion of the organic layer and leaving behind the PEDOT:PSS film intact. Using the optical microscope on the AFM, the scratch was found by adjusting the x-y parameters of the AFM stage. To measure stepheights, images were taken with the scratch and the film in the scanning range. Typically, $15 \mu\text{m} \times 15 \mu\text{m}$ images were taken. If a larger surface roughness was apparent, a larger image was taken to obtain a more accurate

stepheight. SpmLabAnalysis software was used to take an average of the film height and the scratch height (Figure 2-16). Taking the difference of these two average heights resulted in the film thickness. Typically 3-5 stepheight images were taken per device, and the average of these was accepted as an accurate representation of the active layer thickness.

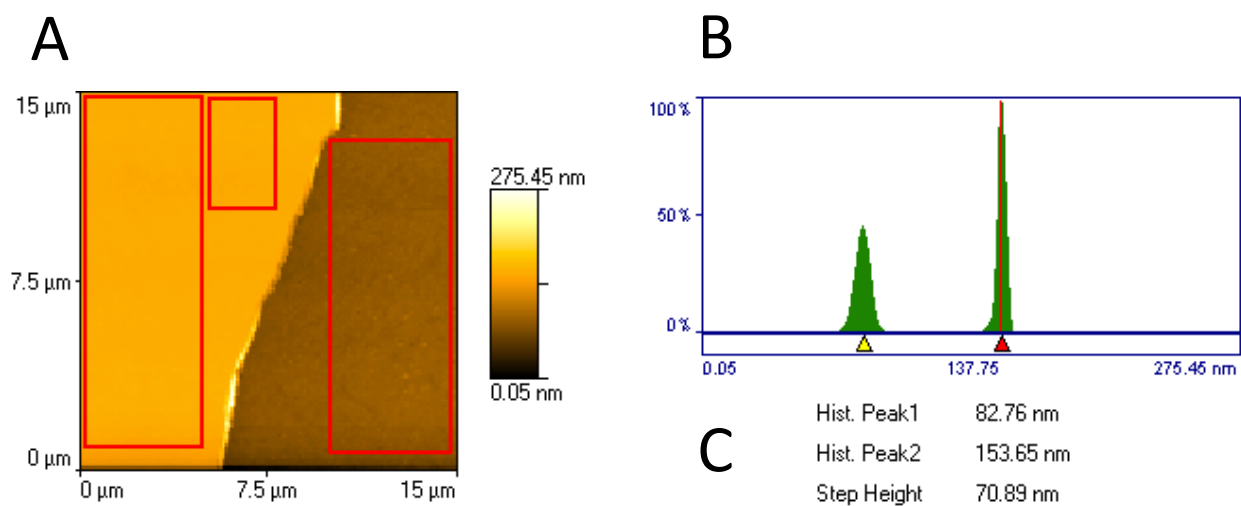


Figure 2-16. Use of SpmLabAnalysis software to calculate the stepheight for an AFM image containing a scratch (left) and the film (right) (a), height distribution (b), and stepheight calculation (c).

2.5.2 Transmission Electron Microscopy

To gain a better understanding of morphology, AFM should not be the only technique used. Techniques involving electron microscopy provide a more in-depth analysis of film structure in OPVs. Transmission Electron Microscopy (TEM) basically shoots electrons at a sample and the interaction of the electrons with the sample is then projected on a film (Figure 2-17). Since the organic layers used in this work were approximately 70 nm, the thickness is sufficient to pass electrons.

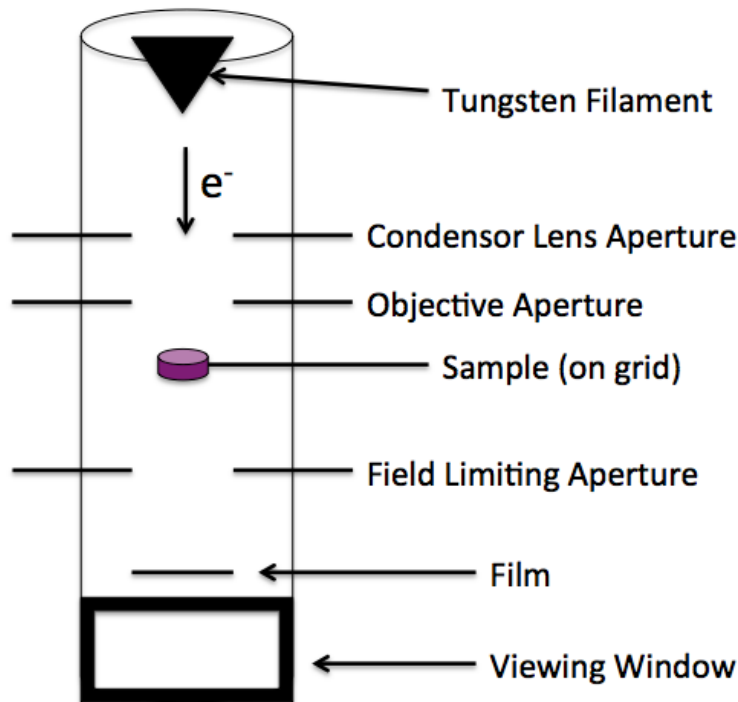


Figure 2-17. Schematic of a TEM.

2.5.2.1 Sample Preparation

To obtain top-down TEM images, samples of organic films were prepared on carbon or lacey carbon coated copper grids (Electron Microscopy Sciences cat. # CF150-Cu and CL-200-Cu, respectively). To ensure accurate representation of morphology and performance, the same device of which OPV parameters and AFM images were reported was used for TEM. A glass scribe was used to cut a square (2 mm × 2 mm) out of the device ~1 mm away from the pixel where the active layer overlapped the underlying ITO (Figure 2-18). A razor blade was used to scratch grids on the surface of the square. The square was then floated atop 18.2 MΩ water. Since PEDOT:PSS is an aqueous solution, the water dissolved this layer and the glass sunk to the bottom of the dish leaving the thin organic film floating on top of the water. Dumont N7 tweezers (Electron Microscopy Science cat. # 72864-D) were used to pick

up the TEM grid. The grid was then slowly lowered to the surface of the water to lightly touch the floating organic film. The film adhered to the grid and excess water was removed from the grid by lightly touching the edge with a KimWipe.

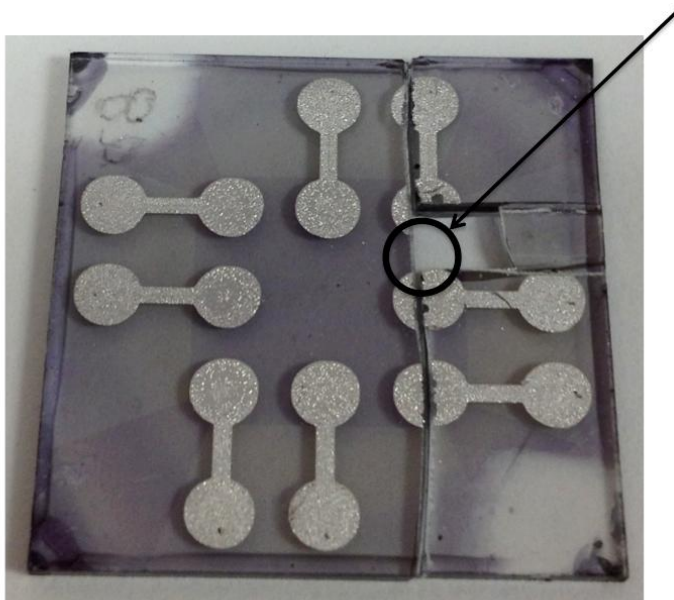


Figure 2-18. Area of a device from which a TEM sample was prepared.

2.5.2.2 Top-down Imaging

TEM images were obtained using a JEOL 200CX TEM at the Major Analytical Instrumentation Center (MAIC) of the Department of Materials Science and Engineering at the University of Florida with the assistance of Dr. Michael Kesler. A driving voltage of 200 kV was used with a spot size of 1 or 2. A small objective aperture (4) was inserted, which blocked a portion of the electrons, reducing the beam intensity. Images were obtained under-focus at a magnification of 100 or 200 kX zoom, unless otherwise noted.

CHAPTER 3
ASYMMETRIC AND SYMMETRIC OLIGOMERS AS TAILOR-MADE ADDITIVES IN
ORGANIC PHOTOVOLTAICS

3.1 Introduction

In order for organic photovoltaics to compete with their inorganic counterparts in the consumer market, power conversion efficiencies (PCEs) must be increased. As discussed in chapter 1, many different aspects of device physics, design, and processing techniques contribute to the film morphology, and thus PCE. Recent techniques include additives,^{101–103} solvent annealing,¹⁰⁴ use of block copolymers,^{105–108} thermal annealing,^{27,109} and slow film drying.¹¹⁰ Such techniques typically have unfavorable mixing thermodynamics, resulting in decreased PCEs, however. Chen *et al.* proposed that P3HT crystallization at the P3HT/PCBM interface in a bulk heterojunction significantly influences film morphology.¹¹¹ Thus, if crystallinity can be controlled, a fundamental understanding of morphological effects on device performance can be achieved. A method to control crystallinity is the use of a “tailor-made additive” to control nucleation and kinetics of crystal growth.^{112–114} Such an additive has the same basic structure as the parent molecule (Figure 3-1a), with the exception of a minor defect (Figure 3-1b).

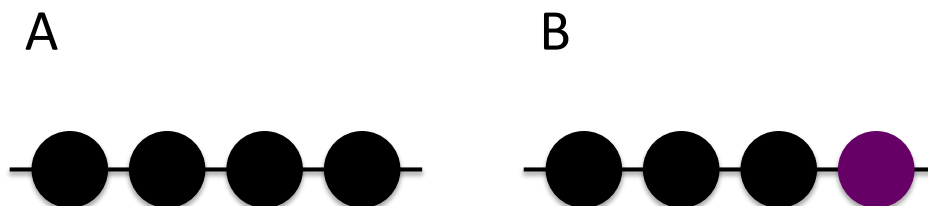


Figure 3-1. Cartoon example of a parent molecule (a) and the resulting “tailor-made additive” (b).

This chapter will discuss the use of tailor-made additives to obtain more favorable morphologies, resulting in increased PCEs of molecular bulk heterojunction organic photovoltaics.

3.2 Isoindigo as an Electron Donor

Isoindigo (Figure 3-2a), a structural isomer of indigo, is a pigment that has been used in dyes since the early 1900s.¹¹⁵ In 2010, our group synthesized the first electroactive isoindigo-based oligomer, il(TT)₂ (Figure 3-2b), as an electron donor for molecular bulk heterojunction organic photovoltaics.¹¹⁶ Initial experiments of il(TT)₂:PC₆₁BM containing solar cells afforded promising power conversion efficiencies up to 1.76%. Isoindigo's popularity in the field of organic electronics quickly grew thereafter. Within two years of initial publication, other groups synthesized and applied isoindigo-based molecules to a variety of electronics—organic field-effect transistors;⁷ thin-film transistors;¹¹ semiconductor memory devices;²¹ and small molecule,^{89,116} and polymer solar cells.^{117–125} Currently, power conversion efficiencies of solar cells containing isoindigo-based materials have reached 6.3%.¹²³ For all solar cells prepared in this chapter, the parent oligomer used was il(TT)₂ (Figure 3-2b).

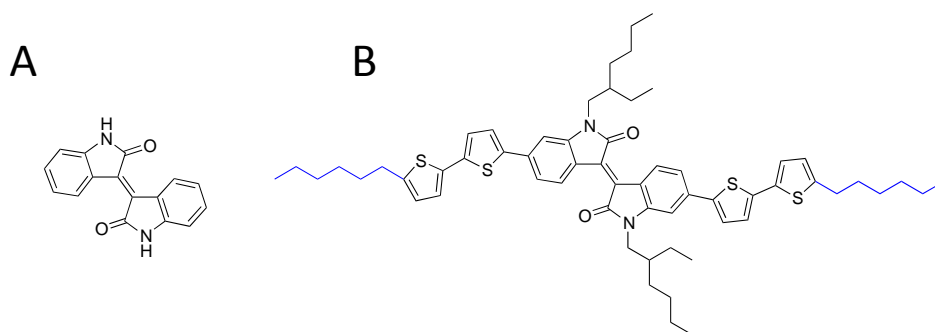


Figure 3-2. Chemical structures of *trans*-isoindigo (a) and il(TT)₂, the parent oligomer used in the experiments presented in this work (b).

3.3 il(TT)₂-*t*Bu₃Si

To probe the effects of a tailor-made additive on the morphology of a bulk-heterojunction cell, an asymmetric oligomer was synthesized. The resulting oligomer, il(TT)₂-*t*Bu₃Si (Figure 3-3), is structurally similar to its parent molecule, il(TT)₂ (Figure 3-2b). Whereas il(TT)₂ is symmetrical with linear hexyl chains as end groups, il(TT)₂-*t*Bu₃Si is asymmetrical with a linear hexyl chain as one end group and a bulky triisobutylsilyl (*t*Bu₃Si) group as the other end group. The idea here is that the bulky size of the triisobutylsilyl group would disrupt crystal growth when incorporated in the il(TT)₂:fullerene heterojunction. Since il(TT)₂-*t*Bu₃Si still contains one similar end group as the parent molecule, crystal growth should not be inhibited, but rather slowed down. As mentioned in chapter 1, with typical exciton diffusion lengths ca. 5 – 15 nm, an ideal morphology may be able to be tuned with an optimized concentration of the tailor-made additive.

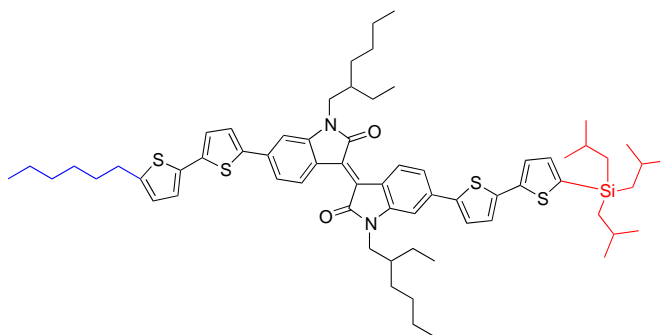


Figure 3-3. Chemical structure of the asymmetric tailor made additive, il(TT)₂-*t*Bu₃Si.

3.3.1 Photovoltaic Performance

Organic photovoltaic devices were prepared by the same fashion described in chapter 2. Active layers of [il(TT)₂:il(TT)₂-*t*Bu₃Si]:PC₆₁BM were prepared, where the concentration of [donor]:acceptor was kept at [1]:1 by weight. To probe the effects of the triisobutylsilyl containing tailor-made additive, the concentration of [il(TT)₂:il(TT)₂-

$i\text{Bu}_3\text{Si}$] was varied with increasing mole percent $i\text{l}(\text{TT})_2-i\text{Bu}_3\text{Si}$. For example, when “20 mole % $i\text{l}(\text{TT})_2-i\text{Bu}_3\text{Si}$ ” is mentioned, the OPV cell has an active layer of [40% $i\text{l}(\text{TT})_2$:10% $i\text{l}(\text{TT})_2-i\text{Bu}_3\text{Si}$]:50% PC_{61}BM , hence [1]:1 by weight.

Solar cell device performance data for increasing mole % $i\text{l}(\text{TT})_2-i\text{Bu}_3\text{Si}$ is shown in Table 3-1. Immediately there is a noticeable increase in PCE from 1.30 to 2.24 % with the addition of 20 mole % $i\text{l}(\text{TT})_2-i\text{Bu}_3\text{Si}$. This almost double increase in PCE can be attributed to the increases in V_{OC} , J_{SC} and FF: 0.72 to 0.82 V, 4.58 to 6.14 mA cm^{-2} , and 0.39 to 0.45, respectively. With the addition of asymmetric oligomer after 20 mole % $i\text{l}(\text{TT})_2-i\text{Bu}_3\text{Si}$, there is a gradual decrease in V_{OC} , J_{SC} , FF, and consequently PCE. Such a decrease can be attributed to the formation of a more amorphous film as the bulky triisobutylsilyl group is disrupting the $i\text{l}(\text{TT})_2:\text{PC}_{61}\text{BM}$ interface crystallization. Figure 3-4 shows representative J-V curves of 0 through 100 mole % $i\text{l}(\text{TT})_2-i\text{Bu}_3\text{Si}$. The shapes of the J-V curves help obtain a visual of the performance, and show a significant difference between a $i\text{l}(\text{TT})_2:\text{PC}_{61}\text{BM}$ (0 % $i\text{l}(\text{TT})_2-i\text{Bu}_3\text{Si}$) and a $i\text{l}(\text{TT})_2-i\text{Bu}_3\text{Si}:\text{PC}_{61}\text{BM}$ (100 % $i\text{l}(\text{TT})_2-i\text{Bu}_3\text{Si}$) solar cell.

Table 3-1. Summary of OPV parameters for increasing mole % asymmetric oligomer in [$i\text{l}(\text{TT})_2:i\text{l}(\text{TT})_2-i\text{Bu}_3\text{Si}$]: PC_{61}BM solar cells under AM1.5G 100 mW cm^{-2} simulated radiation.

mole %	V_{OC} (V)	J_{SC} (mA cm^{-2})	FF	PCE (%)
0	0.72	4.58	0.39	1.30
10	0.75	5.79	0.39	1.69
20	0.82	6.14	0.45	2.24
30	0.81	5.28	0.49	2.09
40	0.75	4.54	0.49	1.65
50	0.69	2.55	0.40	0.71
100	0.77	1.17	0.24	0.22

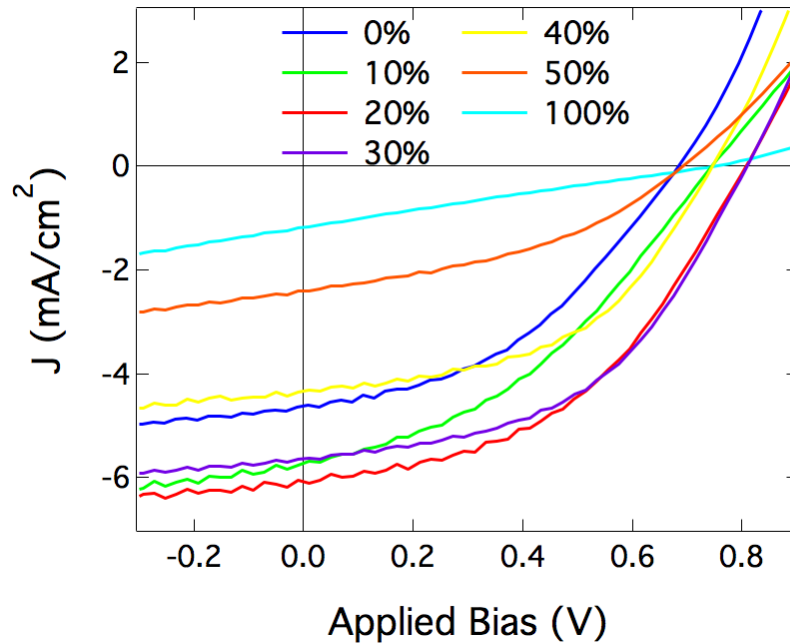


Figure 3-4. Representative J-V curves of 0 to 100 % asymmetric oligomer in [il(TT)₂:il(TT)₂-tBu₃Si]:PC₆₁BM solar cells under AM1.5G 100 mW cm⁻² simulated radiation.

3.3.2 Charge Mobility

To probe the effects of the triisobutylsilyl containing tailor-made additive on charge carrier mobilities, space-charge limited current (SCLC) devices were prepared. Devices were prepared by the same fashion described in chapter 2, with a device architecture of glass/MoO₃/[il(TT)₂:il(TT)₂-tBu₃Si]:PC₆₁BM/gold, with increasing mole percent of asymmetric oligomer as with OPVs. Calculated hole mobilities using the SCLC equation (Equation 1-14) of measured dark current (see chapter 2) are summarized in Figure 3-5. With increasing mole % of il(TT)₂-tBu₃Si, the hole mobility gradually decreases. From 0 to 20 mole % there is a decrease from 1.6×10^{-5} to 1.0×10^{-5} cm² V⁻¹ s⁻¹. The hole mobility of a device without il(TT)₂ (100 mole % il(TT)₂-tBu₃Si) dropped by three orders of magnitude to 2.3×10^{-8} cm² V⁻¹ s⁻¹. Figure 3-6 provides representative J-V curves of 0, 10, 20 (3-6a), 30, 40 (3-6b), 50 and 100 % (3-6c) il(TT)₂-

$t\text{Bu}_3\text{Si}$ fitted with the SCLC equation. Such a continual and drastic decrease in hole mobility with the addition of $\text{il}(\text{TT})_2\text{-}t\text{Bu}_3\text{Si}$ can be attributed to the bulkiness of the triisobutylsilyl group. As there is an increasing amount of $t\text{Bu}_3\text{Si}$, and thus less linear hexyl chains, the crystallographic packing is less ordered, leading to a more amorphous film. The bulkiness of the triisobutylsilyl group increases the intermolecular hopping distance, and consequently decreases the charge-carrier mobility. This will be further realized when considering the morphology data presented in section 3.3.3.

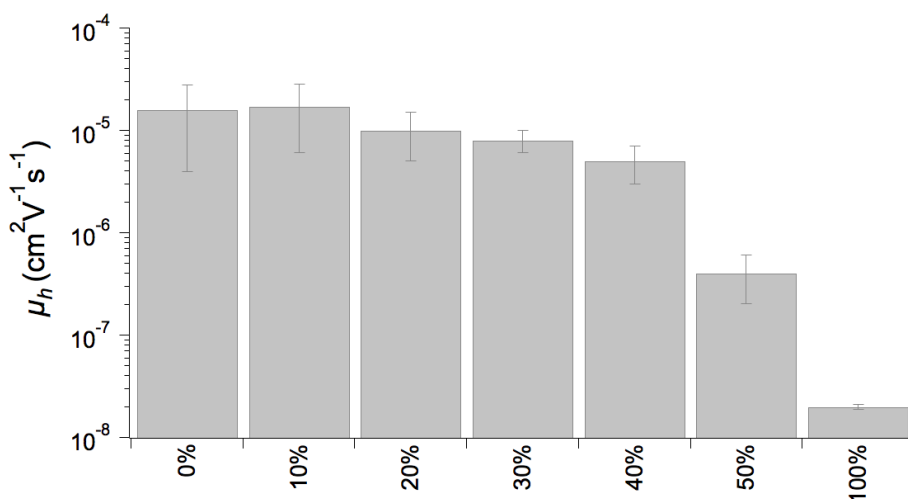


Figure 3-5. Summary of hole mobilities for increasing mole % asymmetric oligomer in $[\text{il}(\text{TT})_2:\text{il}(\text{TT})_2\text{-}t\text{Bu}_3\text{Si}]:\text{PC}_{61}\text{BM}$ SCLC devices. Values reported are averages of 6-8 pixels, with error bars showing +/- one standard deviation.

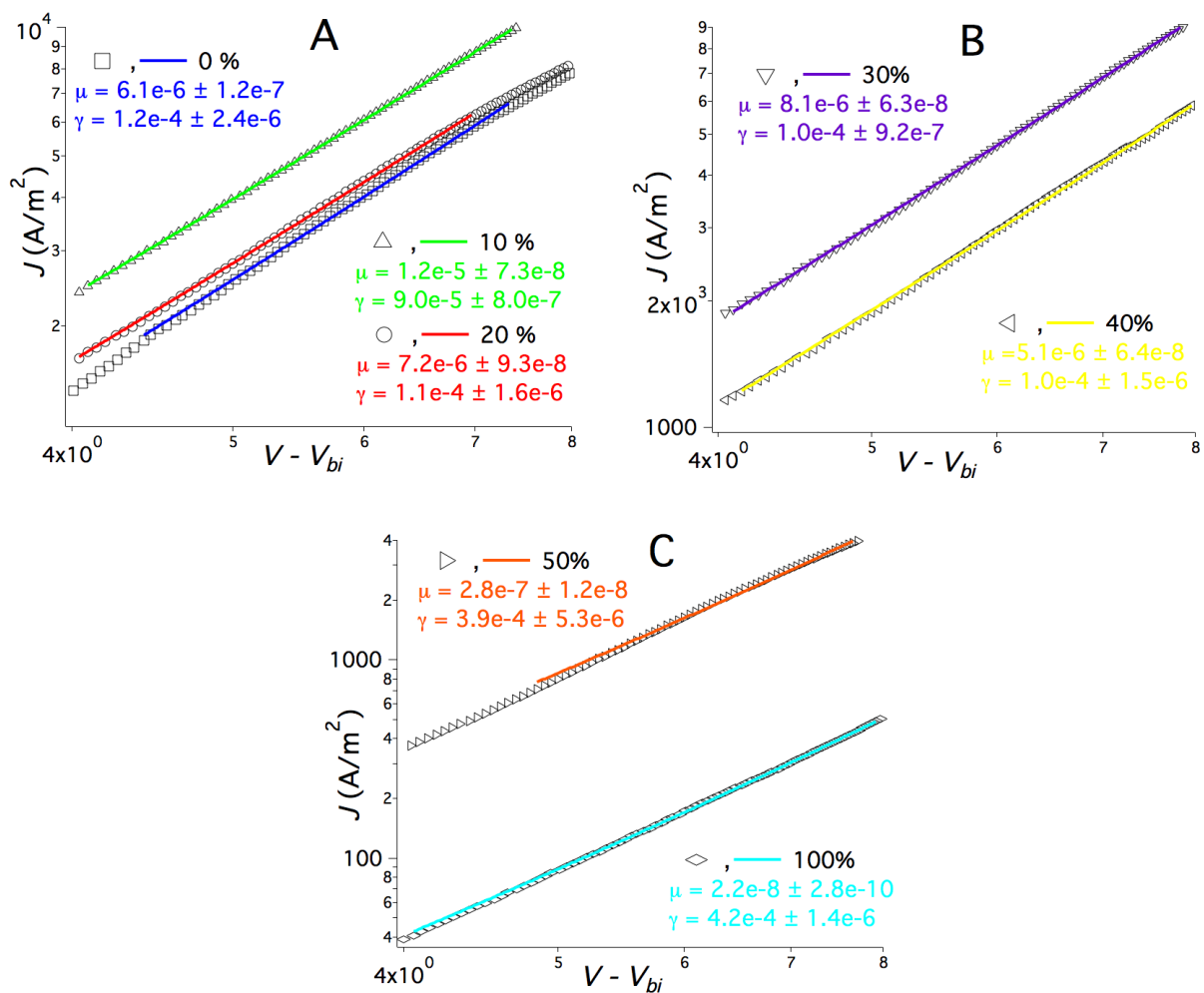


Figure 3-6. Representative J-V plots of 0, 10, 20 (a), 30, 40 (b), 50 and 100 (c) mole % asymmetric oligomer in [il(TT)₂:il(TT)₂-iBu₃Si]:PC₆₁BM SCLC devices. Data presented are from one pixel and the hole mobility (μ) and field-dependent term (γ) are from the SCLC fit for that pixel, which was used in the calculation of the averages in Figure 3-5.

3.3.3 Morphology

As described in sections 3.3.1 and 3.3.2, many performance parameters were a result of morphological changes with the addition of il(TT)₂-iBu₃Si. To probe the morphology of a solid-state device, atomic force microscopy (AFM) and bright field transmission electron microscopy (TEM) were used. Films for AFM characterization were prepared in the same manner as the photovoltaic cells with [il(TT)₂:il(TT)₂-iBu₃Si]:PC₆₁BM at [1]:1 by weight with increasing mole % il(TT)₂-iBu₃Si. AFM images of

these films are presented in Figures 3-7 and 3-8. Immediately it can be seen that the domain sizes gradually decrease upon initial addition of 10 mole % $\text{il}(\text{TT})_2\text{-}i\text{Bu}_3\text{Si}$. Upon addition of 20 mole % $\text{il}(\text{TT})_2\text{-}i\text{Bu}_3\text{Si}$, domain sizes are quite small, allowing for better exciton diffusion and thus increased PCE. In addition to a decreasing domain size, devices with 0 to 30 mole % $\text{il}(\text{TT})_2\text{-}i\text{Bu}_3\text{Si}$ have well defined domains, indicating high crystallinity. When additional $\text{il}(\text{TT})_2\text{-}i\text{Bu}_3\text{Si}$ is added after 30 mole %, the features become distorted and their shapes are less discernable. This distortion may be attributed to the formation of a more amorphous film, which confirms the suspicion that $\text{il}(\text{TT})_2\text{-}i\text{Bu}_3\text{Si}$ disrupts $\text{il}(\text{TT})_2$ crystal growth in the bulk heterojunction. This is confirmed when examining the 100 mole % image, as the surface appears extremely smooth and flat. Using Nanoscope 7.30 software, a surface roughness value of 0.374 nm was calculated for the 100 mole % image, indicating virtually no features, and thus a completely amorphous film. In Figure 3-8, the $1 \times 1 \mu\text{m}$ images further confirm the decrease in domain size and crystallinity, expressed by the formation of a more amorphous film as mole % $\text{il}(\text{TT})_2\text{-}i\text{Bu}_3\text{Si}$ increases.

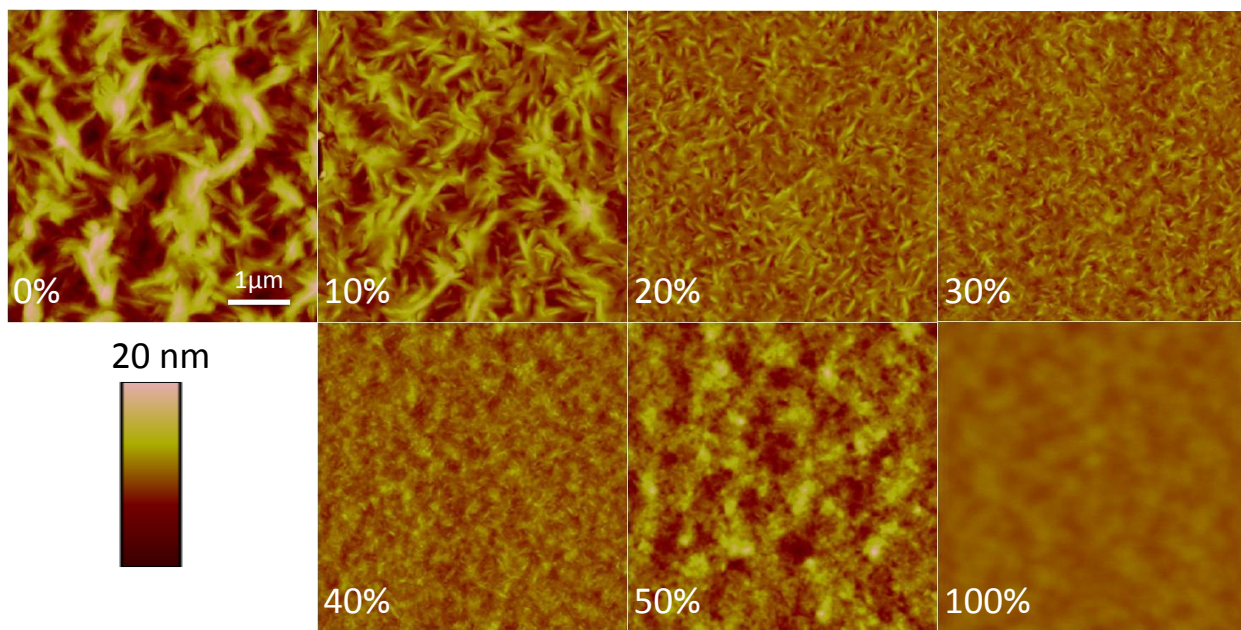


Figure 3-7. AFM images of increasing mole % asymmetric oligomer in [il(TT)₂:il(TT)₂-tBu₃Si]:PC₆₁BM devices. All images shown are 5 × 5 μm, and have the same scale (1 μm) and height bar (20 nm).

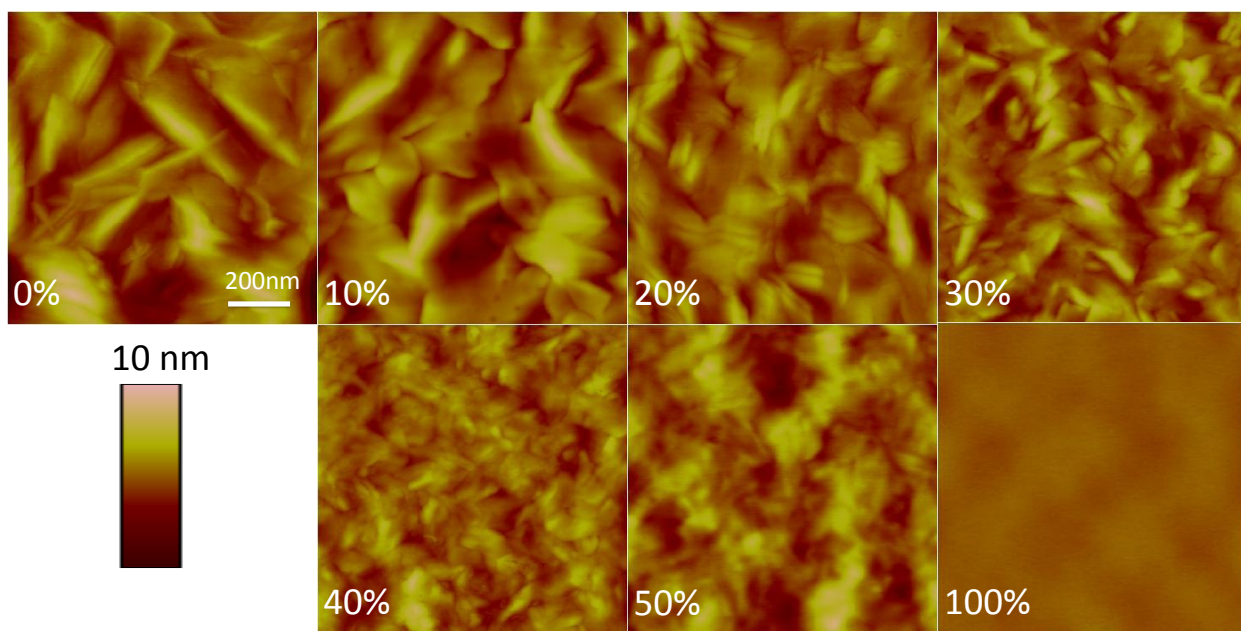


Figure 3-8. AFM images of increasing mole % asymmetric oligomer in [il(TT)₂:il(TT)₂-tBu₃Si]:PC₆₁BM devices. All images shown are 1 × 1 μm, and have the same scale (200 nm) and height bar (10 nm).

As mentioned in chapter 2, the results of one method of morphology characterization should not be immediately accepted as what is truly going on in the

solid-state device. In addition to AFM, top down TEM images were taken to further investigate the morphological changes with addition of $\text{il}(\text{TT})_2\text{-}i\text{Bu}_3\text{Si}$ (Figure 3-9). TEM samples were prepared using the procedure described in chapter 2, and the same film from which AFM images were represented. As with AFM, TEM shows a decrease in domain size with increasing mole % $\text{il}(\text{TT})_2\text{-}i\text{Bu}_3\text{Si}$. Also, the domains become distorted and less discernable upon addition of 40 mole % $\text{il}(\text{TT})_2\text{-}i\text{Bu}_3\text{Si}$.

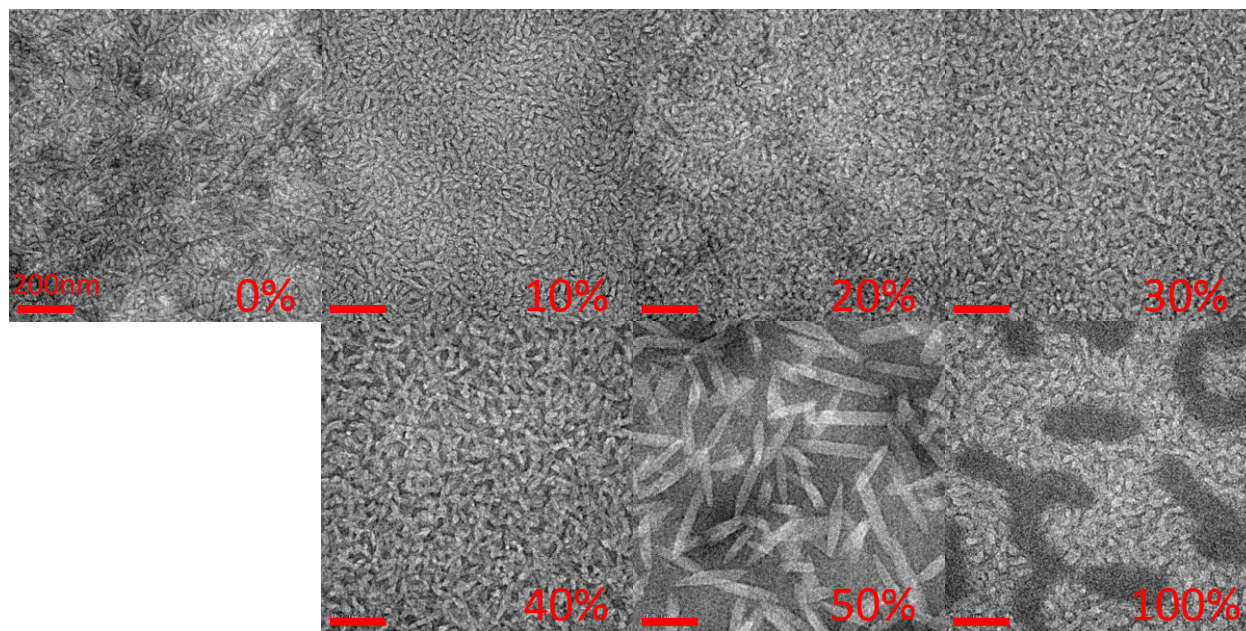


Figure 3-9. TEM images of increasing mole % asymmetric oligomer in $[\text{il}(\text{TT})_2\text{:il}(\text{TT})_2\text{-}i\text{Bu}_3\text{Si}]\text{:PC}_{61}\text{BM}$ devices. All images have the same 200 nm scale bar.

Despite the apparent decrease in domain sizes from 0 to 40 mole % $\text{il}(\text{TT})_2\text{-}i\text{Bu}_3\text{Si}$, the 50 and 100 mole % images are the most striking. Unlike AFM, which showed very flat films for the 50 and 100 mole % devices (Figures 3-7 and 3-8), TEM reveals features. Here there are two different distinct phases, a light and a dark phase. Cross-sectional TEM samples were prepared using a focused ion beam (FIB) for the 20 and 100 mole % $\text{il}(\text{TT})_2\text{-}i\text{Bu}_3\text{Si}$ devices (Figure 3-10). The full procedure of sample preparation using the FIB can be viewed in Ken Graham's Ph.D. dissertation.⁹⁵

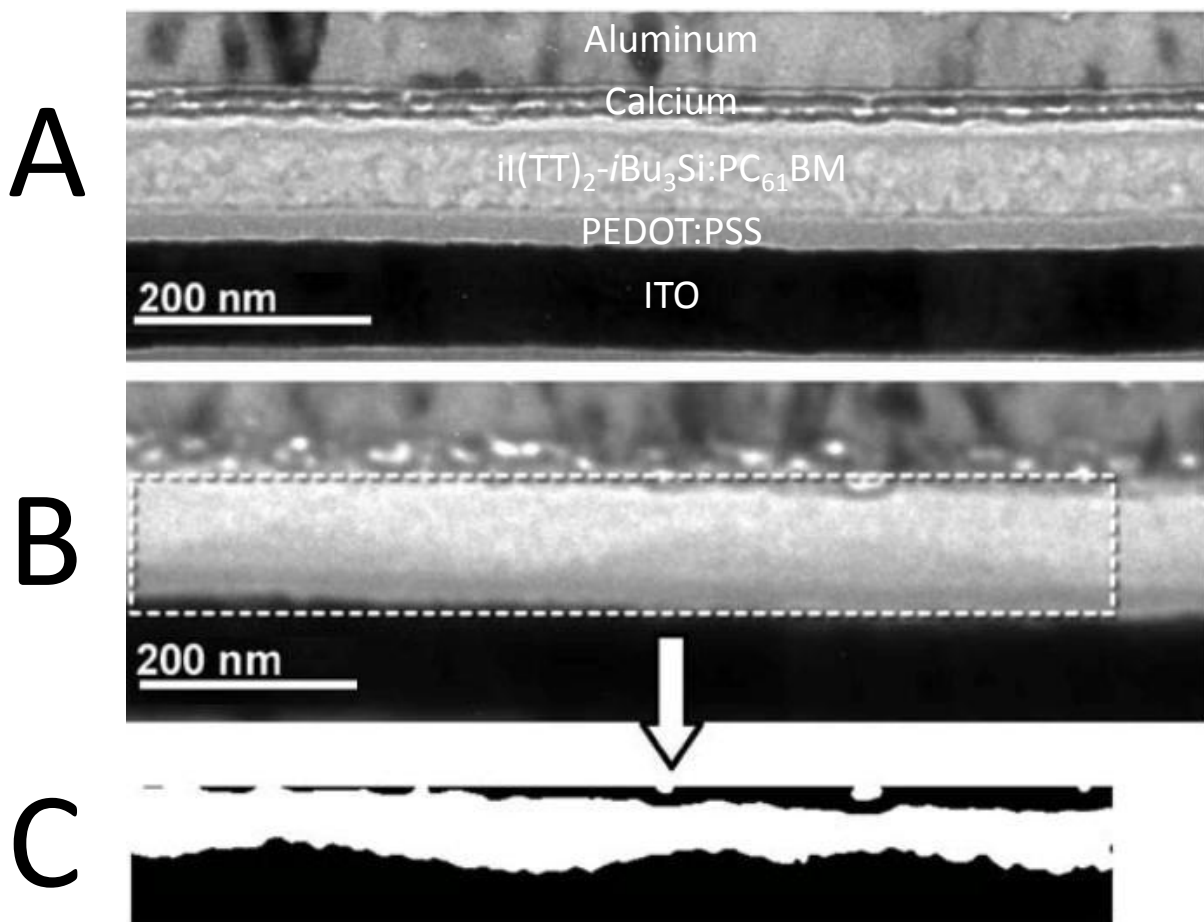


Figure 3-10. Cross-sectional TEM images of 20 (a) and 100 (b) mole % asymmetric oligomer in $[\text{il}(\text{TT})_2:\text{il}(\text{TT})_2\text{-}/\text{Bu}_3\text{Si}]:\text{PC}_{61}\text{BM}$ devices as well as a 3 nm Gaussian blur (c) applied to image b. Adapted with permission from Ref 95.

In our group's previous publication, we took cross-sectional TEM images prepared using a FIB, and performed x-ray photoelectron spectroscopy (XPS) experiments to determine the light phase is PC_{61}BM and the dark phase is the isoindigo oligomer.⁸⁹ Thus, the white phase crystals in the 100 mole % TEM image are those of PC_{61}BM . The cross-sectional image of the 100 mole % device suggests that the PC_{61}BM rich crystals are concentrated near the PEDOT:PSS interface (Figure 3-10b,c). This explains why the features were not visible with AFM, as AFM takes a surface topology image, rather than the bulk of the film (see chapter 2).

It should be stressed, and evident after viewing AFM and TEM images presented in this subsection, that a single morphology technique should not be taken for granted. Performing at least two techniques is a necessity to obtain a full understanding of the fundamental nanostructure in a solid-state device.

3.3.4 Crystal Growth

To further assess the crystallization occurring in the bulk heterojunction with the addition of $\text{il}(\text{TT})_2\text{-}i\text{Bu}_3\text{Si}$, crystal growth experiments were carried out by Danielle Salazar. A complete and detailed procedure of the experiments can be viewed in Ken Graham's Ph.D. dissertation.⁹⁵ An optical microscope was used to view crystals under crossed polars at different mole % $\text{il}(\text{TT})_2\text{-}i\text{Bu}_3\text{Si}$, as a function of $\text{il}(\text{TT})_2$ (Figure 3-11). Crystal size decreased from 172 to 46 μm with 0 to 10 mole % $\text{il}(\text{TT})_2\text{-}i\text{Bu}_3\text{Si}$, respectively. When 20 mole % $\text{il}(\text{TT})_2\text{-}i\text{Bu}_3\text{Si}$ was added, no crystals were observed. With only $\text{il}(\text{TT})_2\text{-}i\text{Bu}_3\text{Si}$ and no $\text{il}(\text{TT})_2$, the polarized microscope shows very small crystals, indicating $\text{il}(\text{TT})_2\text{-}i\text{Bu}_3\text{Si}$'s ability to crystallize on its own. These crystallization experiments further confirm that a tailor-made additive, in this case $\text{il}(\text{TT})_2\text{-}i\text{Bu}_3\text{Si}$, can indeed slow down nucleation and crystallization growth kinetics, in the $\text{il}(\text{TT})_2\text{:PC}_{61}\text{BM}$ bulk heterojunction. Thus, with increasing mole % of the additive, morphology can be finely tuned to achieve desired PCEs.

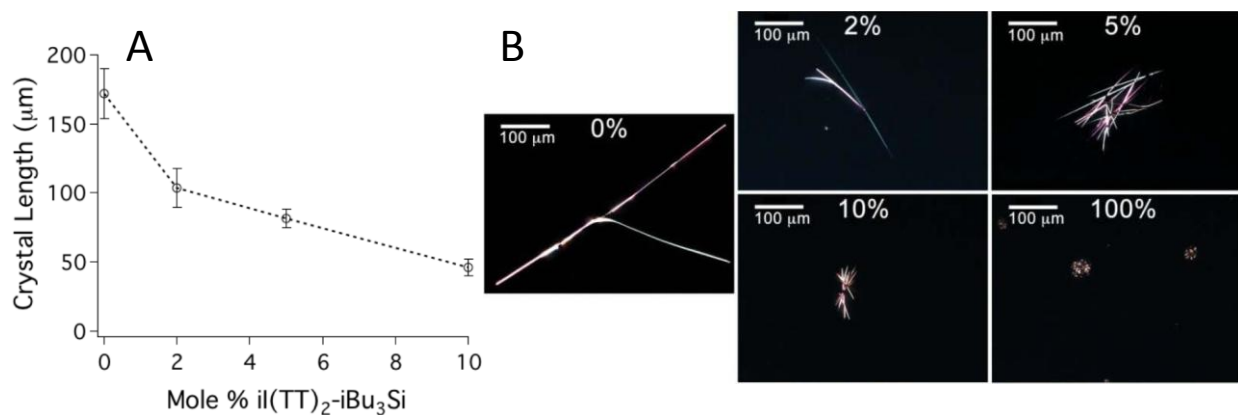


Figure 3-11. Crystal length dependence on mole % $\text{il(TT)}_2\text{-}i\text{Bu}_3\text{Si}$ as a function of il(TT)_2 (a) and representative polarized microscope images of increasing mole % $\text{il(TT)}_2\text{-}i\text{Bu}_3\text{Si}$ in $\text{il(TT)}_2\text{:il(TT)}_2\text{-}i\text{Bu}_3\text{Si}$. Crystal lengths are averages of 32 to 72 crystals and the error bars show \pm one standard deviation. Adapted with permission from Ref 95.

3.4 $\text{il(TT-}i\text{Bu}_3\text{Si)}_2$

Section 3.3 demonstrated the use of a tailor-made additive to finely tune morphology in molecular bulk heterojunction organic photovoltaics. The oligomer used, $\text{il(TT)}_2\text{-}i\text{Bu}_3\text{Si}$, was an asymmetric derivative of the parent molecule il(TT)_2 . To further probe if the asymmetry alone of $\text{il(TT)}_2\text{-}i\text{Bu}_3\text{Si}$ led to morphology control, an analogous symmetrical derivative was synthesized, $\text{il(TT-}i\text{Bu}_3\text{Si)}_2$ (Figure 3-12). A detailed synthesis and characterization procedure may be viewed in Romain Stalder's Ph.D. dissertation.⁸⁶ In this symmetric derivative, both linear hexyl chains in the parent molecule, il(TT)_2 , were replaced with bulky triisobutylsilyl groups.

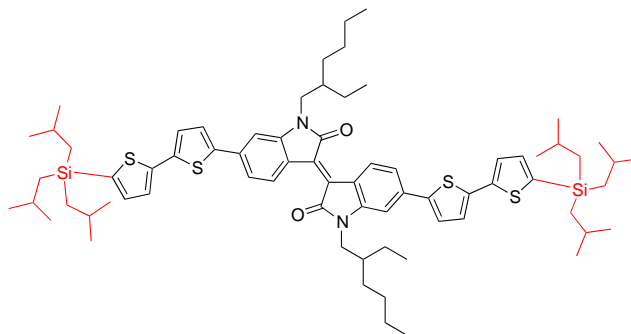


Figure 3-12. Chemical structure of the symmetric tailor made additive, $\text{il}(\text{TT}-\text{ᵐ}\text{Bu}_3\text{Si})_2$.

3.4.1 Photovoltaic Performance

Organic photovoltaics were prepared in the same manner as those with the asymmetric oligomer, $\text{il}(\text{TT})_2-\text{ᵐ}\text{Bu}_3\text{Si}$. Devices had active layers of $[\text{il}(\text{TT})_2:\text{il}(\text{TT}-\text{ᵐ}\text{Bu}_3\text{Si})_2]:\text{PC}_{61}\text{BM}$, and varied with increasing mole % $\text{il}(\text{TT}-\text{ᵐ}\text{Bu}_3\text{Si})_2$, while maintaining a [1]:1 by weight ratio. A summary of OPV parameters from devices containing the symmetrical triisobutylsilyl additive are summarized in Table 3-2, with representative J-V curves of 0 through 100 mole % $\text{il}(\text{TT}-\text{ᵐ}\text{Bu}_3\text{Si})_2$ in Figure 3-13. Unlike devices containing the asymmetrical additive, $\text{il}(\text{TT})_2-\text{ᵐ}\text{Bu}_3\text{Si}$, there is no apparent increase in PCE with the symmetrical additive, $\text{il}(\text{TT}-\text{ᵐ}\text{Bu}_3\text{Si})_2$. With the addition of 0 to 30 mole % $\text{il}(\text{TT}-\text{ᵐ}\text{Bu}_3\text{Si})_2$, there is a decrease in V_{OC} , J_{SC} , and consequently PCE. When more $\text{il}(\text{TT}-\text{ᵐ}\text{Bu}_3\text{Si})_2$ is added past 30 mole %, J_{SC} , FF and consequently PCE further decrease by a larger amount than at lower concentrations. Such decreases may be attributed to charge carrier mobilities and morphology, which will be discussed in sections 3.4.2 and 3.4.3, respectively.

Table 3-2. Summary of OPV parameters for increasing mole % symmetric oligomer in [il(TT)₂:il(TT-*i*Bu₃Si)₂]:PC₆₁BM solar cells under AM1.5G 100 mW cm⁻² simulated radiation.

mole %	V _{OC} (V)	J _{SC} (mA cm ⁻²)	FF	PCE (%)
0	0.72	4.58	0.39	1.30
10	0.65	4.48	0.43	1.27
20	0.66	3.71	0.43	1.07
30	0.62	1.98	0.43	0.52
40	0.76	1.53	0.36	0.42
50	0.78	1.33	0.33	0.33
100	0.72	1.31	0.28	0.28

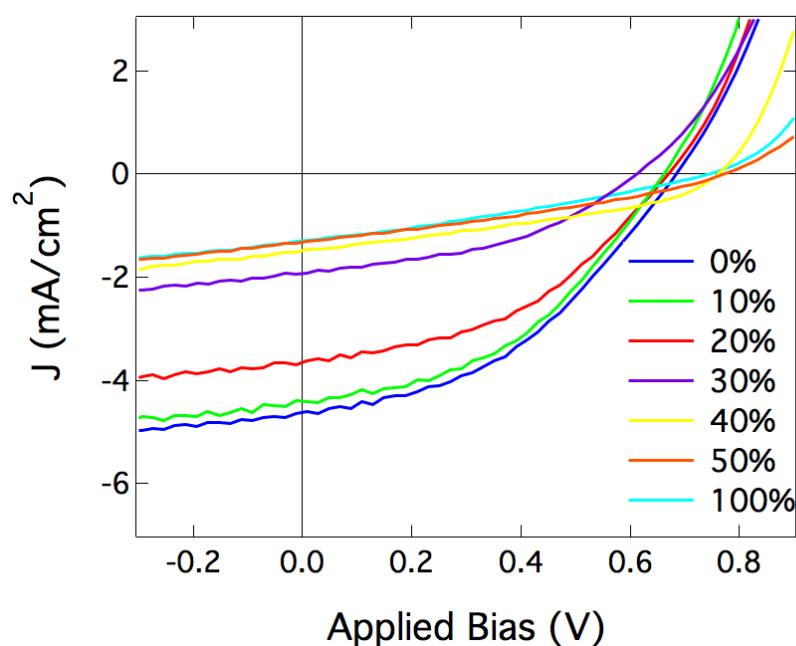


Figure 3-13. Representative J-V curves of 0 to 100 % symmetric oligomer in [il(TT)₂:il(TT-*i*Bu₃Si)₂]:PC₆₁BM solar cells under AM1.5G 100 mW cm⁻² simulated radiation.

3.4.2 Charge Mobility

To determine the effect of the symmetrical triisobutylsilyl additive on charge-carrier mobility, SCLC devices were prepared by the same manner as discussed in chapter 2. Devices received MoO₃ as the hole-injection layer and gold as the hole-collecting layer, and varied by increasing mole % il(TT-*i*Bu₃Si)₂. Hole mobility data are summarized in

Figure 3-14, with averages of 6-8 pixels, and the error bar indicating +/- one standard deviation.

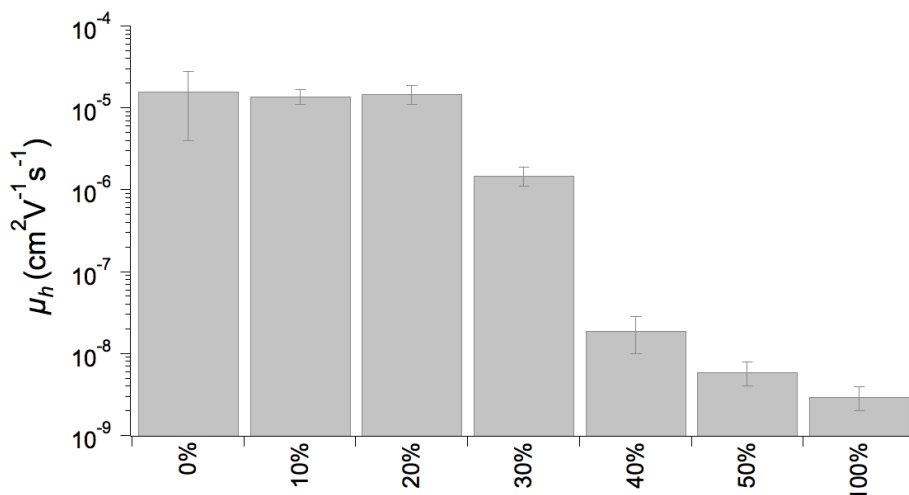


Figure 3-14. Summary of hole mobilities for increasing mole % symmetric oligomer in $[\text{il}(\text{TT})_2:\text{il}(\text{TT}-\text{iBu}_3\text{Si})_2]:\text{PC}_{61}\text{BM}$ SCLC devices. Values reported are averages of 6-8 pixels, with error bars showing +/- one standard deviation.

Similar to the asymmetric derivative, $\text{il}(\text{TT})_2-\text{iBu}_3\text{Si}$, there is negligible change in hole mobility upon addition of 10 and 20 mole % $\text{il}(\text{TT}-\text{iBu}_3\text{Si})_2$. Once more $\text{il}(\text{TT}-\text{iBu}_3\text{Si})_2$ is added past 20 mole %, there is a decrease in hole mobility, similar to the asymmetric derivative. However, the decrease in hole mobility is much sharper with the addition of $\text{il}(\text{TT}-\text{iBu}_3\text{Si})_2$ than it was for $\text{il}(\text{TT})_2-\text{iBu}_3\text{Si}$. From 20 to 40 mole % $\text{il}(\text{TT}-\text{iBu}_3\text{Si})_2$, the hole mobility decreases 3 orders of magnitude from 1.5×10^{-5} to 1.9×10^{-8} $\text{cm}^2 \text{V}^{-1} \text{s}^{-1}$. An even further order of magnitude decrease to 3×10^{-9} $\text{cm}^2 \text{V}^{-1} \text{s}^{-1}$ occurs with the pure $\text{il}(\text{TT}-\text{iBu}_3\text{Si})_2:\text{PC}_{61}\text{BM}$ device (Figure 3-15c). Such abrupt and sharp decreases in hole mobilities of the $\text{il}(\text{TT}-\text{iBu}_3\text{Si})_2$ devices can be attributed to the bulky nature of the triisobutylsilyl group. As the asymmetric oligomer (Figure 3-3) contained only one triisobutylsilyl group, the symmetric derivative contains two (Figure 3-12). Thus it is expected that the steric bulkiness of the end groups in $\text{il}(\text{TT}-\text{iBu}_3\text{Si})_2$ prevent

ordered crystallographic packing to a further extent than $\text{il}(\text{TT})_2\text{-iBu}_3\text{Si}$ did. With the presence of two bulky triisobutylsilyl groups, the intermolecular hopping distance is further increased, resulting in the observed decrease in hole carrier mobility.

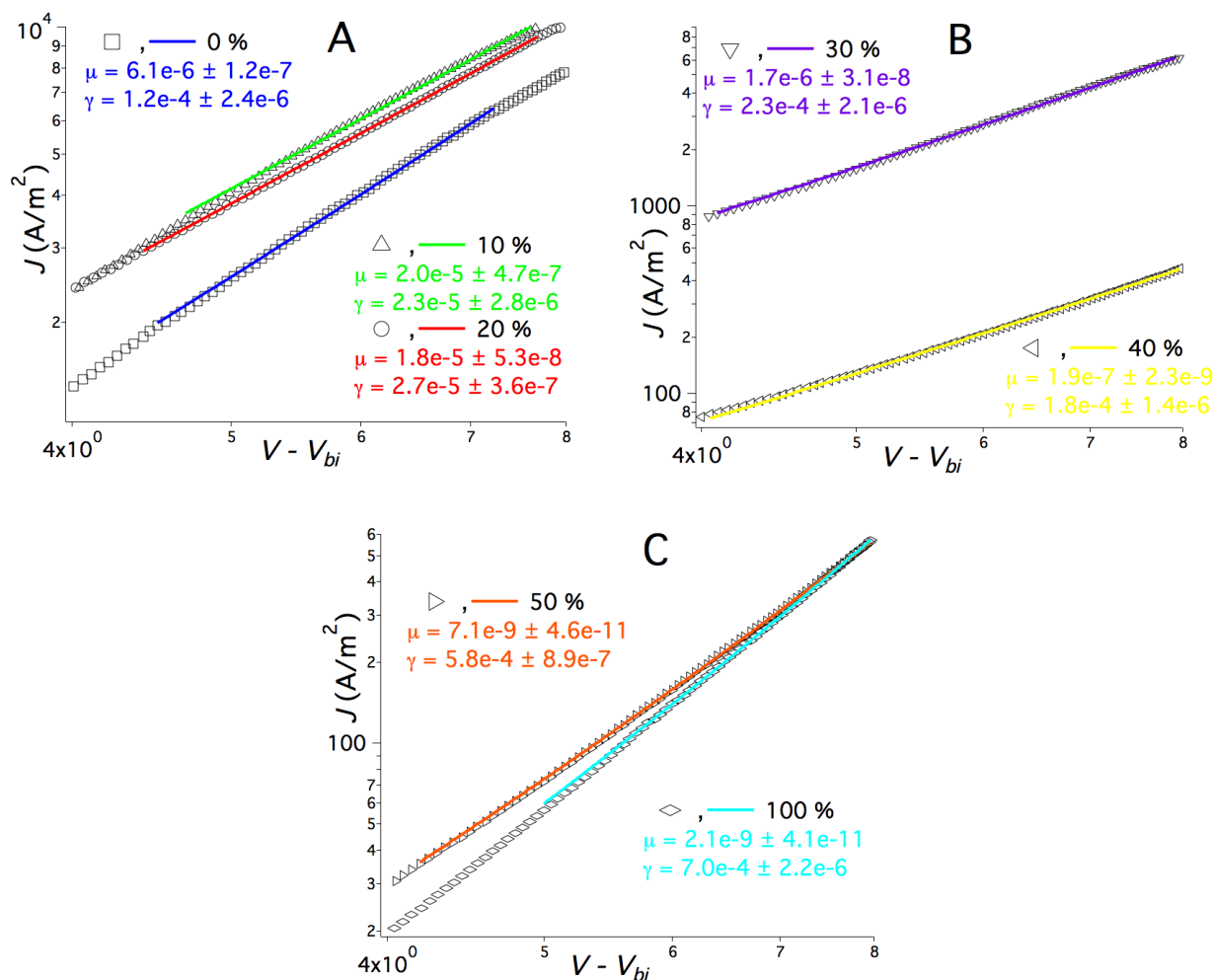


Figure 3-15. Representative J-V plots of 0, 10, 20 (a), 30, 40 (b), 50 and 100 (c) mole % symmetric oligomer in $[\text{il}(\text{TT})_2:\text{il}(\text{TT}-\text{iBu}_3\text{Si})_2]:\text{PC}_{61}\text{BM}$ SCLC devices. Data presented are from one pixel and the hole mobility (μ) and field-dependent term (γ) are from the SCLC fit for that pixel, which was used in the calculation of the averages in Figure 3-14.

3.4.3 Morphology

To obtain a fundamental understanding of the cause of the observed OPV and charge-carrier parameters, AFM and TEM images were taken to probe film morphology.

AFM samples were prepared in the same manner as for OPVs, and images are presented in Figure 3-16 and Figure 3-17 for $25 \mu\text{m}^2$ and $1 \mu\text{m}^2$ areas, respectively.

Upon initial addition of 10 and 20 mole % $\text{il}(\text{TT}-\text{iBu}_3\text{Si})_2$, the feature sizes decrease significantly; however, these features remain sharp. Similar to $\text{il}(\text{TT})_2-\text{iBu}_3\text{Si}$, these sharp features suggest crystallinity in the film. With the addition of more than 20 mole % $\text{il}(\text{TT}-\text{iBu}_3\text{Si})_2$, the features become distorted, similar to what was seen for $\text{il}(\text{TT})_2-\text{iBu}_3\text{Si}$ (Figure 3-7). This distortion can be attributed to the formation of a more amorphous morphology. Unlike $\text{il}(\text{TT})_2-\text{iBu}_3\text{Si}$, when 50 and 100 mole % $\text{il}(\text{TT}-\text{iBu}_3\text{Si})_2$ is added to the BHJ, AFM images indicate the formation of much larger crystalline domains. Upon addition of 100 mole % $\text{il}(\text{TT})_2-\text{iBu}_3\text{Si}$, the surface was virtually feature free, with a very low calculated surface roughness. Moreover, upon addition of 100 mole % $\text{il}(\text{TT}-\text{iBu}_3\text{Si})_2$, large crystal-like features on the scale of several microns are visible. With such large features present, it is apparent that the hole mobility experiences such a drastic decrease.

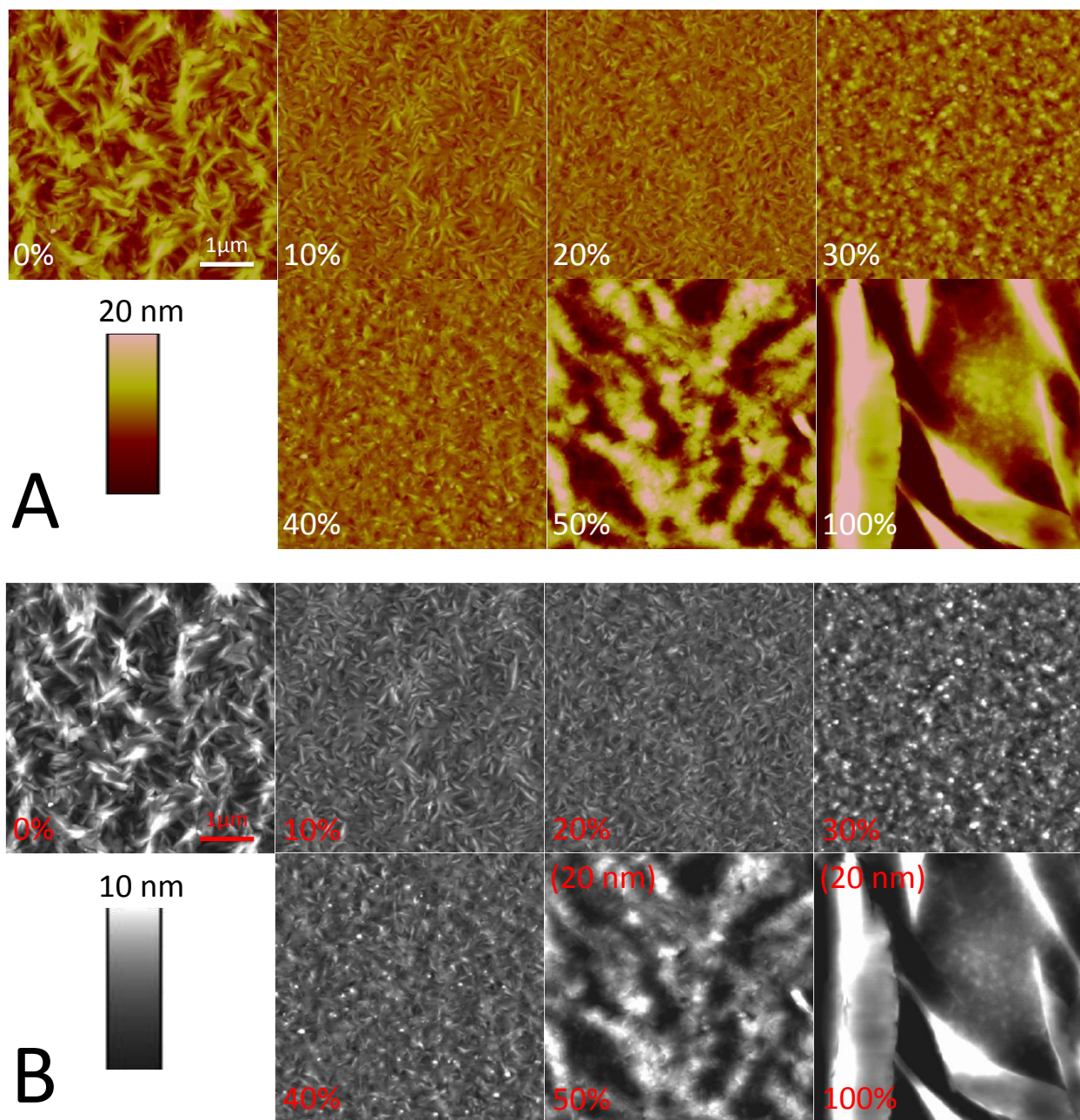


Figure 3-16. AFM images of increasing mole % symmetric oligomer in $[\text{il}(\text{TT})_2:\text{il}(\text{TT}-\text{Bu}_3\text{Si})_2]:\text{PC}_{61}\text{BM}$ devices, with the typical color scale (a) and in gray scale (b). All images shown are $5 \times 5 \mu\text{m}$, and have the same scale ($1 \mu\text{m}$). All images in (a) have a 20 nm height bar, and all images in (b) have a 10 nm height bar, except for 50 and 100 %, which have a 20 nm height bar.

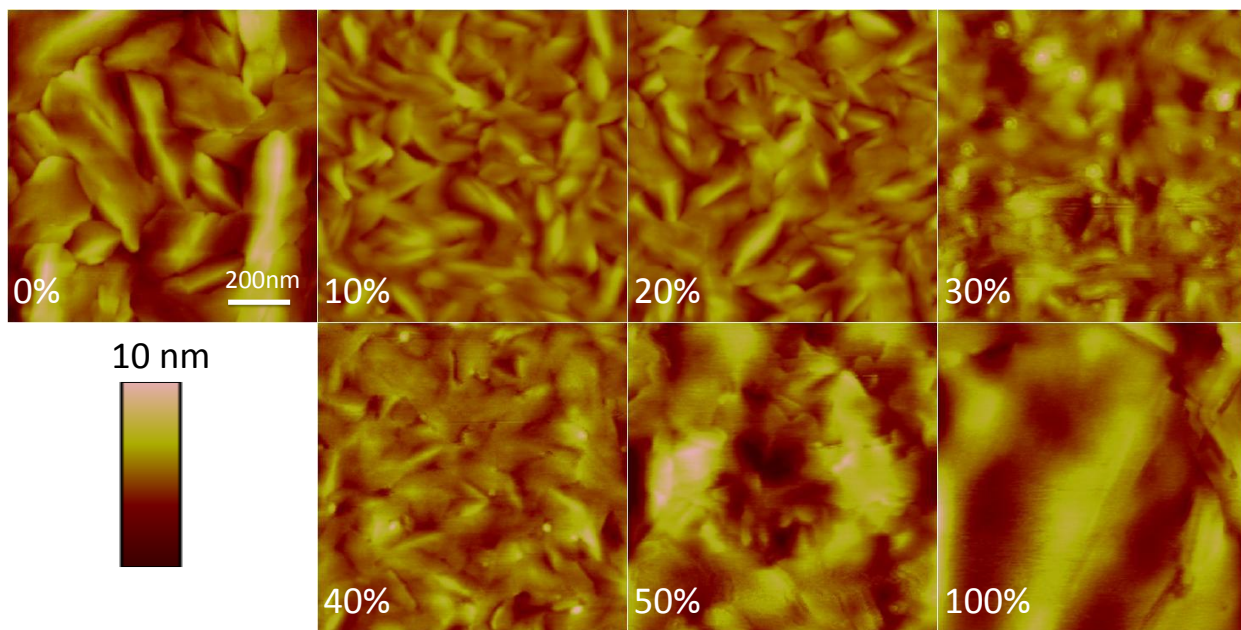


Figure 3-17. AFM images of increasing mole % symmetric oligomer in $[\text{il}(\text{TT})_2:\text{il}(\text{TT}-\text{IBu}_3\text{Si})_2]:\text{PC}_{61}\text{BM}$ devices. All images shown are $1 \times 1 \mu\text{m}$, and have the same scale (200 nm) and height bar (10 nm).

To further examine the features in the AFM images, Nanoscope 7.30 software was used to convert raw $5 \mu\text{m} \times 5 \mu\text{m}$ AFM images into gray scale figures (Figure 3-16b). These gray scale figures allow us to see more easily the changes in feature size and crystallinity. It can be seen in Figure 3-16b that the surface of the film begins to become more amorphous with the addition of 30 mole % $\text{il}(\text{TT}-\text{IBu}_3\text{Si})_2$, as realized with the typical color scale images (Figure 3-16a). However, the gray scale images allow us to see that the larger features begin forming in the 30 mole % device. These features are maxed out on the 10 nm height scale bar indicating their larger size than the rest of the surface. Such formation of larger crystallites already at the 30 mole % device can correlate to the sharp decrease in charge-carrier mobility observed in the SCLC devices.

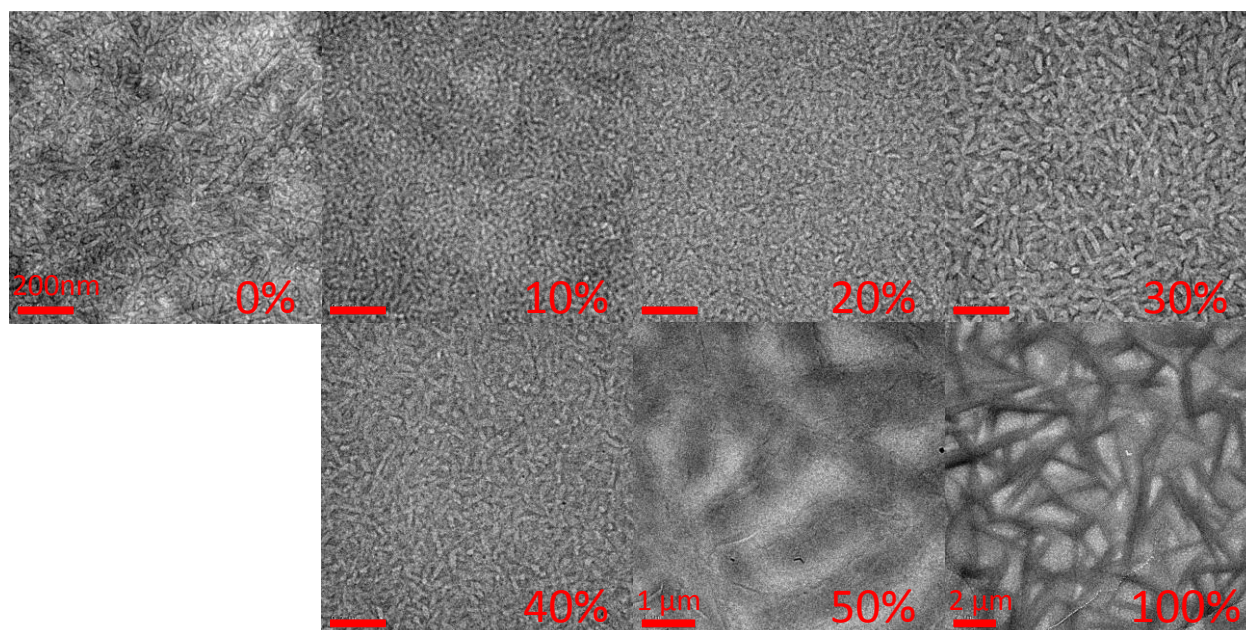


Figure 3-18. TEM images of increasing mole % symmetric oligomer in $[\text{il}(\text{TT})_2:\text{il}(\text{TT}-\text{IBu}_3\text{Si})_2]:\text{PC}_{61}\text{BM}$ devices. All images have the same 200 nm scale bar, with the exception of the 50 and 100 mole % devices, which were taken at a lower magnification.

Prior to making any conclusions about the relationship between morphology and device performance for $\text{il}(\text{TT}-\text{IBu}_3\text{Si})_2$, TEM images were taken. TEM samples were prepared in the same manner as described in chapter 2. Samples were imaged in an identical fashion to $\text{il}(\text{TT})_2-\text{IBu}_3\text{Si}$. TEM images for increasing mole % $\text{il}(\text{TT}-\text{IBu}_3\text{Si})_2$ are shown in Figure 3-18. As expected from the AFM images, the features drastically decrease upon initial addition of 10 mole % symmetric tailor-made additive. As with the asymmetric additive, these features are very distinct and appear crystalline. However, with addition of more than 20 mole % $\text{il}(\text{TT}-\text{IBu}_3\text{Si})_2$, the features become larger, but yet less distinct. This confirms the suspicion that arose from viewing the gray scale AFM images that larger crystallites begin to form after the addition of 30 mole % $\text{il}(\text{TT}-\text{IBu}_3\text{Si})_2$. The TEM images for 50 and 100 mole % $\text{il}(\text{TT}-\text{IBu}_3\text{Si})_2$ reveal very large features. The 50 mole % image was very difficult to image and it can be seen that there

is a large amorphous phase on the size of microns. These larger domains, containing features that are indistinguishable, match what was observed with AFM. Once the pure symmetric device, 100 mole % $\text{il}(\text{TT}-\text{iBu}_3\text{Si})_2$ is viewed, very large crystals are visible. These crystals are on the scale of several microns, and have somewhat discernable shapes.

It is evident from viewing AFM and TEM images, that with increasing mole % $\text{il}(\text{TT}-\text{iBu}_3\text{Si})_2$ in the $\text{il}(\text{TT})_2:\text{PC}_{61}\text{BM}$ heterojunction, feature sizes become larger. Such larger features may be due to the bulkiness of the triisobutylsilyl side groups on both ends of the isoindigo containing oligomer. These bulky groups inhibit planar packing in the solid state, leading to more amorphous films. Additionally, the bulky groups increase the intermolecular hopping distance, which in turn reduces the charge-carrier mobility, as was expressed in Figure 3-14.

3.5 $\text{il}(\text{TT})_2\text{-H}$

Thus far we have examined two tailor-made additives and their effects on morphology, OPV parameters, and charge-carrier mobilities in the $\text{il}(\text{TT})_2:\text{PC}_{61}\text{BM}$ heterojunction. However, both of the additives contained bulky triisobutylsilyl groups. To further investigate the effects of tailor-made additives, we now seek to determine if the bulky size of the end group alone leads to the morphological, performance, and mobility changes discussed.

To probe the effects of end-group size in tailor-made additives, another asymmetric derivative was synthesized. $\text{il}(\text{TT})_2\text{-H}$ is based on the same parent oligomer, $\text{il}(\text{TT})_2$ (Figure 3-2b), but has one linear hexyl side chain replaced with a small hydrogen atom (Figure 3-19).

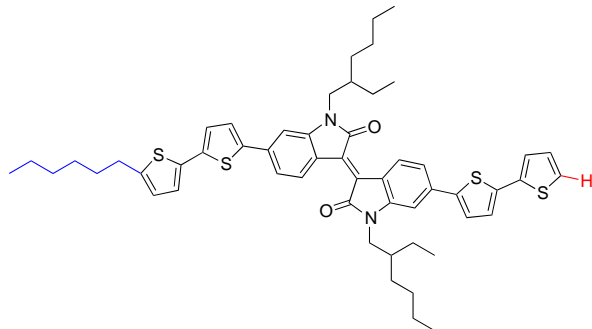


Figure 3-19. Chemical structure of an asymmetric tailor made additive, $\text{il(TT)}_2\text{-H}$.

3.5.1 Photovoltaic Performance

Photovoltaic cells containing the hydrogen end-capped tailor-made additive were prepared in the same manner as described in chapter 2, with increasing mole % $\text{il(TT)}_2\text{-H}$. Photovoltaic parameters are summarized in Table 3-3. Similar to the asymmetric triisobutylsilyl additive, $\text{il(TT)}_2\text{-tBu}_3\text{Si}$, there is an increase in V_{OC} with the addition of 10 and 20 mole % $\text{il(TT)}_2\text{-H}$ from 0.72 to 0.81 and 0.80 V, respectively. These devices also experienced an increase in J_{SC} from 4.58 to 5.53 and 5.51 mA cm^{-2} , and FF from 0.39 to 0.41 and 0.41, respectively. However, the increase in J_{SC} was not as significant as that which resulted from 10 and 20 mole % $\text{il(TT)}_2\text{-tBu}_3\text{Si}$. Consequently, the increase in PCE was not as significant as it was for $\text{il(TT)}_2\text{-tBu}_3\text{Si}$; with the addition of 10 and 20 mole % $\text{il(TT)}_2\text{-H}$, PCE increased from 1.30 to 1.82 and 1.81 %, respectively. Similar to the asymmetric and symmetric triisobutylsilyl additives, there is a decrease in V_{OC} , J_{SC} , FF and PCE with addition of 30 to 100 mole % $\text{il(TT)}_2\text{-H}$. The 100 mole % $\text{il(TT)}_2\text{-H}$ device exhibited a very low J_{SC} and PCE of 1.79 mA cm^{-2} and 0.33 %, respectively. Such a low PCE in the pure $\text{il(TT)}_2\text{-H:PC}_{61}\text{BM}$ device may be attributed to an amorphous film as was observed with the asymmetric triisobutylsilyl derivative. This will be further investigated in section 3.5.3.

Table 3-3. Summary of OPV parameters for increasing mole % asymmetric oligomer in [il(TT)₂:il(TT)₂-H]:PC₆₁BM solar cells under AM1.5G 100 mW cm⁻² simulated radiation.

mole %	V _{OC} (V)	J _{SC} (mA cm ⁻²)	FF	PCE (%)
0	0.72	4.58	0.39	1.30
10	0.81	5.53	0.41	1.82
20	0.80	5.51	0.41	1.81
30	0.68	4.95	0.34	1.16
40	0.73	4.37	0.30	0.95
50	0.74	3.99	0.29	0.87
100	0.64	1.79	0.29	0.33

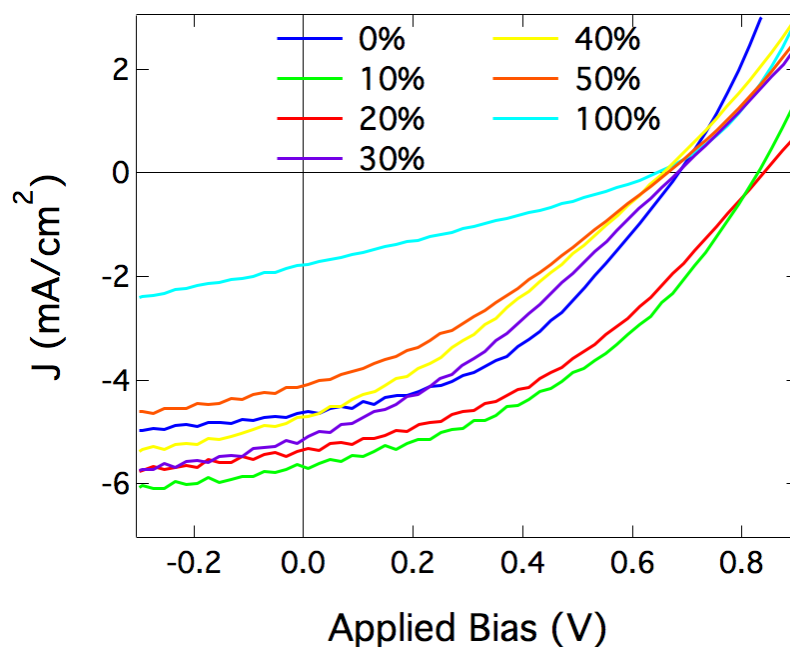


Figure 3-20. Representative J-V curves of 0 to 100 % asymmetric oligomer in [il(TT)₂:il(TT)₂-H]:PC₆₁BM solar cells under AM1.5G 100 mW cm⁻² simulated radiation.

3.5.2 Charge Mobility

To probe the effects of the hydrogen end-capped asymmetric tailor made additive on charge carrier mobility, SCLC devices were prepared as described in chapter 2 with increasing mole % il(TT)₂-H. A summary of average hole mobilities and respective standard deviations is given in Figure 3-21.

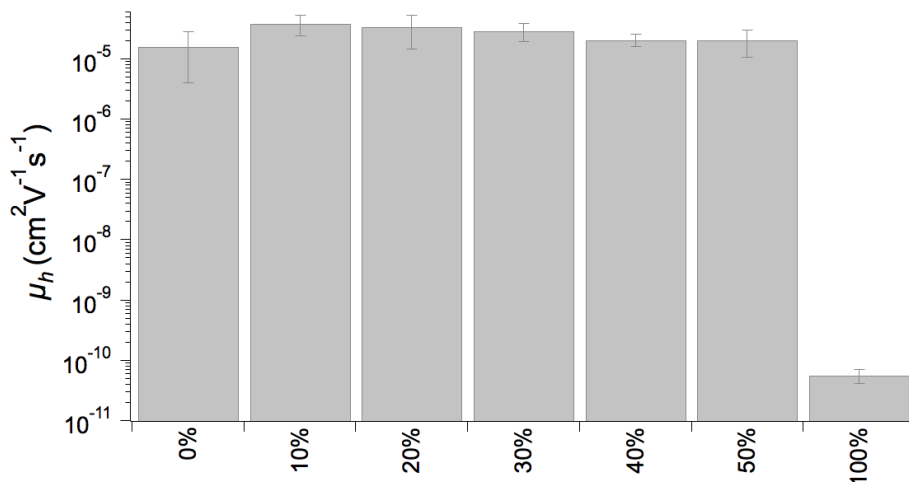


Figure 3-21. Summary of hole mobilities for increasing mole % asymmetric oligomer in [il(TT)₂:il(TT)₂-H]:PC₆₁BM SCLC devices. Values reported are averages of 6-8 pixels, with error bars showing +/- one standard deviation.

With the addition of 10 mole % il(TT)₂-H there is a slight increase in hole mobility from 1.6×10^{-5} to $3.9 \times 10^{-5} \text{ cm}^2 \text{ V}^{-1} \text{ s}^{-1}$. When additional il(TT)₂-H is added past 10 mole % there is a subsequent decrease in hole mobility, as was observed with the asymmetric and symmetric triisobutylsilyl additives. For il(TT)₂-H, however, the decrease in hole mobility is very slight; as 10 to 50 mole % is added there is only a decrease from 3.9×10^{-5} to $2.1 \times 10^{-5} \text{ cm}^2 \text{ V}^{-1} \text{ s}^{-1}$, respectively. This is very different than the triisobutylsilyl oligomers, which experienced orders of magnitude decreases in hole mobility. Such a steady hole mobility with increasing mole % il(TT)₂-H may be attributed to the small size of the hydrogen atom. Whereas the bulky triisobutylsilyl groups disrupted crystallographic packing and increased intermolecular hopping distances, the small hydrogen atom decreases the intermolecular hopping distance, and thus preserves the higher hole mobility. Finally, the pure il(TT)₂-H:PC₆₁BM device (100 mole %) experiences a decrease in hole mobility of 6 orders of magnitude to 5.7×10^{-11}

$\text{cm}^2 \text{V}^{-1} \text{s}^{-1}$. Such a drastic decrease in hole mobility may be a result of the formation of an amorphous film, as will be discussed in section 3.5.3.

3.5.3 Morphology

To obtain a fundamental understanding of device performance and nanostructure in the solid-state film, AFM and TEM were performed. AFM samples were prepared in the same manner as for OPVs, and images for increasing mole % $\text{il}(\text{TT})_2\text{-H}$ are shown in Figures 3-22 and 3-23 for $25 \mu\text{m}^2$ and $1 \mu\text{m}^2$ areas, respectively. Similar to $\text{il}(\text{TT})_2\text{-iBu}_3\text{Si}$, there is a decrease in domain size with the addition of 10 through 50 mole % $\text{il}(\text{TT})_2\text{-H}$. Unlike the $\text{il}(\text{TT})_2\text{-iBu}_3\text{Si}$ devices which showed sharp, discernable domains at concentrations of 10 to 30 mole % asymmetric oligomer, the $\text{il}(\text{TT})_2\text{-H}$ show such features all the way through the addition of 50 mole % asymmetric oligomer. Rather than the formation of an amorphous film early on, this may be attributed to a decreased rate of crystallinity. The pure $\text{il}(\text{TT})_2\text{-H:PC}_{61}\text{BM}$ image is similar to that of the pure $\text{il}(\text{TT})_2\text{-iBu}_3\text{Si:PC}_{61}\text{BM}$ image, indicating an amorphous film. However, some aggregate-type features are visible in the 100 mole % $\text{il}(\text{TT})_2\text{-H}$ image. Such aggregates may be the result of a decrease in solubility. Compared to the previous two tailor-made additives, $\text{il}(\text{TT})_2\text{-H}$ lacks the alkyl solubilizing groups of the hexyl chains and triisobutyl groups, resulting in a lower solubility.

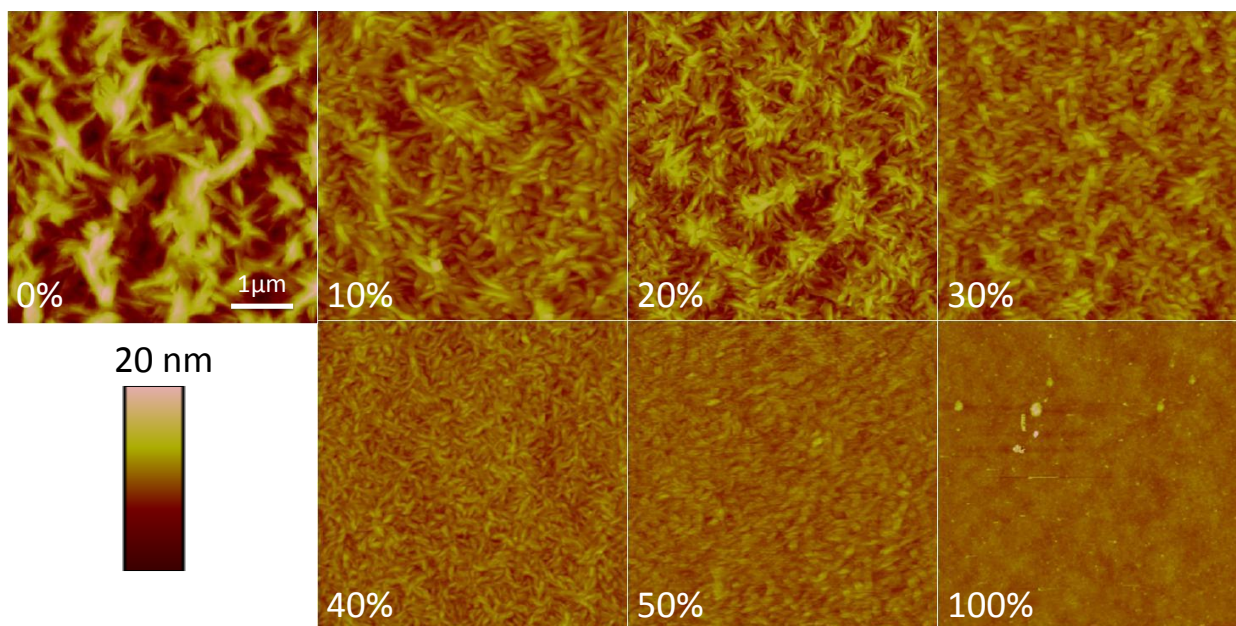


Figure 3-22. AFM images of increasing mole % asymmetric oligomer in [il(TT)₂:il(TT)₂-H]:PC₆₁BM devices. All images shown are 5 × 5 μm, and have the same scale (1 μm) and height bar (20 nm).

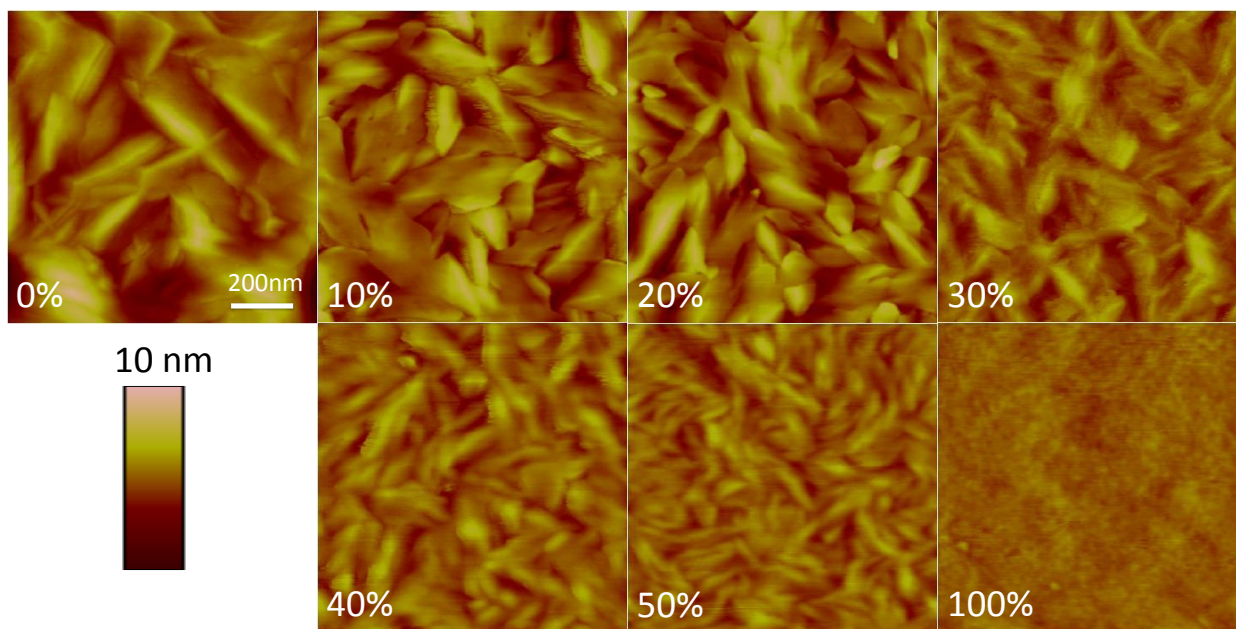


Figure 3-23. AFM images of increasing mole % asymmetric oligomer in [il(TT)₂:il(TT)₂-H]:PC₆₁BM devices. All images shown are 1 × 1 μm, and have the same scale (200 nm) and height bar (10 nm).

As stressed before, to be certain of solid-state nanostructure, additional morphology characterization was conducted for il(TT)₂-H devices. TEM samples were

prepared using the procedure described in chapter 2 and the films used for AFM characterization. TEM images are summarized in Figure 3-24, and overall show similarities with the AFM images obtained. TEM reveals a decrease in feature size as increasing mole % $\text{il}(\text{TT})_2\text{-H}$ is added. The features remain sharp and their shapes are discernable. Finally, the pure $\text{il}(\text{TT})_2\text{-H}$ device (100 mole %) shows an amorphous film, resulting in a 6 order of magnitude decrease in hole carrier mobility.

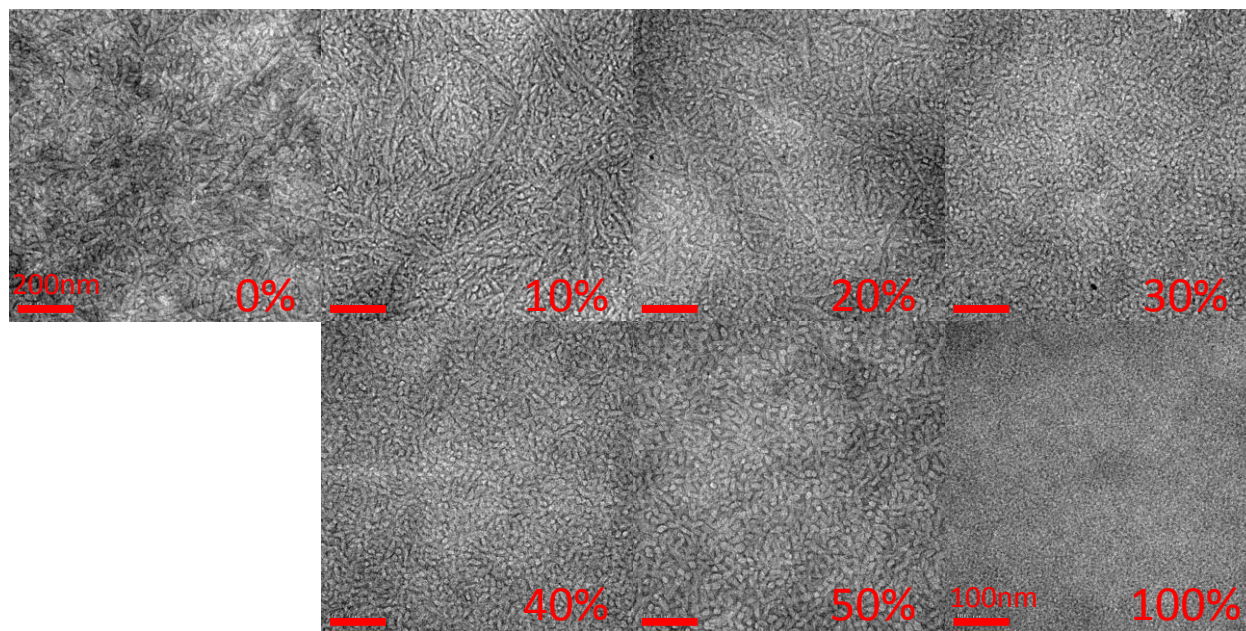


Figure 3-24. TEM images of increasing mole % asymmetric oligomer in $[\text{il}(\text{TT})_2:\text{il}(\text{TT})_2\text{-H}]:\text{PC}_{61}\text{BM}$ devices. All images have the same 200 nm scale bar, with the exception of the 100 mole % device, which was taken at a higher magnification.

3.6 Chapter Summary

The use of tailor-made additives to fine tune morphology, and consequently PCE has been demonstrated. Asymmetric and symmetric additives were prepared and incorporated into BHJ OPVs. Additionally, the end-group size of the additive was also varied to determine the effects on morphology and OPV performance.

The triisobutylsilyl containing asymmetric oligomer, $\text{il}(\text{TT})_2\text{-}i\text{Bu}_3\text{Si}$ was shown to decrease domain sizes with the addition of 20 mole %, resulting in an almost two-fold increase in PCE. Charge-carrier mobilities were measured and found to decrease with increasing mole % asymmetric oligomer due to inhibited crystallographic packing because of the bulky triisobutylsilyl group. Increased intermolecular hopping distances due to the size of triisobutylsilyl compared to the linear hexyl chain resulted in significantly lower hole-carrier mobilities. Crystallization studies were performed to show $\text{il}(\text{TT})_2\text{-}i\text{Bu}_3\text{Si}$ decreases the rate of crystallization in the $\text{il}(\text{TT})_2\text{:PC}_{61}\text{BM}$ heterojunction. However, crystals were visible in the pure $\text{il}(\text{TT})_2\text{-}i\text{Bu}_3\text{Si}$ microscope images indicating the asymmetric oligomer's ability to crystallize on its own.

A symmetric analogue tailor-made additive containing two triisobutylsilyl groups was synthesized to determine if the asymmetry alone afforded morphological changes. $\text{il}(\text{TT}-i\text{Bu}_3\text{Si})_2$ showed decreases in domain sizes and PCE. Charge-carrier mobilities decreased even more compared to the asymmetric derivative. TEM and AFM images revealed the formation of large crystallites on the order of several microns with the addition of 50 and 100 mole % symmetric additive. Such large crystallites and decreases in OPV and charge-carrier performance indicate inhibition of crystallographic packing to a larger extent than was observed with the asymmetric derivative, due to the reduced amount of linear hexyl chains and increasing amount of bulky triisobutylsilyl groups.

An asymmetric tailor-made additive containing a small hydrogen end-group was synthesized to determine if the size of end-group contributed to morphological changes. $\text{il}(\text{TT})_2\text{-H}$ showed a constant decrease in domain size leading to a completely

amorphous film. OPV devices showed an initial increase in PCE with small concentrations of $\text{il(TT)}_2\text{-H}$. The small size of the hydrogen atom led to decreased intermolecular hopping distances resulting in a rather steady charge-carrier mobility with increasing $\text{il(TT)}_2\text{-H}$.

As evidenced with the three tailor-made additives presented in this work, the asymmetry alone leads to morphological changes and an increase in PCE. However, careful selection of the end-group is necessary to achieve higher PCEs, as was demonstrated with triisobutylsilyl and hydrogen end-capped oligomers. This work shows that tailor-made additives have promise in the field of optoelectronics for optimizing device performance. We believe tailor-made additives may be synthesized for a variety of electroactive materials to tune morphology and achieve reproducibly high PCEs in molecular BHJ OPVs.

CHAPTER 4 ELECTROACTIVE POLYOLEFINS WITH PRECISELY CONTROLLED CHROMOPHORE SPACING

The design of π -conjugated organic materials for optoelectronic applications has become an art. As described in chapter 1, there are a variety of electroactive entities to choose from when designing molecular and polymeric materials for light-emitting devices. When it comes to molecular materials, proper chromophore choice is of importance for fabricating quality devices. A material must be designed so that when incorporated into a solid-state device, there is a balance between the electron and hole mobilities for efficient exciton generation and charge recombination.^{13,15,26,83,126} Additionally, to fabricate high performance devices, materials with high fluorescence quantum yields in the solid-state are necessary.¹²⁷⁻¹²⁹ Compared to their molecular counterparts, polymeric materials may be advantageous when rationally designing π -conjugated systems for light-emitting devices. As polymers contain a system of repeat units, the design of the material is not limited as it is in small molecules. This chapter will explore a class of polymeric materials, which are not ordinary in the field of optoelectronics, for systematic control of efficiency and hole mobility.

4.1 Electroactive Polyolefins

Polymeric materials are advantageous over their molecular counterparts as their ordered structure may be specifically tailored. Typical conjugated polymers have delocalized electrons along the backbone, not localized on a single chromophore; and functionalization is branched off the main chain (Figure 4-1a).¹³⁰ Such polymers typically differ in electrical and optical properties than their monomers, but nonetheless can be tuned to emit particular wavelengths achieving a desired color of light.¹³¹

Another class of polymers are main chain π -functional systems. These polymers contain well-defined chromophores, which are connected along an electrically insulated backbone (Figure 4-1b). Such polymers may contain various electroactive entities with varying emissive properties to produce a polymer with desired characteristics.^{13,15,20,132} The last class of polymeric materials are side chain π -functional systems, which will be the focus of this work. These materials contain an electrically insulating aliphatic backbone, with π -conjugated electroactive entities pendant to the backbone (Figure 4-1c).^{133–136} Such a class of materials may be referred to as electroactive polyolefins, whereas traditional polyolefins are desired for cable enclosures due to their electrically insulating properties.^{137,138}

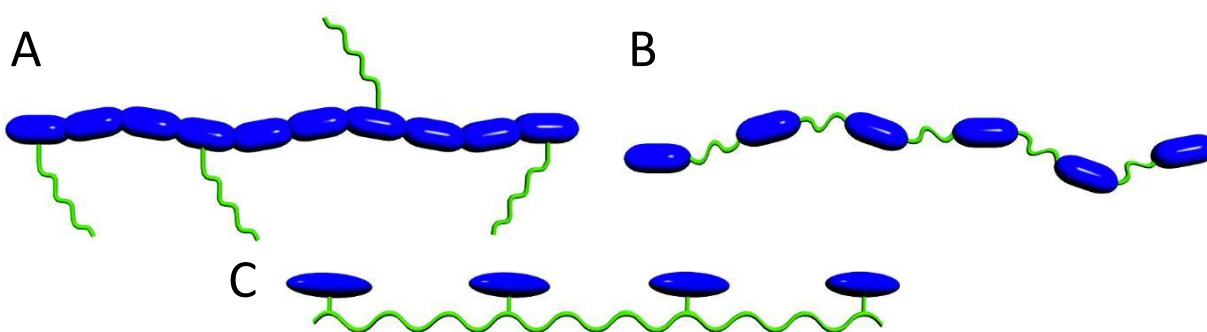


Figure 4-1. Typical electroactive polymer system structures—conjugated polymers (a), main chain π -functional polymers (b) and side chain π -functional polymers (c). Adapted with permission from Aitken, B. S.; Wieruszewski, P. M.; Graham, K. R.; Reynolds, J. R.; Wagener, K. B. *Macromolecules* **2012**, 45 (2), 705. Copyright 2012 American Chemical Society.

Electroactive polyolefins are of interest in this work as they combine electrical and optical properties from pendant chromophore groups with a solubilizing aliphatic backbone. Various electroactive entities may be combined and placed pendant to the backbone for fine-tuning of properties. These characteristics provide for a world of

possibilities in designing optoelectronic materials for highly efficient, solution processable devices.

To synthesize side chain π -functional polymers, ring-opening metathesis polymerization (ROMP) has been used extensively.^{136,139–141} However, ROMP typically affords polymers with variable spacing, and is limited to several carbons. Such polymers have been applied to hole-transporting materials,¹⁴⁰ light-emitting diodes,¹³⁹ and conductive polymers.¹³⁶ ROMP, however, does not produce precisely “regioregular” side chain π -functional polymers, but rather polymers with variable spacer length. For this work, we seek to obtain a fundamental understanding of electroactive entity spacing on an aliphatic backbone on device performance.

To synthesize regioregular side chain π -functional polyolefins, acyclic diene metathesis (ADMET) polymerization can be used. First proposed by Dr. Kenneth B. Wagener at the University of Florida, ADMET polymerization allows for the synthesis of regioregular polyolefins through symmetric α,ω -diene functionalized electroactive chromophores.¹⁴² In this work, ADMET polymerization was used to prepare regioregular terfluorenylidene for PLEDs and regioregular triarylamine containing polyfluorenes for hole-transporting materials. We seek to systematically control device performance with chromophore spacer length along the polymer backbone.

4.2 Perfectly Regioregular Terfluorenylidene Polymers

To probe the effects of chromophore spacing on device performance, a family of electroactive terfluorenylidene containing polymers was synthesized. ADMET polymerization was used to synthesize polymers with a terfluorenylidene chromophore on each 8th, 14th, and 20th carbon of an unsaturated aliphatic backbone (Figure 4-2a). The backbone was further hydrogenated to afford another series of polymers with

identical chromophores and spacing on a saturated backbone (Figure 4-2b). In addition to the regioregular terfluorenylidene polyolefins, regiorandom unsaturated (Figure 4-2c) and saturated (Figure 4-2d) analogues were synthesized. For full synthetic procedure and characterization discussion, the reader is directed to the appropriate publication.⁸⁷ For further discussions regarding this set of polymers, the acronyms presented in Figure 4-2 will be used.

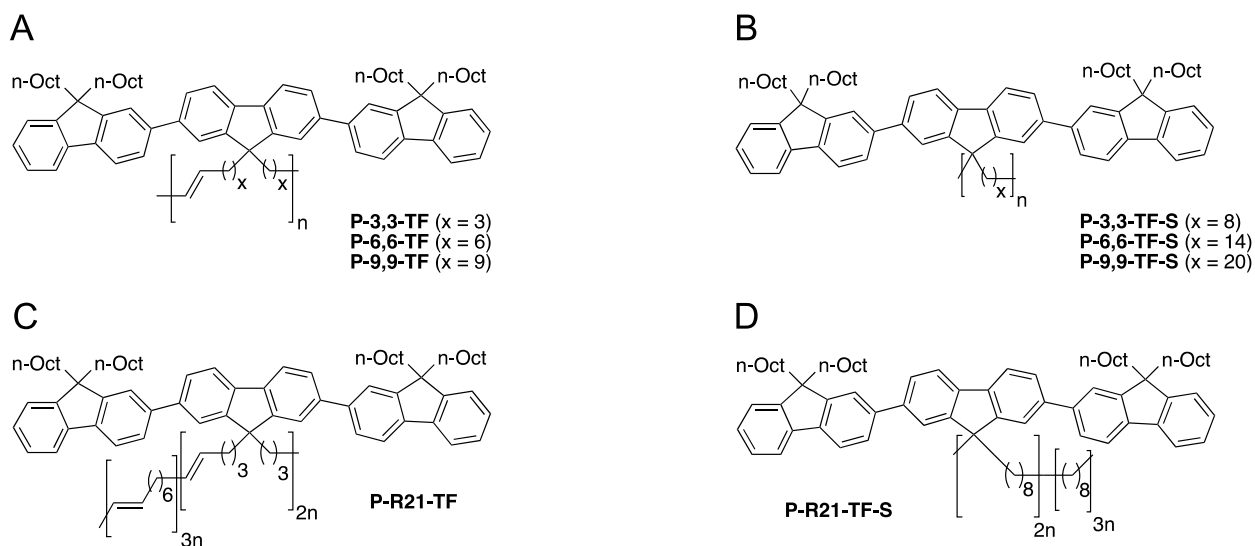


Figure 4-2. Family of electroactive terfluorenylidene polymers—regioregular unsaturated (a), regioregular saturated (b), regiorandom unsaturated (c), and regiorandom saturated (d).

Polymer light-emitting diodes were fabricated with each of the polymers in the family, using the procedure described in chapter 2. Devices were prepared with an architecture of substrate/ITO/PEDOT:PSS/active layer/LiF/Al. An interesting pixel phenomenon was observed with the P-9,9-TF-S device, which will be discussed later.

4.2.1 Electroluminescence

To probe electroluminescence (EL), a fresh device was placed inside the device holder, and the method discussed in chapter 2 was employed. EL spectra of the saturated polymers at a constant driving bias are shown in Figure 4-3. Since the

chromophores are identical in each polymer, their basic EL spectra are the same. However, there are some slight differences between them, most realized with the regiorandom polymer, P-R21-TF-S. This can be explained due to varied interaction between chromophores in the non-ordered polymer (regiorandom) as opposed to the precisely ordered polymers (regioregular). The variations in EL spectra between the regioregular polymers, P-3,3-TF-S, P-6,6-TF-S, and P-9,9-TF-S can again be explained by the different interactions as the amount of spacing between chromophores changes.

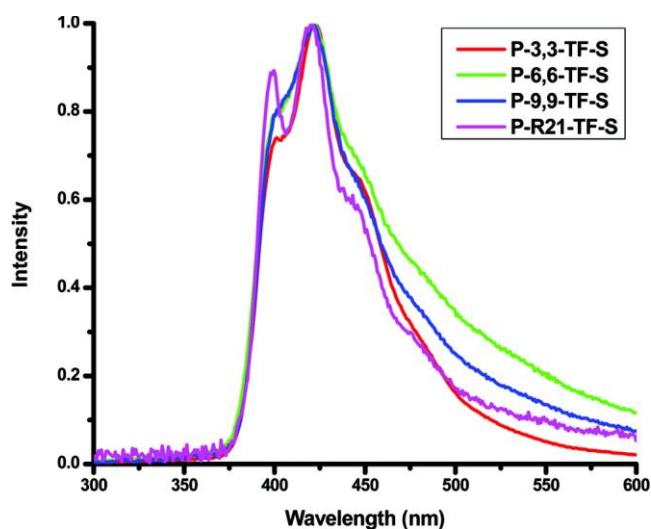


Figure 4-3. Electroluminescence spectra of saturated polymers at a constant driving bias. Reprinted with permission from Aitken, B. S.; Wieruszewski, P. M.; Graham, K. R.; Reynolds, J. R.; Wagener, K. B. *Macromolecules* **2012**, 45 (2), 705. Copyright 2012 American Chemical Society.

4.2.2 Luminance

To probe the brightness of devices fabricated with the family of terfluorenylidene polymers, luminance was measured. Figure 4-4 shows luminance and current density as a function of driving voltage for unsaturated and saturated polymers. Unlike the EL spectra (Figure 4-3), the devices exhibit very different J-V characteristics. It can be seen that as chromophore spacer length increases, current density drops (at a constant

bias). Though not studied in this work, the decrease in current density may be the result of decrease charge-carrier mobilities. Since the chromophores are pendant to the main chain, increasing the distance between them increases the intermolecular hopping distance, resulting in lower charge-carrier mobilities.

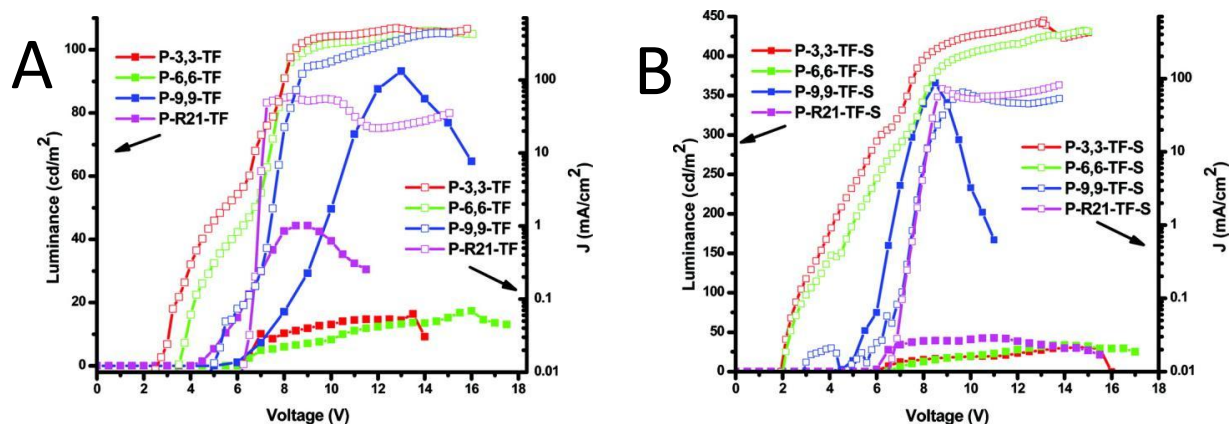


Figure 4-4. Luminance and current density as a function of driving voltage for unsaturated (a) and saturated (b) polymers. Data presented is for individual pixels. Reprinted with permission from Aitken, B. S.; Wieruszewski, P. M.; Graham, K. R.; Reynolds, J. R.; Wagener, K. B. *Macromolecules* **2012**, 45 (2), 705. Copyright 2012 American Chemical Society.

Luminance, on the other hand, exhibits a much less ordered trend than the current density, though it is still somewhat systematic. With low chromophore spacing, P-3,3-TF, P-3,3-TF-S, P-6,6-TF and P-6,6-TF-S, exhibit low luminance values of $<35 \text{ cd m}^{-2}$. The regiorandom polymers, P-R21-TF and P-R21-TF-S, follow with slightly higher maximum luminance values of 43 and 45 cd m^{-2} , respectively. Finally the polymers with the largest chromophore spacing, P-9,9-TF and P-9,9-TF-S, exhibit the largest maximum luminance values of 93 and 366 cd m^{-2} , respectively.

Though the data presented in Figure 4-4 is of just a single pixel, it will be shown in section 4.2.3 that these results can be confidently accepted as uniform throughout the

device. Thus, for this class of polymers, a lower chromophore density (increased chromophore spacer length) is advantageous for increased brightness.

4.2.3 PLED Performance

After investigating the brightness, which is important when applying materials in an industrial setting, we investigated the performance of the devices. The performance of PLEDs was probed using a silicon photodiode and the procedure described in chapter 2. As with the EL, luminance, and current density characteristics, a trend with the external quantum efficiency (EQE) is also noticed. Calculated EQEs for the entire family of terfluorenylidene polymers are presented in Figure 4-5. Average and max EQEs are presented for at least 8 pixels; with the error bars indicating one standard deviation. Indicated by the relatively low standard deviations, there is little pixel-to-pixel variation within a device. Thus, the current density and luminance data presented in Figure 4-4 can be confidently accepted as accurately representing any pixel on the device.

PLED EQE data presented in Figure 4-5 show similar trends as luminance and current density data. There is an increase in EQE as the spacing between chromophores increases (decreasing chromophore density). Additionally, saturating the backbone is beneficial to PLED performance, as shown by increasing EQEs. This increase is most evident in P-9,9-TF-S, which exhibits a two-fold increase in EQE upon saturation. As shown before, P-9,9-TF-S also shows a three-fold increase in luminance upon saturation. This odd behavior will be described in section 4.2.4. It can be concluded from this data that device performance increases as spacer length between chromophores increases, or chromophore density decreases.

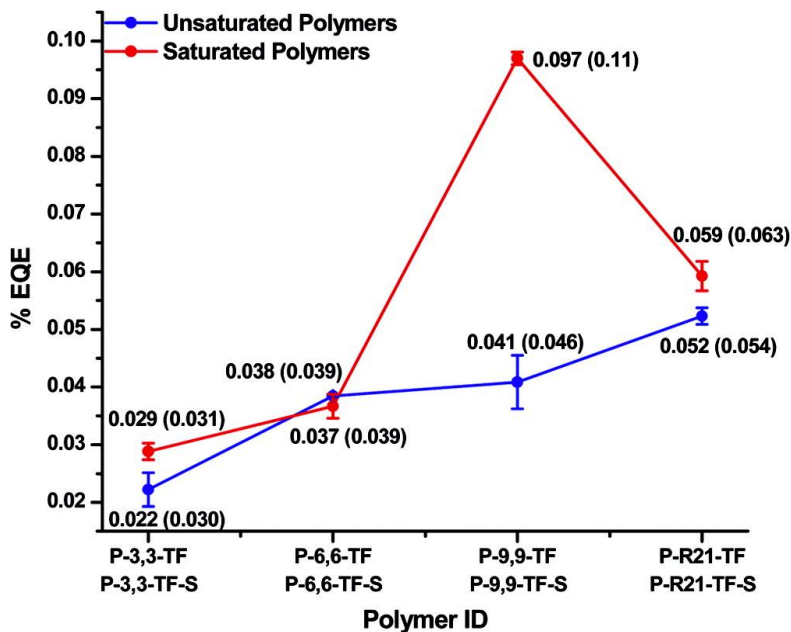


Figure 4-5. Calculated EQEs for the entire family of terfluorenylidene polymers. Data is represented as: average EQE (max EQE), with error bars giving one standard deviation. Reprinted with permission from Aitken, B. S.; Wieruszewski, P. M.; Graham, K. R.; Reynolds, J. R.; Wagener, K. B. *Macromolecules* **2012**, 45 (2), 705. Copyright 2012 American Chemical Society.

4.2.4 Pixel Anomaly

As shown through luminance and PLED EQE calculations, P-9,9-TF-S is an outlier when considering the general trend of spacer length. AFM images were taken of P-3,3-TF-S, P-6,6-TF-S, and P-9,9-TF-S using the procedure described in chapter 2 and are presented in Figure 4-6. Calculated surface roughnesses of these images were 0.308, 0.200, and 0.235 nm, respectively. Such roughness data indicate very flat films with no features or aggregation.

Upon closer investigation, it was noticed that the top aluminum electrode had a different appearance on the P-9,9-TF-S device. Immediately upon removal from the thermal evaporation chamber, inside the glovebox, a surface coloration was visually apparent. As described in chapter 2, thermal evaporation vapor deposits metals at very high temperatures. Since the device holder has room for 8 devices (Figure 2-3), all

devices received the top aluminum electrode during the same deposition. Thus, the variation in electrode color may be a result of a temperature-dependent property of the P-9,9-TF-S polymer, rather than experimental error or the presence of impurities.

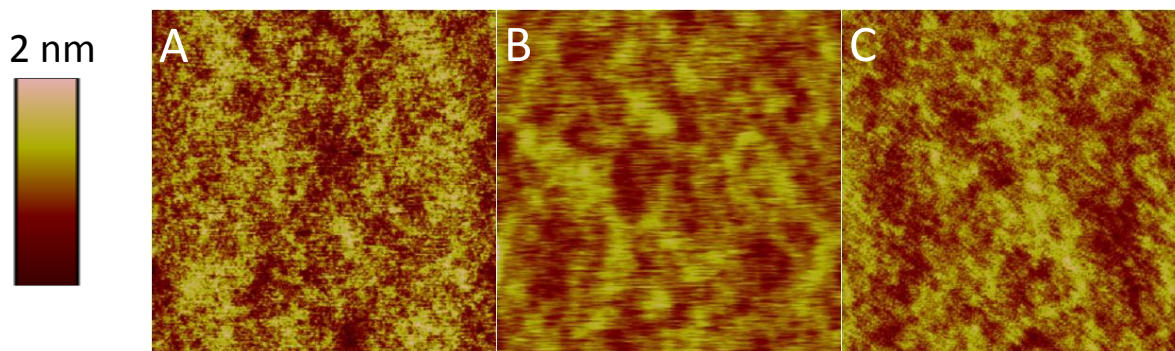


Figure 4-6. AFM images of P-3,3-TF-S (a), P-6,6-TF-S (b), and P-9,9-TF-S (c). All images are $5\ \mu\text{m} \times 5\ \mu\text{m}$ and have a same 2 nm height scale bar. Adapted with permission from Aitken, B. S.; Wieruszewski, P. M.; Graham, K. R.; Reynolds, J. R.; Wagener, K. B. *Macromolecules* **2012**, 45 (2), 705. Copyright 2012 American Chemical Society.

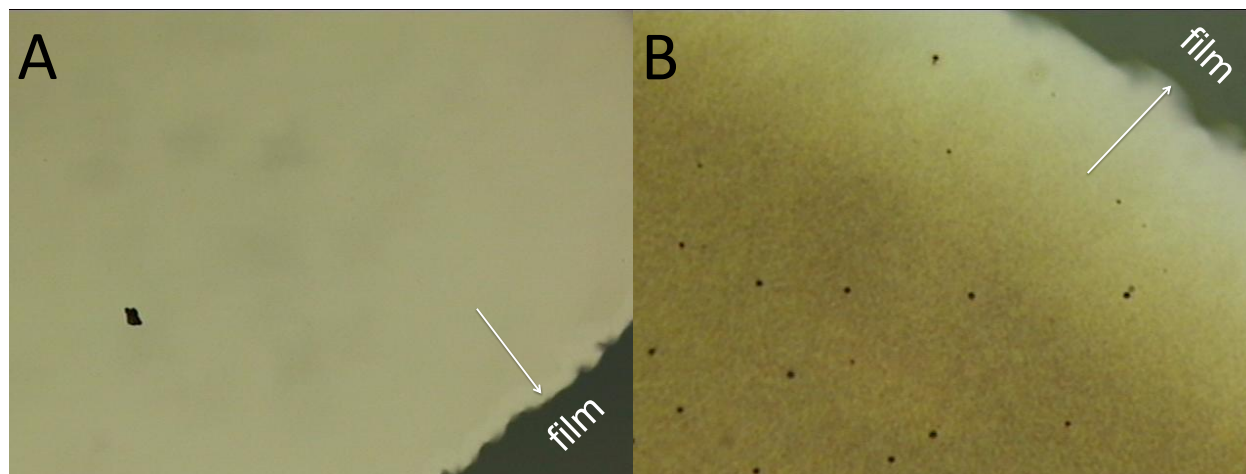


Figure 4-7. Optical microscope images of the aluminum electrode on devices with P-3,3-TF-S (a), and P-9,9-TF-S (b). Arrows point to the Al/film edge. Adapted with permission from Aitken, B. S.; Wieruszewski, P. M.; Graham, K. R.; Reynolds, J. R.; Wagener, K. B. *Macromolecules* **2012**, 45 (2), 705. Copyright 2012 American Chemical Society.

Further inspection under an optical microscope revealed indeed a surface coloration as well as a surface roughness of the aluminum electrode on the P-9,9-TF-S device (Figure 4-7b). Typically, the aluminum electrode appears smooth and has a

shiny metallic surface, as was observed for P-3,3-TF-S (Figure 4-7a). Analysis of surface features of the aluminum electrodes *via* AFM was difficult and not achieved.

The variation in electrode appearance may be a result of the thermal characteristics of P-9,9-TF-S. Differential scanning calorimetry (DSC) was used to calculate a T_g of 34 °C for P-9,9-TF-S, which is near room temperature. We are led to believe that the coloration upon device removal from the thermal evaporation chamber was a result of the high temperatures during deposition. Since the temperature required to vaporize metals is high, there could be sufficient energy to surpass the T_g . This would result in rearrangement of polymer chains underneath the electrode during thermal deposition, altering the morphology of the aluminum electrode.

Upon testing the devices, a fluctuation in pixel light output was visible for P-9,9-TF-S. Typically when a bias is applied to a PLED, light is uniformly emitted from the pixel (Figure 2-8). However, when P-9,9-TF-S was turned on, luminosity was visually changing. A video was taken of a P-9,9-TF-S pixel at a constant driving bias of 13 V, and can be viewed in Object 4-1. Figure 4-8 shows time-lapsed images of a pixel from the video.

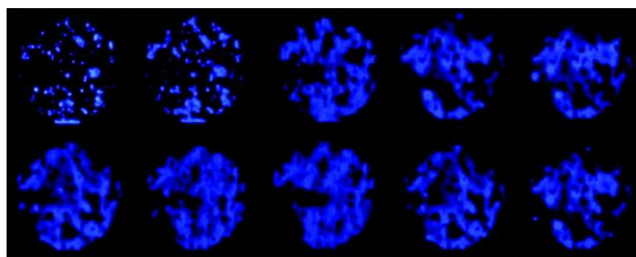


Figure 4-8. Time-lapsed images taken every 2.5 s of a P-9,9-TF-S pixel at a constant driving bias of 13 V, starting from the top left and ending at the bottom right. Reprinted with permission from Aitken, B. S.; Wieruszewski, P. M.; Graham, K. R.; Reynolds, J. R.; Wagener, K. B. *Macromolecules* **2012**, 45 (2), 705. Copyright 2012 American Chemical Society.

[Object 4-1. Video of a P-9,9-TF-S pixel at a constant bias of 13 V \(.avi file 20.6 MB\)](#)

The fluctuation in PLED luminosity during testing is less questionable than the electrode appearance. Since the fluctuation is observed when a bias is applied and the device is turned on, it may also be a result of the low T_g of P-9,9-TF-S. An explanation for this may be the presence of Joule heating, an electro-thermal phenomenon typically experienced in transistors and electronic devices, first proposed by James Joule in 1841.¹⁴³ Also referred to as resistive heating, Joule heating describes the generation of heat due to a current passing, and can be quantified by:

$$P = I^2R \quad (4-1)$$

Where P is the power dissipated, I is the current flow and R is the resistance of the material. Though it would be very difficult to calculate the exact temperature at which the device is raised to during testing, Joule heating has been known to raise the temperature of PLEDs several tens of degrees.¹⁴⁴⁻¹⁴⁶ Such a rise in temperature may provide sufficient energy to surpass the T_g and cause polymer chain rearrangement underneath the electrode. This movement would in turn result in the temporal and spatial morphological changes observed in the video of the pixel.

To completely confirm the speculation that the fluctuation in pixel luminosity is a result of Joule heating, the device would need to be tested at extremely low temperatures. A possible method to do this would be to devise an experimental apparatus that can be fully submerged in liquid nitrogen. This would keep the device at liquid nitrogen temperature during testing, causing the heat generated by Joule heating to be negligible. Due to time constraints and experimental limitations, however, this was not carried out in this work.

4.3 Sequenced Triarylamine Functionalized Polyolefins

For PLEDs to be competitive with their molecular and inorganic counterparts, charge carrier mobilities must be balanced for effective charge recombination.^{79,83,126} Highly efficient organic light-emitting devices operate with a multilayer structure consisting of an active layer sandwiched by an electron transport layer and a hole transport layer.^{77,78,82,147–149} To date, there has been much research effort geared towards synthesizing and optimizing electron^{78,82,150–153} and hole^{16,36,40,81,134,147,154–156} transport layers for high performance multilayer organic electronic devices. In some cases, reduced hole mobilities are in fact beneficial to device performance as hole mobilities typically exceed electron mobilities.⁸³ To achieve efficient charge transport, charge carrier mobilities must be balanced. In fact, studies where hole mobilities were purposefully reduced to fabricate highly efficient blue light-emitting devices have been conducted.¹⁵⁷

To our knowledge, however, polymeric materials with precisely spaced chromophores along an aliphatic backbone have not been applied as charge-carrying layers in light-emitting devices. Having demonstrated systematic control of PLED EQE *via* inter-chromophore distance on pendant π -functional polymers,⁸⁷ we were compelled to study hole-injection materials.

A family of pendant π -functional polyolefins with triarylamine flanked fluorenes were synthesized *via* ADMET.⁸⁸ Synthesis afforded polymers with chromophores on every 9th, 15th, and 21st carbon on an unsaturated backbone (Figure 4-9a). The backbone was further hydrogenated to afford identically spaced chromophores on a saturated backbone (Figure 4-9b). The design of chromophores was based on prior advances in light-emitting devices. Triarylaminines have been demonstrated as efficient

hole-injectors in OLEDs.^{80,158–163} A triarylamine flanked polyfluorene, or 2,7-bis(phenyl-*m*-toluylamino)fluorene (TPF) has been studied as a hole transporter that can be modified into polymer structures.⁸⁰ Additionally TPF is structurally similar to a more common hole transporter in OLEDs, TPD (4,4'-bis(phenyl-*m*-toluylamino)biphenyl) (Figure 1-14a).¹⁵⁹ Combining the hole transporting properties of TPF and a solubilizing aliphatic backbone, we believe this class of hole transporting materials can systematically control charge carrier mobilities for highly efficient PLEDs.

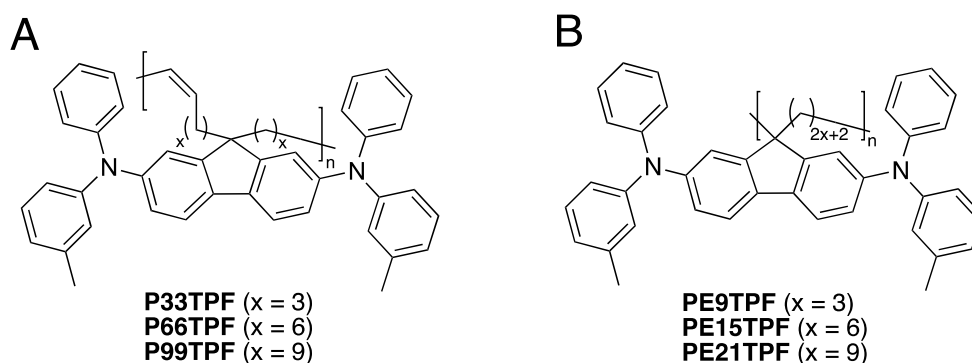


Figure 4-9. Family of regioregular sequenced triarylamine functionalized polyolefins—unsaturated (a) and saturated (b) hole transporters.

To probe the effects of spacer length in the TPF polymers, space-charge limited current (SCLC) devices were prepared as described in chapter 2. Devices were fabricated with an architecture of glass/ITO/PEDOT:PSS/active layer/gold. Unlike SCLC devices made with OPV materials, which used MoO₃ as the hole-injecting layer, these devices received PEDOT:PSS instead. Though MoO₃ is known to be an efficient hole transporting layer,^{36,164} J-V characteristics better fit the SCLC model with PEDOT:PSS containing devices with these TPF polymers. This may be advantageous from an industrial point of view as PEDOT:PSS is spun cast from aqueous solution, whereas MoO₃ requires high vacuum vapor deposition, which is quite costly.

Hole mobilities were calculated using the field-dependent SCLC model (Equation 1-14), with a thickness (L) of 70 nm, determined by tapping mode AFM. Average hole mobility data and current-voltage characteristics are summarized in Figures 4-10a and 4-10b, respectively. Immediately, it is noticed that the current, and consequently hole mobility, decreases with increasing space between chromophores, with the exception of PE9TPF, which will be discussed later.

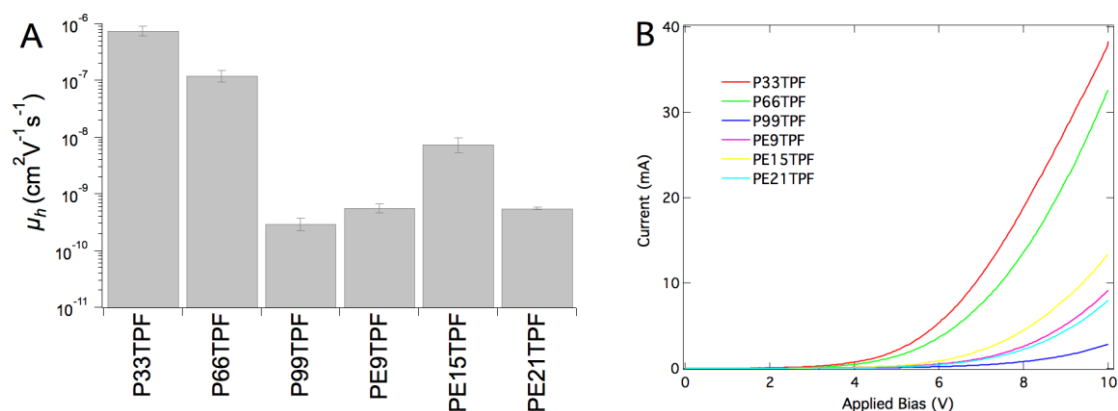


Figure 4-10. Summary of average hole mobility data (a) and current-voltage characteristics (b) for SCLC devices. For image a, the error bars indicate one standard deviation for a minimum of 8 pixels. Adapted (a) and reprinted (b) with permission from Aitken, B. S.; Wieruszewski, P. M.; Graham, K. R.; Reynolds, J. R.; Wagener, K. B. *ACS Macro Letters* **2012**, 1 (2), 324. Copyright 2012 American Chemical Society.

Representative current density-voltage curves with SCLC fits are presented in Figure 4-11a and 4-11b for unsaturated and saturated polymers, respectively. These SCLC fits represent a single pixel, however, average hole mobilities presented in Figure 4-10a show a very small standard deviation allowing us to accept these J-V curves as accurately representing any given pixel on a device. The decrease in current, and consequently hole mobility can be attributed to the structure of the materials. As spacer length between chromophores on the aliphatic, and thus electrically insulating backbone

increases, the intermolecular hopping distance also increases. Since the intermolecular hopping distance is increased, hole mobility is thus decreased.

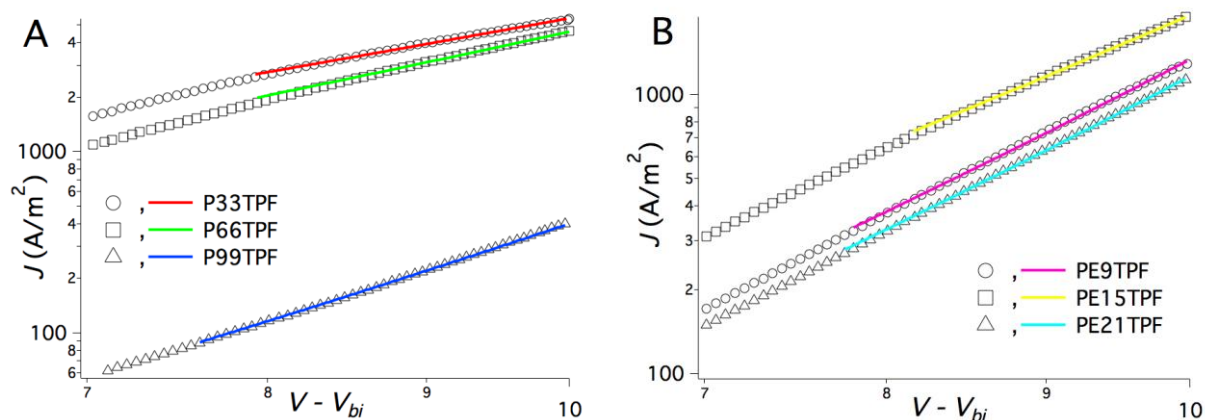


Figure 4-11. Representative J-V plots of unsaturated (a) and saturated (b) TPF polymer containing SCLC devices. Data and SCLC fits represent individual pixels. Adapted with permission from Aitken, B. S.; Wieruszewski, P. M.; Graham, K. R.; Reynolds, J. R.; Wagener, K. B. *ACS Macro Letters* **2012**, 1 (2), 324. Copyright 2012 American Chemical Society.

There is however an exception to the general trend of spacer length and hole mobility—PE9TPF. After hydrogenating the backbone of P33TPF, the afforded polymer, PE9TPF, had a compromised solubility. This was possibly a result of the necessity to run the hydrogenation dilute, with a larger amount of catalyst; and thus the presence of residual catalyst in the resulting saturated polymer. Consequently, when SCLC devices were fabricated, extra measures were taken with solution preparation. All polymer solutions were prepared at 15 mg mL^{-1} in chlorobenzene, and were allowed to stir overnight at room temperature. PE9TPF, however, did not go into solution as easily as the rest of the family. Consequently, the solution of PE9TPF was heated to $50 \text{ }^\circ\text{C}$ and stirred overnight. This still did not fully dissolve the polymer. The solution was raised to $100 \text{ }^\circ\text{C}$ just prior to spin casting, which allowed the polymer to completely dissolve. Subsequently, this extra heating may have led to polymer degradation and

thus the formation of traps in the solid-state device, resulting in a lower charge-carrier mobility.

4.4 Chapter Summary

The use of pendant π -functional electroactive polyolefins to controllably tune PLED EQE and hole mobility has been demonstrated. Regioregular and regiorandom terfluorenylidene polyolefins were synthesized and incorporated into PLEDs. Additionally, regioregular triarylamine functionalized polyolefins were synthesized and incorporated into SCLC devices. Finally, the effects on PLED EQE and hole mobility by backbone saturation were studied for the terfluorenylidene and triarylamine polymers, respectively.

The terfluorenylidene polymers were shown to have increased luminance and PLED EQE with increasing spacer length, and thus lower chromophore density. Saturating the backbone of the polyolefins showed minor, but nonetheless, increases in EQE. Upon saturation of P-9,9-TF, luminance increased three-fold, and EQE doubled. Due to a low T_g , P-9,9-TF-S experienced temporal and spatial morphological changes underneath the top electrode, presumably a result of Joule heating. A possible instrumental apparatus was proposed to fully confirm the occurrence of Joule heating during PLED testing.

Sequenced triarylamine functionalized polyolefins were shown to control hole mobilities over 3 orders of magnitude from $\sim 7 \times 10^{-7}$ to $\sim 3 \times 10^{-10} \text{ cm}^2 \text{ V}^{-1} \text{ s}^{-1}$. Increasing the spacer length of chromophores on the aliphatic backbone resulted in a decreased hole mobility due to increasing intermolecular hopping distances. Upon saturation of P33TPF, solubility was compromised due to the presence of residual

catalyst. This resulted in possible polymer degradation and the formation of trap states due to the necessity of heating the solution prior to spin casting.

As evidenced by the results presented in this chapter, pendant π -functional polymers with chromophores precisely spaced on an electrically insulating backbone, or electroactive polyolefins, are promising materials for light-emitting devices. An ideal spacer length may be optimized for electroactive materials to achieve reproducibly high EQEs. Additionally, hole mobilities may be strategically tuned to match those of electron mobilities for efficient charge recombination, and thus increased performance. We believe that the synthesis of pendant π -functional electroactive polyolefins is not limited to the materials presented in this work. These polymers have immense promise in the field of optoelectronics and can be prepared with a wide variety of chromophores to produce highly efficient light-emitting devices.

CHAPTER 5 PERSPECTIVES AND OUTLOOK

Over the past several decades, the field of organic electronics has grown immensely. Many research efforts are being made towards novel synthetic materials for optoelectronic applications in the industrial and consumer markets. Compared to petroleum-based materials, solar energy may provide a form of cleaner and cheaper power. Additionally, larger, thinner, more lightweight displays with lower power consumption are being sought after. However, for organic optoelectronics to transition from the classic spin coating process of the laboratory setting to roll-to-roll printing in the industrial setting, research efforts must be maximized in optimizing synthetic protocols and device design.

5.1 Bulk-Heterojunction Organic Photovoltaics

The first portion of this work examined the use of tailor-made additives for morphological control and increased device performance in molecular BHJ OPVs. Novel synthesis of asymmetric and symmetric derivatives, with bulky and small end-groups was achieved. At optimized tailor-made additive concentrations, critical OPV parameters such as the FF, J_{SC} , V_{OC} , and consequently PCE were increased. This work, however, was only applied to an isoindigo oligothiophene system. Tailor-made additives can be synthesized over a variety of organic materials for electronic applications. The use of tailor-made additives in conjunction with solvent additives may lead to breakthroughs in device performance of molecular BHJ OPVs pushing them over their polymeric counterparts.

It is without a doubt that organic and polymeric photovoltaics lag behind their inorganic counterparts in terms of PCE. For industrialization, these PCEs must be

increased. However, a researcher working with OPVs should not be discouraged by low device results. OPVs have many advantages over their inorganic counterparts in a practical industrial and consumer setting—they can be cheaply fabricated using non-toxic materials. Additionally, OPVs may be solution-processed onto thin, flexible substrates giving rise to innovative applications—t-shirts, backpacks, wrappings for buildings, etc.; whereas inorganic cells are heavy and brittle, thus limited to a rooftop or solar field. Furthermore, organic materials pose many advantages over their polymeric counterparts as well—simpler purification, less end-group contamination, no molecular weight variation, easier functionalization, and more reproducible syntheses.

5.2 Polymer Light-Emitting Diodes

The second portion of this work examined the synthesis and application of unique electroactive polymers. Typically, polyolefins are sought after industrially for their insulating properties. However, through ADMET, polyolefins can be synthesized with precisely spaced chromophores, giving rise to a new class of materials, “electroactive polyolefins.”

A family of terfluorenylidene polymers with precisely spaced chromophores was synthesized and incorporated into simple PLEDs. The systematic increase in EQE with increasing chromophore distance is very exciting. The systems observed in this work used 9,9-dioctylfluorene as the active fluorophore. However, as discussed in chapter 1, new emissive molecules are being synthesized and applied to optoelectronics daily. ADMET synthesis can be applied to many flavors of chromophores, and carbon spacing may be precisely tuned to achieve ideal EQEs. Additionally, such materials may be applied to multilayer devices utilizing electron and hole transport layers for increased performance.

When designing synthetic materials for PLED application, one must consider charge carrier mobilities in the solid-state device. As electrons and holes are injected at the electrodes in a PLED, they recombine in the emissive layer forming an exciton, which decays to give off the characteristic light the human eye recognizes. Balanced hole and electron mobilities are crucial for efficient charge transfer, recombination, and exciton formation. This work examined the synthesis and application of triarylamine functionalized polyolefins for systematic control of hole mobility. Though the hole mobilities observed were lower than their inorganic counterparts, they exceeded many electron mobilities in comparable organic systems. ADMET may become a gateway to synthesizing polymers with precisely spaced chromophores for both electron and hole transporting layers. Using similar chromophores with lined-up charge mobilities may lead to higher performing PLEDs. Though polymeric systems lag behind their organic counterparts, molecular design has infinite possibilities. A number of companies are already producing OLED televisions available to the consumer, and the results are beautiful. With increased research efforts and novel synthetic materials, OLED TV's may become cheaper and more widely available to the consumer.

APPENDIX
DERIVATION OF THE FIELD INDEPENDENT AND DEPENDENT MOTT-GURNEY
LAW

Consider a p-type semiconducting material sandwiched between two high work function metals to create ohmic contacts (Figure A-1), where only holes are injected, no electrons.

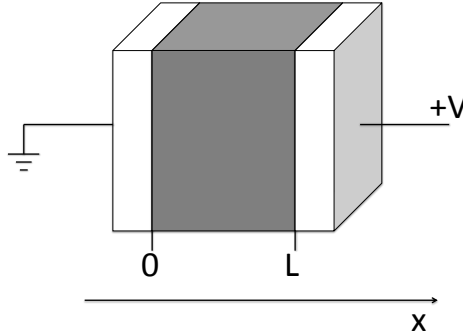


Figure A-1. Schematic of an organic semiconducting material sandwiched by two electrodes, with an applied voltage (V) and diffusion length (L) of the current flow in the positive x -direction.

According to Gauss' law, the free charge density (ρ) is given by

$$\rho = \epsilon_0 \epsilon_r \vec{\nabla} \cdot \vec{E} \quad (\text{A-1})$$

Considering the positive x direction as the flow of electrical current we have

$$\rho(x) = \epsilon_0 \epsilon_r \frac{\partial E(x)}{\partial x} \quad (\text{A-2})$$

Where E is the electric field, and ϵ is the permittivity (see section 1.1.4). At steady states, the continuity equation holds, indicating the current density, J , is independent of the x direction,

$$\vec{\nabla} \cdot \vec{J} = 0 \quad (\text{A-3})$$

The current density may be expressed as,

$$J = \rho(x)E(x)\mu \quad (\text{A-4})$$

Where μ is the charge mobility. Substitution of A-2 into A-4 gives

$$J = \mu\epsilon_0\epsilon_r \frac{\partial(E(x))^2}{\partial x} \quad (\text{A-5})$$

Rearrangement of A-5 into a usable form,

$$\frac{J}{\mu\epsilon_0\epsilon_r} dx = E(x) dE \quad (\text{A-6})$$

Let us allow $E(x) = E$ and define the variable ϕ for ease of derivation,

$$\phi = \frac{J}{\mu\epsilon_0\epsilon_r} \quad (\text{A-7})$$

Applying a boundary condition so that $E(0) = 0$ and integrating gives

$$\begin{aligned} \phi \int_0^x dx &= \int_0^E E dE \\ \phi x &= \frac{E^2}{2} \end{aligned} \quad (\text{A-8})$$

Given the length of diffusion in the positive x direction as L (Figure A-1), and the voltage across the active layer (V) given by

$$V = \int_0^L E dx \quad (\text{A-9})$$

Then rearranging, integrating both sides of A-8, and applying A-9, gives

$$\begin{aligned} (2\phi x)^{1/2} &= E \\ (2\phi)^{1/2} \int_0^L x^{1/2} dx &= \int_0^L E dx \\ \frac{2}{3} (2\phi)^{1/2} L^{3/2} &= V \end{aligned} \quad (\text{A-10})$$

Substituting A-7 into A-10 and solving for the current density gives us the Mott-Gurney law of the space charge limited current,

$$\begin{aligned} \frac{2}{3} \left(2 \frac{J_{SCL}}{\mu\epsilon_0\epsilon_r} \right)^{1/2} L^{3/2} &= V \\ J_{SCL} &= \frac{9}{8} \mu\epsilon_0\epsilon_r \frac{V^2}{L^3} \end{aligned} \quad (\text{A-11})$$

Equation A-10 provides the *field-independent* space charge limited current model. However, the field-dependent mobility is of interest in this work as it most accurately fits the data obtained. To begin the derivation of the field-dependent space charge limited current we combine Equations 1-13 (field dependence of the charge mobility) and A-4,

$$J = \mu_0 \exp(\gamma\sqrt{E}) \varepsilon_0 \varepsilon_r \frac{\partial(E(x))^2}{\partial x} \quad (\text{A-12})$$

Again, rearrangement, allowing $E(x) = E$, and defining a variable, ζ , for ease of derivation,

$$\zeta = \frac{J}{\mu_0 \exp(\gamma\sqrt{E}) \varepsilon_0 \varepsilon_r} \quad (\text{A-13})$$

Substituting A-13 gives

$$\zeta dx = E dE \quad (\text{A-14})$$

Integrating both sides of A-14 and applying A-9 gives

$$V = \int \frac{E^2}{\zeta} dE \quad (\text{A-15})$$

Substitution of A-13 into A-15 gives

$$V = \frac{\mu_0 \varepsilon_0 \varepsilon_r}{J} \int \exp(\gamma\sqrt{E}) E^2 dE \quad (\text{A-16})$$

Integration and expansion of A-16 is beyond the scope of this work, however, a detailed approximate solution has been demonstrated by Murgatroyd,³⁸ and yields the widely used *field-dependent* space charge limited current model,

$$J_{SCL} = \frac{9}{8} \mu_0 \varepsilon_0 \varepsilon_r \exp(0.891\gamma\sqrt{E}) \frac{V^2}{L^3} \quad (\text{A-17})$$

LIST OF REFERENCES

- (1) Seebeck, T. J. *Annalen der Physik* **1826**, 82, 253-286.
- (2) Königsberger, J.; Weiss, J. *Annalen der Physik* **1911**, 340, 1-46.
- (3) Shockley, W. B. J. Semiconductor Amplifier. US Patent 1948, 2502488.
- (4) Shirakawa, H.; Louis, E. J.; MacDiarmid, A. G.; Chiang, C. K.; Heeger, A. J. *Journal of the Chemical Society, Chemical Communications* **1977**, 578-580.
- (5) Dyer, A. L.; Thompson, E. J.; Reynolds, J. R. *ACS Applied Materials & Interfaces* **2011**, 3, 1787-95.
- (6) Vasilyeva, S. V.; Beaujuge, P. M.; Wang, S.; Babiarz, J. E.; Ballarotto, V. W.; Reynolds, J. R. *ACS Applied Materials & Interfaces* **2011**, 3, 1022-32.
- (7) Lei, T.; Cao, Y.; Fan, Y.; Liu, C.-J.; Yuan, S.-C.; Pei, J. *Journal of the American Chemical Society* **2011**, 133, 6099-101.
- (8) Ahmed, E.; Subramaniyan, S.; Kim, F. S.; Xin, H.; Jenekhe, S. A. *Macromolecules* **2011**, 44, 7207-7219.
- (9) Irimia-vladu, M.; Głowacki, E. D.; Troshin, P. A.; Schwabegger, G.; Leonat, L.; Susarova, D. K.; Krystal, O.; Ullah, M.; Kanbur, Y.; Bodea, M. A.; Razumov, V. F.; Sitter, H.; Bauer, S.; Sariciftci, N. S. *Advanced Materials* **2011**, 24, 375-380.
- (10) Chen, Z.; Lee, M. J.; Shahid Ashraf, R.; Gu, Y.; Albert-Seifried, S.; Meedom Nielsen, M.; Schroeder, B.; Anthopoulos, T. D.; Heeney, M.; McCulloch, I.; Siringhaus, H. *Advanced Materials* **2012**, 24, 647-52.
- (11) Mei, J.; Kim, D. H.; Ayzner, A. L.; Toney, M. F.; Bao, Z. *Journal of the American Chemical Society* **2011**, 133, 20130-20133.
- (12) Mohebbi, A. R.; Yuen, J.; Fan, J.; Munoz, C.; Wang, M.; Shirazi, R. S.; Seifert, J.; Wudl, F. *Advanced Materials* **2011**, 23, 4644-4648.
- (13) Tessler, N. *Applied Physics Letters* **2000**, 77, 1897.
- (14) Arif, M.; Mukhopadhyay, S.; Ramasesha, S.; Guha, S. *Europhysics Letters* **2009**, 87, 57008.
- (15) Zhong, C.; Duan, C.; Huang, F.; Wu, H.; Cao, Y. *Chemistry of Materials* **2011**, 23, 326-340.
- (16) Zhou, X.; Pfeiffer, M.; Blochwitz, J.; Werner, a.; Nollau, a.; Fritz, T.; Leo, K. *Applied Physics Letters* **2001**, 78, 410.

- (17) Bliznyuk, V. N.; Carter, S. A.; Scott, J. C.; Kla, G.; Miller, R. D.; Miller, D. C. *Macromolecules* **1999**, *32*, 361-369.
- (18) Gong, X.; Iyer, P. K.; Moses, D.; Bazan, G. C.; Heeger, a. J.; Xiao, S. S. *Advanced Functional Materials* **2003**, *13*, 325-330.
- (19) Leung, L. M.; Lo, W. Y.; So, S. K.; Lee, K. M.; Choi, W. K. *Journal of the American Chemical Society* **2000**, *122*, 5640-5641.
- (20) Furuta, P. T.; Deng, L.; Garon, S.; Thompson, M. E.; Fréchet, J. M. J. *Journal of the American Chemical Society* **2004**, *126*, 15388-9.
- (21) Xu, X.; Li, L.; Liu, B.; Zou, Y. *Applied Physics Letters* **2011**, *98*, 063303.
- (22) Peumans, P.; Yakimov, A.; Forrest, S. R. *Journal of Applied Physics* **2003**, *93*, 3693.
- (23) Mühlbacher, D.; Scharber, M.; Morana, M.; Zhu, Z.; Waller, D.; Gaudiana, R.; Brabec, C. *Advanced Materials* **2006**, *18*, 2884-2889.
- (24) Backer, S. a.; Sivula, K.; Kavulak, D. F.; Fréchet, J. M. J. *Chemistry of Materials* **2007**, *19*, 2927-2929.
- (25) Zhu, R.; Kumar, A.; Yang, Y. *Advanced Materials* **2011**, *23*, 4193-4198.
- (26) Armstrong, N. R.; Wang, W.; Alloway, D. M.; Placencia, D.; Ratcliff, E.; Brumbach, M. *Macromolecular Rapid Communications* **2009**, *30*, 717-731.
- (27) Chirvase, D.; Parisi, J.; Hummelen, J. C.; Dyakonov, V. *Nanotechnology* **2004**, *15*, 1317-1323.
- (28) Nelson, J.; Kwiatkowski, J. O. E. J.; Kirkpatrick, J.; Frost, J. M. *Accounts of Chemical Research* **2009**, *42*, 1768-1778.
- (29) Varshni, Y. P. *Physica* **1967**, *34*, 149-154.
- (30) O'Donnell, K. P.; Chen, X. *Applied Physics Letters* **1991**, *58*, 2924-2926.
- (31) Shaheen, S. E.; Jabbour, G. E.; Morrell, M. M.; Kawabe, Y.; Kippelen, B.; Peyghambarian, N.; Nabor, M.-F.; Schlaf, R.; Mash, E. a.; Armstrong, N. R. *Journal of Applied Physics* **1998**, *84*, 2324.
- (32) Parker, I. D. *Journal of Applied Physics* **1993**, *75*, 1656-1666.
- (33) Kim, J. S.; Park, J. H.; Lee, J. H.; Jo, J.; Kim, D.-Y.; Cho, K. *Applied Physics Letters* **2007**, *91*, 112111.
- (34) Sharma, S. K. *Atomic and Nuclear Physics*; Pearson Education, 2008; p. 118.

- (35) Koch, N.; Vollmer, a.; Elschner, a. *Applied Physics Letters* **2007**, *90*, 043512.
- (36) Meyer, J.; Khalandovsky, R.; Görrn, P.; Kahn, A. *Advanced Materials* **2011**, *23*, 70-3.
- (37) Mott, N. F.; Gurney, R. W. *Electronic Processes in Ionic Crystals*; Oxford University Press: London, 1940.
- (38) Murgatroyd, P. N. *Journal of Physics D: Applied Physics* **1970**, *3*, 151-156.
- (39) Schauer, F. *Solar Energy Materials and Solar Cells* **2005**, *87*, 235-250.
- (40) Nicolai, H. T.; Wetzelaer, G. a. H.; Kuik, M.; Kronemeijer, a. J.; de Boer, B.; Blom, P. W. M. *Applied Physics Letters* **2010**, *96*, 172107.
- (41) Bisquert, J.; Montero, J. M.; Bolink, H. J.; Barea, E. M.; Garcia-Belmonte, G. *Physica Status Solidi (a)* **2006**, *203*, 3762-3767.
- (42) Tanase, C.; Blom, P.; de Leeuw, D. *Physical Review B: Condensed Matter and Materials Physics* **2004**, *70*, 193202.
- (43) Azimi, H.; Senes, A.; Scharber, M. C.; Hingerl, K.; Brabec, C. J. *Advanced Energy Materials* **2011**, *1*, 1162-1168.
- (44) Ginley, D.; Green, M. A.; Collins, R. *MRS Bulletin* **2008**, *33*, 355-364.
- (45) Johnson, J. *Chemical & Engineering News* **2012**, *90*, 10.
- (46) Brown, N. Solar Junction Breaks Concentrated Solar World Record with 43.5 % Efficiency. *CleanTechnica* **2011**.
- (47) Krebs, F. C. *Solar Energy Materials and Solar Cells* **2009**, *93*, 465-475.
- (48) Krebs, F. C.; Fyenbo, J.; Jørgensen, M. *Journal of Materials Chemistry* **2010**, *20*, 8994.
- (49) Krebs, F. C. *Solar Energy Materials and Solar Cells* **2009**, *93*, 394-412.
- (50) Alstrup, J.; Jørgensen, M.; Medford, A. J.; Krebs, F. C. *ACS Applied Materials & Interfaces* **2010**, *2*, 2819-27.
- (51) Aernouts, T.; Aleksandrov, T.; Girotto, C.; Genoe, J.; Poortmans, J. *Applied Physics Letters* **2008**, *92*, 033306.
- (52) Hoth, C. N.; Schilinsky, P.; Choulis, S. A.; Brabec, C. J. *Nano Letters* **2008**, *8*, 2806-2813.
- (53) Eom, S. H.; Senthilarasu, S.; Uthirakumar, P.; Yoon, S. C.; Lim, J.; Lee, C.; Lim, H. S.; Lee, J.; Lee, S.-H. *Organic Electronics* **2009**, *10*, 536-542.

- (54) Andersen, T. R.; Larsen-Olsen, T. T.; Andreasen, B.; Böttiger, A. P. L.; Carlé, J. E.; Helgesen, M.; Bundgaard, E.; Norrman, K.; Andreasen, J. W.; Jørgensen, M.; Krebs, F. C. *ACS Nano* **2011**, *5*, 4188-96.
- (55) Manceau, M.; Angmo, D.; Jørgensen, M.; Krebs, F. C. *Organic Electronics* **2011**, *12*, 566-574.
- (56) Krebs, F. C.; Gevorgyan, S. a.; Gholamkhash, B.; Holdcroft, S.; Schlenker, C.; Thompson, M. E.; Thompson, B. C.; Olson, D.; Ginley, D. S.; Shaheen, S. E.; Alshareef, H. N.; Murphy, J. W.; Youngblood, W. J.; Heston, N. C.; Reynolds, J. R.; Jia, S.; Laird, D.; Tuladhar, S. M.; Dane, J. G. a.; Atienzar, P.; Nelson, J.; Kroon, J. M.; Wienk, M. M.; Janssen, R. a. J.; Tvingstedt, K.; Zhang, F.; Andersson, M.; Inganäs, O.; Lira-Cantu, M.; de Bettignies, R.; Guillerez, S.; Aernouts, T.; Cheyng, D.; Lutsen, L.; Zimmermann, B.; Würfel, U.; Niggemann, M.; Schleiermacher, H.-F.; Liska, P.; Grätzel, M.; Lianos, P.; Katz, E. a.; Lohwasser, W.; Jannon, B. *Solar Energy Materials and Solar Cells* **2009**, *93*, 1968-1977.
- (57) Amb, C. M.; Craig, M. R.; Koldemir, U.; Subbiah, J.; Choudhury, K. R.; Gevorgyan, S. a; Jørgensen, M.; Krebs, F. C.; So, F.; Reynolds, J. R. *ACS Applied Materials & Interfaces* **2012**, Article ASAP.
- (58) Amb, C. M.; Chen, S.; Graham, K. R.; Subbiah, J.; Small, C. E.; So, F.; Reynolds, J. R. *Journal of the American Chemical Society* **2011**, *133*, 10062-10065.
- (59) Small, C. E.; Chen, S.; Subbiah, J.; Amb, C. M.; Tsang, S.-wing; Lai, T.-han; Reynolds, J. R.; So, F. *Nature Photonics* **2012**, *6*, 115-120.
- (60) Zhou, H.; Yang, L.; Stuart, A. C.; Price, S. C.; Liu, S.; You, W. *Angewandte Chemie International Edition* **2011**, *50*, 2995-8.
- (61) Li, Z.; He, G.; Wan, X.; Liu, Y.; Zhou, J.; Long, G.; Zuo, Y.; Zhang, M.; Chen, Y. *Advanced Energy Materials* **2011**, *2*, 74-77.
- (62) Sun, Y.; Welch, G. C.; Leong, W. L.; Takacs, C. J.; Bazan, G. C.; Heeger, A. J. *Nature Materials* **2011**, *11*, 44-48.
- (63) Thompson, B. C.; Fréchet, J. M. J. *Angewandte Chemie* **2008**, *47*, 58-77.
- (64) Shuttle, C. G.; Treat, N. D.; Fan, J.; Varotto, A.; Hawker, C. J.; Wudl, F.; Chabinyc, M. L. *Journal of Polymer Science Part B: Polymer Physics* **2011**, *50*, 174-179.
- (65) Meng, X.; Zhang, W.; Tan, Z.; Li, Y.; Ma, Y.; Wang, T.; Jiang, L.; Shu, C.; Wang, C. *Advanced Functional Materials* **2012**, Early View Article.
- (66) Khlyabich, P. P.; Burkhart, B.; Thompson, B. C. *Journal of the American Chemical Society* **2011**, *133*, 14534-14537.

- (67) Derbal-Habak, H.; Bergeret, C.; Cousseau, J.; Simon, J. J.; Escoubas, L.; Nunzi, J.-M. *Journal of Photonics for Energy* **2011**, *1*, 011120.
- (68) Varotto, A.; Treat, N. D.; Jo, J.; Shuttle, C. G.; Batara, N. a; Brunetti, F. G.; Seo, J. H.; Chabinye, M. L.; Hawker, C. J.; Heeger, A. J.; Wudl, F. *Angewandte Chemie* **2011**, *50*, 5166-9.
- (69) Giebink, N.; Wiederrecht, G.; Wasielewski, M.; Forrest, S. *Physical Review B: Condensed Matter and Materials Physics* **2011**, *83*, 195326.
- (70) Deschler, F.; De Sio, A.; von Hauff, E.; Kutka, P.; Sauermann, T.; Egelhaaf, H.-J.; Hauch, J.; Da Como, E. *Advanced Functional Materials* **2012**, Early View Article.
- (71) Kawamoto, H. *Proceedings of the IEEE* **2002**, *90*, 460-500.
- (72) Weber, L. F. *IEEE Transactions on Plasma Science* **2006**, *34*, 268-278.
- (73) Keller, P. A. *The Cathode-Ray Tube: Technology, History and Applications*; Palisades Press: New York, 1992; p. 314.
- (74) Hornbeck, L. J. *Digital Light Processing: A New MEMS-Based Display Technology*; 1996.
- (75) Howard, W. E.; Prache, O. F. *IBM Journal of Research and Development* **2001**, *45*, 115.
- (76) Bernanose, A. *British Journal of Applied Physics* **1955**, *6*, S54-S56.
- (77) Al-Attar, H. a.; Monkman, A. P. *Journal of Applied Physics* **2011**, *109*, 074516.
- (78) Liu, Z.-Y.; Tseng, S.-R.; Chao, Y.-C.; Chen, C.-Y.; Meng, H.-F.; Horng, S.-F.; Wu, Y.-H.; Chen, S.-H. *Synthetic Metals* **2011**, *161*, 426-430.
- (79) Hung, L. S.; Chen, C. H. *Materials Science and Engineering R* **2002**, *39*, 143-222.
- (80) Kimura, M.; Kurata, T.; Sawaki, Y.; Toba, Y.; Enokida, T.; Takagi, K. *Bulletin of the Chemical Society of Japan* **2007**, *80*, 418-422.
- (81) Yan, H.; Lee, P.; Armstrong, N. R.; Graham, A.; Evmenenko, G. a; Dutta, P.; Marks, T. J. *Journal of the American Chemical Society* **2005**, *127*, 3172-83.
- (82) Barth, S.; Müller, P.; Riel, H.; Seidler, P. F.; Rieß, W.; Vestweber, H.; Bässler, H. *Journal of Applied Physics* **2001**, *89*, 3711.
- (83) Gao, H.; Zhang, H.; Mo, R.; Sun, S.; Su, Z.-M.; Wang, Y. *Synthetic Metals* **2009**, *159*, 1767-1771.
- (84) Li, H.; Winget, P.; Bredas, J.-L. *Advanced Materials* **2012**, *24*, 687-93.

- (85) Helander, M. G.; Wang, Z. B.; Qiu, J.; Greiner, M. T.; Puzzo, D. P.; Liu, Z. W.; Lu, Z. H. *Science* **2011**, *332*, 944-7.
- (86) Stalder, R. Ph.D. Dissertation, University of Florida, 2012.
- (87) Aitken, B. S.; Wieruszewski, P. M.; Graham, K. R.; Reynolds, J. R.; Wagener, K. B. *Macromolecules* **2012**, *45*, 705-712.
- (88) Aitken, B. S.; Wieruszewski, P. M.; Graham, K. R.; Reynolds, J. R.; Wagener, K. B. *ACS Macro Letters* **2012**, *1*, 324-327.
- (89) Graham, K. R.; Mei, J.; Stalder, R.; Shim, J. W.; Cheun, H.; Steffy, F.; So, F.; Kippelen, B.; Reynolds, J. R. *ACS Applied Materials & Interfaces* **2011**, *3*, 1210-5.
- (90) Heston, N. C. Ph.D. Dissertation, University of Florida, 2009.
- (91) Wu, C. C.; Wu, C. I.; Sturm, J. C.; Kahn, A. *Applied Physics Letters* **2001**, *70*, 1348-1350.
- (92) You, Z. Z.; Dong, J. Y. *Journal of Colloid and Interface Science* **2006**, *300*, 697-703.
- (93) Kasten, F.; Young, a T. *Applied Optics* **1989**, *28*, 4735-8.
- (94) Lampret, V.; Peternelj, J.; Krainer, A. *Solar Energy* **2003**, *73*, 319-326.
- (95) Graham, K. R. Ph.D. Dissertation, University of Florida, 2011.
- (96) Dutta, P.; Rathi, M.; Xie, Y.; Kumar, M.; Ahrenkiel, P. *Journal of Photonics for Energy* **2011**, *1*, 011124.
- (97) Ma, W.; Yang, C.; Gong, X.; Lee, K.; Heeger, a. J. *Advanced Functional Materials* **2005**, *15*, 1617-1622.
- (98) Koldemir, U.; Graham, K. R.; Salazar, D. H.; McCarley, T. D.; Reynolds, J. R. *Journal of Materials Chemistry* **2011**, *21*, 6480.
- (99) Ohara, T.; Matsumoto, Y.; Ohashi, H. *Physics of Fluids A: Fluid Dynamics* **1989**, *1*, 1949.
- (100) Bornside, D. E.; Macosko, C. W.; Scriven, L. E. *Journal of Applied Physics* **1989**, *66*, 5185.
- (101) Lou, S. J.; Szarko, J. M.; Xu, T.; Yu, L.; Marks, T. J.; Chen, L. X. *Journal of the American Chemical Society* **2011**, *133*, 20661-3.
- (102) Salim, T.; Wong, L. H.; Bräuer, B.; Kukreja, R.; Foo, Y. L.; Bao, Z.; Lam, Y. M. *Journal of Materials Chemistry* **2011**, *21*, 242.

- (103) Graham, K. R.; Stalder, R.; Wieruszewski, P. M.; Hartell, M.; Mei, J.; So, F.; Reynolds, J. R. Improved Performance of Molecular Bulk-Heterojunction Photovoltaic Cells through Predictable Selection of Solvent Additives **2012**, Submitted, *Advanced Functional Materials*.
- (104) Zhao, Y.; Xie, Z.; Qu, Y.; Geng, Y.; Wang, L. *Applied Physics Letters* **2007**, *90*, 043504.
- (105) Sary, N.; Richard, F.; Brochon, C.; Leclerc, N.; Lévêque, P.; Audinot, J.-N.; Berson, S.; Heiser, T.; Hadziioannou, G.; Mezzenga, R. *Advanced Materials* **2010**, *22*, 763-8.
- (106) Sivula, K.; Ball, Z. T.; Watanabe, N.; Fréchet, J. M. J. *Advanced Materials* **2006**, *18*, 206-210.
- (107) McNeill, C. R. *Energy & Environmental Science* **2012**, *5*, 5653-5667.
- (108) Lin, Y.; Lim, J. A.; Wei, Q.; Mannsfeld, S. C. B.; Briseno, A. L.; Watkins, J. J. *Chemistry of Materials* **2012**, *24*, 622-632.
- (109) Nguyen, L. H.; Hoppe, H.; Erb, T.; Günes, S.; Gobsch, G.; Sariciftci, N. S. *Advanced Functional Materials* **2007**, *17*, 1071-1078.
- (110) Janssen, G.; Aguirre, A.; Goovaerts, E.; Vanlaeke, P.; Poortmans, J.; Manca, J. *The European Physical Journal: Applied Physics* **2007**, *37*, 287-290.
- (111) Chen, D.; Liu, F.; Wang, C.; Nakahara, A.; Russell, T. P. *Nano Letters* **2011**, *11*, 2071-2078.
- (112) Berkovitch-Yellin, Z.; van Mil, J.; Addadi, L.; Idelson, M.; Lahav, M.; Leiserowitz, L. *Journal of the American Chemical Society* **1985**, *107*, 3111-3122.
- (113) Addadi, L.; Berkovitch-Yellin, Z.; Weissbuch, I.; van Mil, J.; Shirnon, L. J. W.; Lahav, M.; Leiserowitz, L. *Angew. Chem., Int. Ed. Engl.* **1985**, *24*, 466-485.
- (114) Lechuga-Ballesteros, D.; Rodriguez-Hornedo, N. *Journal of Colloid and Interface Science* **1993**, *157*, 147-153.
- (115) Wahal, A.; Bagard, P. *Comptes Rendus des Séances* **1913**, *156*, 1382-1385.
- (116) Mei, J.; Graham, K. R.; Stalder, R.; Reynolds, J. R. *Organic Letters* **2010**, *12*, 660-3.
- (117) Ma, Z.; Wang, E.; Vandewal, K.; Andersson, M. R.; Zhang, F. *Applied Physics Letters* **2011**, *99*, 143302.
- (118) Ma, Z.; Wang, E.; Jarvid, M. E.; Henriksson, P.; Inganäs, O.; Zhang, F.; Andersson, M. R. *Journal of Materials Chemistry* **2012**, *22*, 2306-2314.

- (119) Stalder, R.; Grand, C.; Subbiah, J.; So, F.; Reynolds, J. R. *Polymer Chemistry* **2012**, *3*, 89.
- (120) Stalder, R.; Mei, J.; Reynolds, J. R. *Macromolecules* **2010**, *43*, 8348-8352.
- (121) Stalder, R.; Mei, J.; Subbiah, J.; Grand, C.; Estrada, L. A.; So, F.; Reynolds, J. R. *Macromolecules* **2011**, *44*, 6303-6310.
- (122) Liu, B.; Zou, Y.; Peng, B.; Zhao, B.; Huang, K.; He, Y.; Pan, C. *Polymer Chemistry* **2011**, *2*, 1156.
- (123) Wang, E.; Ma, Z.; Zhang, Z.; Vandewal, K.; Henriksson, P.; Inganäs, O.; Zhang, F.; Andersson, M. R. *Journal of the American Chemical Society* **2011**, *133*, 14244-14247.
- (124) Wang, E.; Ma, Z.; Zhang, Z.; Henriksson, P.; Inganäs, O.; Zhang, F.; Andersson, M. R. *Chemical Communications* **2011**, *47*, 4908-10.
- (125) Zhang, G.; Fu, Y.; Xie, Z.; Zhang, Q. *Macromolecules* **2011**, *44*, 1414-1420.
- (126) Redecker, M.; Bradley, D. D. C.; Inbasekaran, M.; Woo, E. P. *Applied Physics Letters* **1998**, *73*, 1565.
- (127) Liang, Z.-Q.; Li, Y.-X.; Yang, J.-X.; Ren, Y.; Tao, X.-T. *Tetrahedron Letters* **2011**, *52*, 1329-1333.
- (128) Vu, T. T.; Badre, S.; Julien, C.; Audebert, P.; Senotrusova, E. Y.; Schmidt, E. Y.; Trofimov, B. A.; Pansu, R. B.; Clavier, G.; Me, R. *Journal of Physical Chemistry C* **2009**, *113*, 11844-11855.
- (129) Chen, C.-ti *Chemistry of Materials* **2004**, *16*, 4389-4400.
- (130) Xu, X.; Han, B.; Chen, J.; Peng, J.; Wu, H.; Cao, Y. *Macromolecules* **2011**, *44*, 4204-4212.
- (131) Huebner, C. F.; Foulger, S. H. *Langmuir* **2010**, *26*, 2945-50.
- (132) Sommer, M.; Lang, A. S.; Thelakkat, M. *Angewandte Chemie International Edition* **2008**, *47*, 7901-4.
- (133) Mei, J.; Aitken, B. S.; Graham, K. R.; Wagener, K. B.; Reynolds, J. R. *Macromolecules* **2010**, *43*, 5909-5913.
- (134) Park, J. H.; Yun, C.; Park, M. H.; Do, Y.; Yoo, S.; Lee, M. H. *Macromolecules* **2009**, *42*, 6840-6843.
- (135) Sugiyama, K.; Hirao, A.; Hsu, J.-C.; Tung, Y.-C.; Chen, W.-C. *Macromolecules* **2009**, *42*, 4053-4062.

- (136) Nantalaksakul, A.; Krishnamoorthy, K.; Thayumanavan, S. *Macromolecules* **2010**, *43*, 37-43.
- (137) Hong, C. H.; Lee, Y. B.; Bae, J. W.; Jho, J. Y.; Uk Nam, B.; Chang, D.-H.; Yoon, S.-H.; Lee, K.-J. *Journal of Applied Polymer Science* **2005**, *97*, 2311-2318.
- (138) Naskar, K.; Mohanty, S.; Nando, G. B. *Journal of Applied Polymer Science* **2007**, *104*, 2839-2848.
- (139) Kimyonok, A.; Domercq, B.; Haldi, A.; Cho, J.-yang; Carlise, J. R.; Wang, X.-yong; Hayden, L. E.; Jones, S. C.; Barlow, S.; Marder, S. R.; Kippelen, B.; Weck, M. *Chemistry of Materials* **2007**, *19*, 5602-5608.
- (140) Bellmann, E.; Shaheen, S. E.; Thayumanavan, S.; Barlow, S.; Grubbs, R. H.; Marder, S. R.; Kippelen, B. *Chemistry of Materials* **1998**, *10*, 1668-1676.
- (141) Kim, S.-H.; Lee, H.-J.; Jin, S.-H.; Cho, H.-N.; Choi, S.-K. *Macromolecules* **1993**, *26*, 846-848.
- (142) Wagener, K. B.; Boncella, J. M.; Nel, J. G. *Macromolecules* **1991**, *24*, 2649-2657.
- (143) Joule, J. P. *Philosophical Magazine and Journal of Science* **1841**, *19*, 260-277.
- (144) Zhou, B. X.; He, J.; Liao, L. S.; Lu, M.; Ding, X. M.; Hou, X. Y.; Zhang, X. M.; He, X. Q.; Lee, S. T. *Advanced Materials* **2000**, *12*, 265-269.
- (145) Choi, S. H.; Lee, T. I.; Baik, H. K.; Roh, H. H.; Kwon, O.; Suh, D. H. *Applied Physics Letters* **2008**, *93*, 183301.
- (146) Tessler, N.; Harrison, N. T.; Thomas, D. S.; Friend, R. H. *Applied Physics Letters* **1998**, *73*, 732.
- (147) Su, W.-F.; Chen, R.-T.; Chen, Y. *Journal of Polymer Science Part A: Polymer Chemistry* **2010**, *49*, 352-360.
- (148) Patel, D. G. (Dan); Graham, K. R.; Reynolds, J. R. *Journal of Materials Chemistry* **2012**, *22*, 3004-3014.
- (149) Lamansky, S.; Djurovich, P.; Murphy, D.; Abdel-Razzaq, F.; Lee, H. E.; Adachi, C.; Burrows, P. E.; Forrest, S. R.; Thompson, M. E. *Journal of the American Chemical Society* **2001**, *123*, 4304-12.
- (150) Kulkarni, A. P.; Tonzola, C. J.; Babel, A.; Jenekhe, S. a. *Chemistry of Materials* **2004**, *16*, 4556-4573.
- (151) Sun, X.; Zhou, D.-Y.; Qiu, L.; Liao, L.-S.; Yan, F. *The Journal of Physical Chemistry C* **2011**, *115*, 2433-2438.

- (152) Pho, T. V.; Kim, H.; Seo, J. H.; Heeger, A. J.; Wudl, F. *Advanced Functional Materials* **2011**, *21*, 4338-4341.
- (153) Emitters, E.-transporting; Li, Z. H.; Wong, M. S.; Tao, Y.; Fukutani, H. *Organic Letters* **2007**, *9*, 3659-3662.
- (154) Ecker, B.; Nolasco, J. C.; Pallarés, J.; Marsal, L. F.; Posdorfer, J.; Parisi, J.; von Hauff, E. *Advanced Functional Materials* **2011**, *21*, 2705-2711.
- (155) Yi, Y.; Jeon, P. E.; Lee, H.; Han, K.; Kim, H. S.; Jeong, K.; Cho, S. W. *The Journal of Chemical Physics* **2009**, *130*, 094704.
- (156) Bacher, E.; Bayerl, M.; Rudati, P.; Reckefuss, N.; Mu, C. D.; Meerholz, K.; Nuyken, O. *Macromolecules* **2005**, *38*, 1640-1647.
- (157) Chi, C.-C.; Chiang, C.-L.; Liu, S.-W.; Yueh, H.; Chen, C.-T.; Chen, C.-T. *Journal of Materials Chemistry* **2009**, *19*, 5561.
- (158) Barea, E. M.; Garcia-Belmonte, G.; Sommer, M.; Hüttner, S.; Bolink, H. J.; Thelakkat, M. *Thin Solid Films* **2010**, *518*, 3351-3354.
- (159) Klenkler, R. A.; Voloshin, G. *The Journal of Physical Chemistry C* **2011**, *115*, 16777-16781.
- (160) Huang, Q.; Li, J.; Marks, T. J.; Evmenenko, G. a.; Dutta, P. *Journal of Applied Physics* **2007**, *101*, 093101.
- (161) Cho, H. Y.; Park, L. S.; Han, Y. S.; Kwon, Y.; Ham, J.-Y. *Molecular Crystals and Liquid Crystals* **2009**, *498*, 314-322.
- (162) Lin, H.-yi; Liou, G.-sheng; Lee, W.-ya; Chen, W.-chang *Journal of Polymer Science Part A: Polymer Chemistry* **2007**, *45*, 1727-1736.
- (163) Laquai, F.; Hertel, D. *Applied Physics Letters* **2007**, *90*, 142109.
- (164) Meyer, J.; Kahn, A. *Journal of Photonics for Energy* **2011**, *1*, 011109.

BIOGRAPHICAL SKETCH

Patrick Michael Wieruszewski was born April 30, 1990 in Brandon, Florida to Marzenna and Maciej Wieruszewski. He grew up with an older sister and spent his childhood in Riverview, Florida, with annual visits to family in Władysławowo, Poland. For high school, he attended King High for two years, followed by Riverview High for the last two years. In the fall of 2008, Patrick began his undergraduate career at the University of Florida in Gainesville, FL, with a major in Chemistry. In the spring of 2010, he joined the research group of Dr. John R. Reynolds, with Ken Graham serving as his mentor. He initially worked on obtaining images of thin films using an Atomic Force Microscope, but was quickly interested in optoelectronics. He began fabricating and characterizing OPVs and PLEDs, leading to the work presented in this thesis. Patrick earned his Bachelor of Science degree in Chemistry with a minor in Materials Science and Engineering from UF in the spring of 2012. His girlfriend Megan earned her Bachelor of Science in Nursing, also from UF in the spring of 2012. After graduation, Patrick and Megan will move to Jacksonville, FL, where Patrick will be beginning the Doctor of Pharmacy program at the University of Florida, College of Pharmacy, and Megan will be working as a registered nurse.